2021

The Roles of Groundwater Table in Catchment Hydrology

Lili Yao
University of Central Florida

STARS Citation

Yao, Lili, "The Roles of Groundwater Table in Catchment Hydrology" (2021). *Electronic Theses and Dissertations, 2020-*. 1163.
https://stars.library.ucf.edu/etd2020/1163

THE ROLES OF GROUNDWATER TABLE IN CATCHMENT HYDROLOGY

by

LILI YAO
B.S. Taiyuan University of Technology, 2014
M.S. Beijing Normal University, 2017

A dissertation submitted in partial fulfillment of the requirements
for the degree of Doctor of Philosophy
in the Department of Civil, Environmental and Construction Engineering
in the College of Engineering and Computer Science
at the University of Central Florida
Orlando, Florida

Summer Term
2021

Major Professor: Dingbao Wang

ABSTRACT

The main goal of this dissertation research is to investigate catchment hydrological processes including infiltration and saturation excess runoff generation with consideration of groundwater table. For the infiltration process, an infiltration Péclet number was proposed to quantify the relative effects of gravity and capillary force on the evolution of infiltration capacity in the special case of the presence of a shallow water table, and a power law functional form of Time Compression Approximation was developed whose exponent was found to vary with the Péclet number. For the saturation excess runoff process, a new probability distribution model based on the SCS distribution function was developed. This new daily hydrologic model provided a framework for unifying water balance models from daily to mean annual timescales, and was applied to quantify the relative effects of climate variabilities on streamflow across different timescales for the U.S. Based on the new water balance model, a new analytical expression for mean annual baseflow was developed which was successfully used for disentangling the impacts of mean annual climate and landscape properties on baseflow generation in the U.S. and U.K. Inspired by the different statistical distributions of water storage at catchments, this dissertation further demonstrated that different functional forms of Budyko equation in the literature could be considered as emergent outcomes of the spatial variability of available water for evaporation. Considering the importance of water storage capacity and its spatial variability on hydrological processes, numerical simulations were conducted to explore the control of climate humidity on the spatial distribution of water storage at the catchment scale, and a new framework for unifying different saturation excess runoff models was obtained. The studies in this dissertation advance our understanding of hydrological processes with the presence of a groundwater table.

ACKNOWLEDGMENTS

I would like to acknowledge and give my warmest thanks to my advisor and committee chair Dr. Dingbao Wang. His guidance and advice carried me through all the stages of my doctorate study. He always aimed at moving me forward. His expertise and insightful feedback pushed me to sharpen my thinking and brough my research work to a higher level. I would also like to thank my committee members, Dr. Kelly Kibler, Dr. Arvind Singh, and Dr. David M. Sumner, for their continuous help and support when I undertook my research and writing my dissertation. I would like to thank Dr. Murugesu Sivapalan and Dr. Sankar Arumugam for their keen interest and cooperation during my doctorate research. I also had great pleasure of working with my colleagues at CHAMPS lab, Dr. Milad Hooshyar, Dr. Daljit Sandhu, Dr. Marwan Kheimi, Dr. Yuan Gao, Dr. Sevil Ranjbar, Dr. Saba Ghotbi, Dr. Jeane Camelo, Dr. Shiblu Sarker, and Ms. Yu Zhang. I must also thank the University of Central Florida for the financial support through the trustees doctoral fellowship. Special thanks to my family especially my brother for their love and support during my study in the U.S.

TABLE OF CONTENTS

LIST OF FIGURES

LIST OF TABLES

CHAPTER ONE: INTRODUCTION

Groundwater table is an important hydrologic interface controlling water exchange between surface and subsurface (Condon, et al., 2020; Ferguson & Maxwell, 2010; Hooshyar & Wang, 2016; Liang et al., 2003; Maxwell & Condon, 2016; Spence et al., 2009). During the rainfall-runoff process, antecedent soil moisture in a catchment which is determined by the location of groundwater table affects both infiltration capacity and effective soil water storage capacity. Therefore, groundwater table is closely associated with both the infiltration excess and saturation excess runoff generation in a catchment. The former occurs when water supply on the soil surface, e.g., rainfall intensity, is larger than the infiltration capacity, and the latter occurs when soil becomes fully saturated.

Infiltration is the entry of water into the soil surface and its subsequent vertical motion through the soil profile), and infiltration capacity is the maximum rate that occurs under condition of a continuously ponded surface. Infiltration capacity is large in the early time of an infiltration process and decreases gradually as soil moisture deficit decreases (Brutsaert, 2005). Existing analytical and empirical equations, e.g., Green-Ampt equation (Green and Ampt, 1911), Horton equation (Horton, 1940), Philip equation (Philip, 1957), and SCS curve number method (SCS, 1972) used for estimating infiltration rates and/or runoff generation are commonly based on two critical assumptions. Firstly, these equations assumed instantaneous ponding under which condition the actual infiltration rate equals infiltration capacity. Whereas, soil surface is typically not ponded at the onset of rainfall in natural infiltration conditions; therefore, the Time Compression Approximation (TCA) has been introduced to adjust the infiltration capacity for the discrepancy. However, the TCA relationship is assumed to be invariant during the infiltration process which can in fact change through time since the driving forces of infiltration, i.e., capillarity and gravity, is not static, and the dynamic TCA relationship is not largely unknown. The second assumption is the uniform initial soil moisture profile which is not reasonable under realistic field conditions with a finite depth of groundwater table. Therefore, the first part of this dissertation research aims to investigate the dynamic TCA relationship with presence of a shallow water table.

Groundwater table affects water balance behaviors by controlling the effective water storage capacity as well. Effective soil water storage capacity is defined as the total pore space above groundwater table in this dissertation research. Water balance can be conceptualized as a two-stage precipitation partitioning process (L'vovich, 1979). In the first stage, precipitation is partitioned into fast flow and soil wetting (or infiltration); in the second stage, soil wetting is further divided into baseflow and evaporation. Soil water storage capacity affects water balance in both stages. In the first stage, the effective storage capacity determines the maximum volumetric infiltration volume before the occurrence of saturation excess runoff. The spatial heterogeneity of soil water storage capacity facilitates runoff generations and determines the location of runoff generation (Beven & Kirkby, 1979; Liang et al., 1994; Moore, 1985). The impact of soil water storage capacity on the volume of soil wetting could propagate to the second partitioning stage since soil wetting from the first stage is the water source for the second stage. In addition, it has been found that the spatial variability of water storage capacity also influences the evaporation process since the actual evaporation is determined by both the water supply and atmospheric demand (Sivapalan et al., 1997). As a result, baseflow perceives influence from the groundwater table or the storage capacity not only because of its water source, i.e., soil wetting, but also because of the evaporation component which competes water in the second partitioning step. However, compared to the total streamflow, the impact of storage capacity and its spatial variability on the baseflow is much less known (Gnann et al., 2019; Meira Neto et al., 2020).

Hydrological models are powerful tools for evaluating and predicting the water balance under different climatic and catchment landscape conditions. Hydrological models could be divided into empirical (SCS, 1972), conceptual (Thomas, 1981; Moore, 1985), and physically distributed models (Refsgaard et al., 1995; Arnold et al., 1998). Empirical models lack representation of the physically based processes in hydrological systems. While, distributed physical models represent different hydrologic processes well using physical laws by accounting for both the spatial and temporal variabilities of inputs, they usually require extensive parameterization, more computation time and power (Devia et al., 2015). Therefore, conceptual water balance models are extensively used in the literature because they are simple to setup and use and yet incorporating important hydrological processes using semi-empirical equations with a physical basis (Devia et al., 2015). There are various hydrological models used for simulating hydrological responses at different timescales, such as VIC model for daily scale (Liang et al., 1994), “abcd” model for monthly scale (Thomas, 1981), and Budyko equation for annual scale (Budyko 1974). These models usually have various structures and are based on different assumptions on water balance behaviors. Though it is known that water balance behaviors should be consistent at different timescales, a more general understanding of hydrological behaviors is still lacking, and a unified framework for water balance models with connected theories across different timescales is needed (Berghuijs et al., 2020). Among the various timescales of water balance model, mean annual water balance models have the simplest parameterization and capture the most basic controls on the water balance behavior. Budyko equations may be the most popular mean annual water balance model in the field of hydrology because of its efficiency while parsimonious function form. Different forms of Budyko equations have been used in the literature (e.g., Budyko 1974; Yang et al., 2008; Turc, 1954; Zhang et al., 2004), whereas few studies have been conducted to explore the general hydrological basis of Budyko equations (Berghuijs et al., 2020).

Considering the configuration of groundwater table is directly related to the spatial distribution of water storage which is crucial for the catchment hydrological processes, it is necessary to understand the controls on the groundwater table and the corresponding spatial distribution of water storage within a catchment. A lot of studies have simplified the groundwater table as the subdued replica of topography (Cardenas, 2007; Jiang et al., 2010; Micallef et al., 2020; Toth, 1963; Zhang et al., 2020). Though studies have confirmed the benefit from this simple conceptualization, it has been found that water table is not always highly correlated to the land surface topography (Condon & Maxwell, 2015; Desbarats et al., 2002; Grayson & Western, 2001; Shaman et al., 2002). On the other hand, a number of studies focused on hillslope-scale processes have identified that the topography of hydrological impeding layer is one of the most important physical characteristics affecting the response of groundwater to rainfall (Bachmair & Weiler, 2012; Freer et al., 2002). The hydrological impeding layer could be a fresh bedrock or a soil layer with hydraulic conductivity several orders of magnitude lower than that of the surficial soil formation (Condon, et al., 2020; Freeze & Cherry, 1979). For the sake of brevity, we will refer to the hydrological impeding layer that restricts percolation as bedrock in this dissertation study. Based on observations at the hillslope scale, van Meerveld et al. (2015) and Hutchinson & Moore (2000) reported that the shapes of water table change with groundwater levels, and water table configuration follows land surface topography when the water table is shallow in wet conditions, whereas water table configuration follows bedrock topography when the water table is close to the bedrock in dry conditions. However, much uncertain still exists about the relationship between the topography (surface and subsurface) and groundwater configuration or the corresponding water storage at the catchment scale due to the limitation of bedrock information as mentioned previously.

This dissertation research aims to advance our understanding of catchment hydrological processes which are closely related to the groundwater table from the perspective of both infiltration excess and saturation excess runoff generation regimes. Specifically, there are five research objectives in this study. Firstly, the time invariance of the TCA relationship normally assumed is evaluated in the presence of a water table depth at finite depth, and to shed light on the factors that govern the time evolution of the TCA relationship. Secondly, a new conceptual water balance model at the daily time step is developed which unified water balance models with consistent water balance theories across timescales. The mean annual water balance model from this unified framework is then used for accomplishing the third objective, i.e., differentiating the roles of storage capacity and climate on baseflow at the mean annual scale. The fourth objective is to propose a general hydrological basis for unifying different Budyko equations from the view of the available water storage for evaporation, and the last objective is to investigate the variation of groundwater configuration and groundwater storage in different wetness conditions, and to examine the impacts of surface and subsurface topography on the spatial distribution of water storage.

CHAPTER TWO: TIME COMPRESSION APPROXIMATION WITH A SHALLOW WATER TABEL

2.1 Introduction

Infiltration is a critical component in the hydrological cycle associated with surface runoff, groundwater recharge, and evaporation. Its practical importance in hydrological studies has prompted the advance of infiltration theory over the years (Smith et al., 2002; Brutsaert, 2005; Assouline et al., 2007). Infiltration capacity is defined as the maximum infiltration rate that results when rainfall intensity is so large that the surface is saturated (i.e., ponded) instantaneously. Actual infiltration rate is typically lower due to the limited water supply to the soil surface, especially during early times during typical rainfall events. Indeed, infiltration capacity starts out large during early times and as more and more rainfall infiltrates, infiltration capacity decreases with time. The decreasing infiltration capacity eventually becomes equal to the rainfall intensity, and surface runoff (and ponding) is initiated. Ponding time is defined as the time after the beginning of rainfall at which ponding or surface runoff occurs (Diskin & Nazimov, 1996). From that time onward, with continued rainfall, the surface remains ponded, and so actual infiltration rate remains equal to infiltration capacity, but continues to decrease with time until (in the long-term) it reaches a constant rate asymptotically, provided the soil is sufficiently deep. Infiltration theory suggests the early time infiltration behavior is governed by absorption (due to capillary action of soil) while late time behavior is governed by gravitational action, and that the final constant infiltration rate after a long time is approximately equal to the saturated hydraulic conductivity of the soil (Brutsaert, 2005).

A common way to describe infiltration in soils is via Richards' Equation (1931) and its one-dimensional form can be expressed as:

$$\frac{\partial \theta}{\partial t} = \frac{\partial}{\partial z}\left[D(\theta)\frac{\partial \theta}{\partial z}\right] - \frac{\partial K(\theta)}{\partial \theta}\frac{\partial \theta}{\partial z} \tag{2.1}$$

where θ is volumetric soil water content; t is time; z is the depth measured from soil surface (positive downward); $K(\theta)$ is hydraulic conductivity; and $D(\theta)$ is soil water diffusivity defined as:

$$D(\theta) = K(\theta)\frac{\partial \psi}{\partial \theta} \tag{2.2}$$

where ψ is pressure head and negative in unsaturated soils.

Although infiltration rates from the numerical solution of Richards' Equation are available for various initial and boundary conditions, it is not practical to apply the numerical approach for hydrologic problems especially at large spatial scales. Instead, analytical and empirical Equations, e.g., Green-Ampt Equation (Green & Ampt, 1911), Horton Equation (Horton, 1940), Philip Equation (Philip, 1957), and SCS curve number method (SCS, 1972) are preferred for estimating infiltration rates and/or runoff generation. Assuming instantaneous ponding at the soil surface and a uniform initial soil moisture profile, Philip (1957) employed Boltzmann transformation to derive an analytical solution for ponded infiltration, expressed as an infinite power series:

$$f_c = \frac{1}{2}A_0 t^{-1/2} + (A_1 + K_s) + \frac{3}{2}A_2 t^{1/2} + 2A_3 t + \frac{5}{2}A_4 t^{3/2} + \cdots \tag{2.3}$$

where f_c is infiltration capacity; A_i are functions of initial moisture content; $A_0 = S$ which is defined as the soil’s sorptivity (a measure of its ability to absorb water in the absence of gravity); K_s is saturated hydraulic conductivity.

Similar to the Philip Equation, Green-Ampt and Horton Equations are also based on the assumption of instantaneous ponding on the soil surface. However, rainfall intensity is seldom larger than infiltration capacity at early times (Mein & Larson, 1973; Assouline et al., 2007), and therefore initially all rainfall infiltrates. To account for this discrepancy, the time compression approximation (TCA), also referred to as time condensation approximation, was introduced to estimate both ponding time and the post-ponding infiltration rate (Sherman, 1943; Holtan, 1945; Reeves & Miller., 1975; Milly, 1986; Sivapalan & Milly, 1989; Kim et al., 1996; Smith et al., 2002; Assouline., 2007; Wang et al., 2018). The essential concept behind TCA is the assumption of a unique, invariant relationship between infiltration capacity and the cumulative infiltration volume, regardless of the rainfall (or infiltration) history. The infiltration rate and cumulative infiltration volume after ponding could be obtained by shifting the time of infiltration capacity and cumulative potential infiltration over a compression reference time, respectively (Brutsaert, 2005); this explains the name “time condensation approximation”.

In past applications, the TCA relationship has been usually assumed to be invariant with time (i.e., unchanging) during the entire infiltration process (Milly, 1986; Kim et al., 1996; Smith et al., 2002; Wang et al., 2018). However, from the Philip Equation (Equation 2.3), one can observe that as time increases, more terms on the right-hand side need to be included in order to minimize the error. Consequently, the TCA relationship can in fact change through time, since the relative importance of the two driving forces on infiltration, i.e. capillarity and gravity, is dynamic. Capillarity dominates at early times when the soil is relatively dry and decays as the volume of water infiltrated (or depth of the wetting front) increases. Gravity dominates at longer times when the wetting front is very deep. The relative importance of these two forces changes during the infiltration process, coinciding with the change of infiltration rate and volume of infiltrated water (and wetting front depth). Therefore, it is reasonable to find recourse to the dynamic change of this relative effect to reveal how TCA relationship might evolve during infiltration. Philip (1969) introduced a characteristic time at which the effect of gravity is equivalent to that of capillarity. Philip (1986) also introduced a sorptive number, which is a parameter in the quasi-linear hydraulic conductivity function, and considered as a measure of the relative importance of capillarity and gravity during ponded infiltration and a uniform initial soil moisture profile (Basha, 2011). Considering the fact that ponding is delayed during actual rainfall events, and the possible presence of a water table at finite depth under realistic field conditions, a more general quantification and tracking of the relative effect of the two driving forces is needed.

The objective of this chapter is to link the relative effects of gravity and capillarity forces to the evolution of the TCA relationship, in the special case of the presence of a shallow water table.

2.2 Methodology

2.2.1 TCA and Infiltration Slope Curve

2.2.1.1 TCA

When rainfall intensity is larger than the saturated hydraulic conductivity (K_s) at the soil surface, infiltration rate decreases with time and approaches K_s for soil of sufficient depth (Brutsaert, 2005). Therefore, infiltration capacity can be decomposed into two components:

$$f_c = f_t + K_s \tag{2.4}$$

The reason for separating f_t and K_s is that K_s is a constant but f_t is a function of time. f_t represents the infiltration capacity relative to the case of gravitational force only. Consequently, the cumulative infiltration corresponding to f_t and K_s are:

$$F_t = \int_0^t f_t dt \tag{2.5}$$

$$F_0 = K_s t \tag{2.6}$$

The total cumulative potential infiltration F_c is:

$$F_c = F_t + F_0 \tag{2.7}$$

Traditionally, TCA defines the relationship between f_c (Equation 2.4) and F_c (Equation 2.7). In this paper, TCA was applied to the relationship between f_t and F_t since the relationship between F_0 and K_s is known, and simple enough, as shown in Equation (2.6).

2.2.1.2 Infiltration Slope Curve

In TCA, the infiltration rate after ponding is normally expressed as a function of cumulative infiltration. In this paper we propose a more general functional form of TCA between the infiltration capacity and its derivative with respect to time:

$$-\frac{df_t}{dt} = \alpha {f_t}^{\beta} \tag{2.8}$$

where α and β are parameters depending on the infiltration conditions. From Equation (2.8), by eliminating time, we can obtain the functional form for TCA between infiltration capacity and cumulative infiltration as:

$$f_t = \begin{cases} (\alpha(\beta - 2))^{\frac{1}{2-\beta}}(F_t + m_1)^{\frac{1}{2-\beta}} & \text{if } \beta \neq 2 \\ m_2 e^{-\alpha F_t} & \text{if } \beta = 2 \end{cases} \tag{2.9}$$

The values of m_1 and m_2 can be determined by considering f_t and F_t at the ponding time (t_p), i.e., $f_t(t_p) = i - K_s$ and $F_t(t_p) = (i - K_s)t_p$, where i is rainfall intensity. Substituting $f_t(t_p)$ and $F_t(t_p)$ into Equation (2.9), the values of m_1 and m_2 are obtained:

$$m_1 = \frac{(i-K_s)^{2-\beta}}{\alpha(\beta-2)} - (i - K_s)t_p \tag{2.10-1}$$

$$m_2 = (i - K_s)e^{\alpha(i-K_s)t_p} \tag{2.10-2}$$

The exponent β is an important parameter since it determines the shape of the TCA curve. In order to test the generalized TCA relation (Equation 2.8) and evaluate the controls on β, in this paper

$-\frac{df_t}{dt}$ and the corresponding f_t are computed using a numerical model of infiltration for various rainfall/infiltration events for a range of soil types. The plot of $-\frac{df_t}{dt} \sim f_t$ on log-log space is referred to here as the infiltration slope curve in analogy to the recession slope curve used in streamflow recession curve analysis (Brutsaert & Nieber, 1977).

2.2.2 Infiltration Péclet Number

A dimensionless number equivalent to Péclet number in linear advection-diffusion systems was applied to quantify the relative effect of gravity and capillarity. Péclet number generally quantifies the relative effect of mass transport by advective and dispersive (or diffusive) processes. It has been widely used to characterize the ratio of advective sediment transport due to water movement in channels and diffusive sediment transport driven by surface gradient of hillslopes in landscape evolution (Fernandes and Dietrich, 1997; Perron et al., 2009; Sweeney et al., 2015) and also the ratio of advection to diffusion in contaminant transport (Simmons et al., 1999; Detwiler et al., 2000; Huysmans and Dassargues, 2005; Pedretti et al., 2013). The general form of Péclet number is the ratio of the coefficient between advective term and the coefficient of diffusion term multiplied by a characteristic length scale (Huysmans & Dassargues, 2005). The one-dimensional Richards' Equation (Equation 2.1) is an advection-diffusion Equation and the first term on the right-hand side is a diffusion term, representing the component of infiltration caused by capillarity; and the second term represents the advective term driven by gravity. Therefore, the infiltration Péclet number (Pe) can be defined as:

$$Pe = \frac{\frac{\partial K(\theta)}{\partial \theta} L}{D(\theta)} \tag{2.11}$$

In this paper, the length scale L is defined as the depth of wetting front (below the soil surface), as shown in Figure 2.1a, since it is the traveled distance of infiltrated water. The unsaturated hydraulic conductivity K(θ) is given by the Brooks-Corey relationships (Brooks & Corey, 1964):

$$\frac{K}{K_s} = \left(\frac{\theta-\theta_r}{\theta_s-\theta_r}\right)^{3+\frac{2}{\lambda}} \tag{2.12-1}$$

$$\frac{\theta-\theta_r}{\theta_s-\theta_r} = \left(\frac{\psi_a}{\psi}\right)^{\lambda} \tag{2.12-2}$$

where θ_r and θ_s denote the residual and saturated moisture contents, respectively; ψ_a is called the bubbling pressure or air-entry value; and λ is the pore-size distribution index. By substituting Equation (2.12) into Equation (2.11), one obtains:

$$Pe = \frac{(3\lambda+2)L}{|\psi|} \tag{2.13}$$

When the initial vertical soil moisture profile is in hydraulic equilibrium with a water table, the absolute value of the pressure head at the wetting front is the difference between water table depth and wetting front depth:

$$|\psi| = W - L \tag{2.14}$$

where W is water table depth. Substituting Equation (2.14) into Equation (2.13), one obtains:

$$Pe = \frac{(3\lambda+2)}{1/\gamma-1} \tag{2.15}$$

where $\gamma = L/W$ is the ratio of wetting front depth to water table depth. When $Pe = 1$, the effects of capillarity and gravity are in balance in controlling infiltration; when $Pe < 1$, capillarity is dominant; whereas $Pe > 1$ indicates the dominance of gravity.

The Mualem-*van* Genuchten (MG) model (Mualem, 1976; van Genuchten, 1980) could also be used to represent the soil hydraulic properties in place of the Brooks-Corey model. The MG model has the advantage that it can provide a continuous characterization of the water retention curve from residual water content to saturated water content. The derivation of Péclet number for the MG model is presented in the Appendix for completeness. Equation (A8) in the appendix shows Pe as a function of $|\psi|$, and this Equation is more complex compared with Equation (2.13) for the Brooks-Corey model.

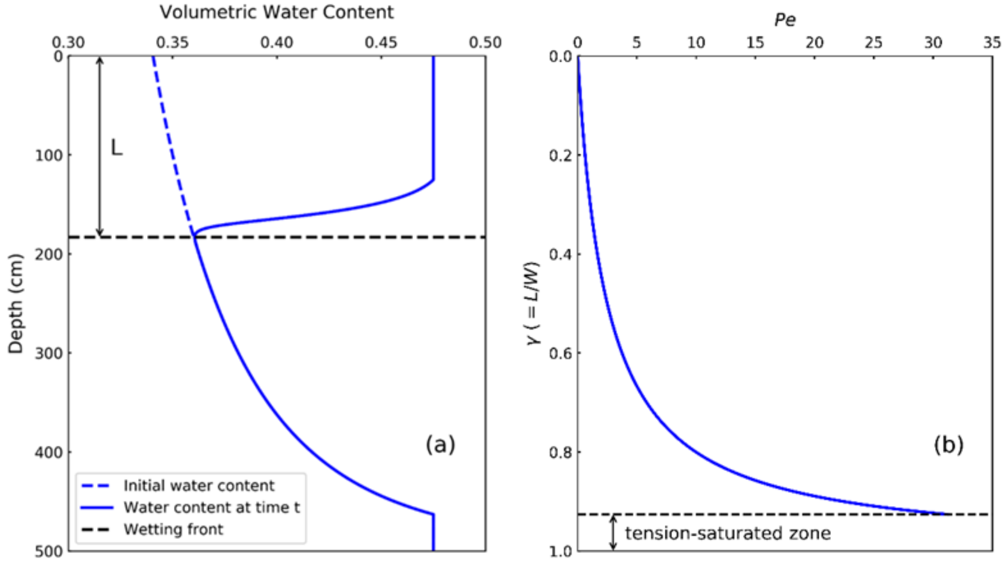

Figure 2.1: (a): soil moisture profile for clay soil with a constant rain rate of 2.4 mm/h and water table depth of 500 cm. The dashed and solid blue curves represent the water content profile at initial time and time t, respectively. The dashed black line denotes the position of wetting front at time t, below which the soil moisture is at hydrostatic condition. The distance between the soil surface and wetting front is the characteristic length L for defining Péclet number. (b): Péclet number increases as wetting front deepens. γ is the ratio between wetting front depth (L) and water table depth (W).

2.2.3 Numerical Simulations

In order to test the validity of the proposed power function relationship for TCA (Equation 2.8), numerical simulations are conducted for a range of infiltration events with different soil types, rainfall intensities, and water table depths.

2.2.3.1 HYDRUS

HYDRUS is a finite-element software package for simulating the movement of water, heat, and multiple solutes in variably saturated media (Šejna et al., 2018). It has been widely used for evaluating various irrigation systems, water flow and contaminant transport in the subsurface, the effects of plants on water movement in the subsurface and for many other agricultural and environmental applications (Pang et al., 2000; Vrugt et al., 2001; Schijven & Šimůnek, 2002; Cote et al., 2003; Skaggs et al., 2004; Dabach et al., 2013; Blackmore et al., 2018). The robust computational program and user-friendly interface make HYDRUS a powerful tool for simulating infiltration events in real world situations. In this paper, an advanced version of HYDRUS (i.e., 2D/3D) is used for simulating one-dimensional infiltration, since simulation time is not a concern for this study.

2.2.3.2 Simulation Settings

Five soil types (i.e., clay, silty clay loam, silty loam, sandy loam, and sand) with different capillary effects are considered in this paper, and their corresponding hydraulic properties are presented in Table 2.1. For each soil type, 7 rainfall intensities and 10 water table depths were considered, leading to a total of 350 simulations. Since TCA is only meaningful starting from ponding (Liu et al., 1998) and ponding only occurs with a rainfall intensity larger than saturated hydraulic conductivity of the soil, the rainfall intensities applied here are all larger than saturated hydraulic conductivity: $1.5K_s$, $2.0K_s$, $2.5K_s$, $3.0K_s$, $3.5K_s$, $4.0K_s$, and $10.0K_s$. The water table depths used range from 50 cm to 500 cm with a 50 cm interval. Different water table depths affect the initial soil moisture profile in soils and the total soil water storage capacity.

In all simulations, the model domain was a one-dimensional homogeneous soil column. At the soil surface, the Neumann boundary condition is applied before ponding, and the Dirichlet boundary condition is applied after ponding. Ponding time is determined by HYDRUS numerically. The bottom boundary is treated as a no-flow boundary. The initial soil moisture profile is an equilibrium profile consistent with a water table at finite depth (Salvucci & Entekhabi, 1995; Hooshyar & Wang, 2016). Model soil columns are vertically discretized into uniform cells of 0.5 cm. For time discretization, the initial time steps ranged from 3×10^{-6} s to 6 s depending on soil types and boundary conditions. Smaller time steps were used for cases with more nonlinear soil hydraulic properties and larger rainfall intensities (Šejna et al., 2018). Minimum time steps ranged from 10^{-9} s to 10^{-3} s; and maximum time steps ranged from 100 s to 86,400 s. HYDRUS could automatically adjust its optimal time step during the simulations.

Table 2.1: Hydraulic parameters of Brooks-Corey model for 5 soil classes (Maidment, 1993).

Soil type	K_s **(mm/hr)**	θ_r **(-)**	θ_s **(-)**	ψ_a **(mm^{-1})**	λ **(-)**
Clay	0.6	0.09	0.475	0.0027	0.165
Silty clay loam	2.0	0.04	0.471	0.0030	0.177
Silty loam	6.8	0.015	0.501	0.0048	0.234
Sandy loam	21.8	0.041	0.453	0.0067	0.378
Sand	235.6	0.02	0.437	0.0143	0.694

2.2.3.3 Calculation of Paired Values of $-\frac{df_t}{dt} \sim f_t$

Here we focus on the infiltration rate starting from the time of ponding and before the wetting front reaches close to the saturated zone at the bottom. The saturated hydraulic conductivity is subtracted from the original infiltration rate data since TCA is applied only to f_t in this paper instead of f_c (see Equation 2.4). $-\frac{df_t}{dt}$ and f_t are approximated as:

$$-\frac{df_t}{dt} = \frac{f_t^i - f_t^{i+1}}{\Delta t} \tag{2.16-1}$$

$$f_t = \frac{f_t^i + f_t^{i+1}}{2} \tag{2.16-2}$$

where the superscript i refers to infiltration at time t and $i+1$ refers to the time $t+\Delta t$. Δt is a suitable time increment for the calculation of time derivative of f_t, which increases as f_t decreases in order to eliminate the effect of numerical error in the infiltration data.

2.3 Results and Discussion

2.3.1 Effect of Rainfall Intensity and Water Table Depth on Exponent of TCA

Figure 2.2 shows the paired values of $-\frac{df_t}{dt}$ and f_t during infiltration events after ponding. For all soil types, the data points with the same water table depth and same soil texture almost fall on a single curve regardless of rainfall intensity. This indicates that for a given initial condition, $-\frac{df_t}{dt}$ is almost independent of rainfall intensity after ponding. This result proves the validity of the basic TCA assumption, which considers that infiltration capacity is independent of the rainfall intensity or infiltration history.

Figure 2.3 shows the infiltration slope curve for various water table depths. For a given f_t, $-\frac{df_t}{dt}$ decreases as water table depth increases. This is due to the larger relative capillary effect with deeper water table for a given value of f_t. For example, for clay soil with a rainfall intensity of $4.0K_s$, when f_t decreases to 1 mm/hr, Pe is 3.2 when water table depth is 1 m, but Pe is 0.5 when water table depth is 3.5 m. Larger relative capillary effect helps maintain a larger infiltration potential; therefore, $-\frac{df_t}{dt}$ decreases with increasing water table depth. This effect is more pronounced in clay soil compared to sand.

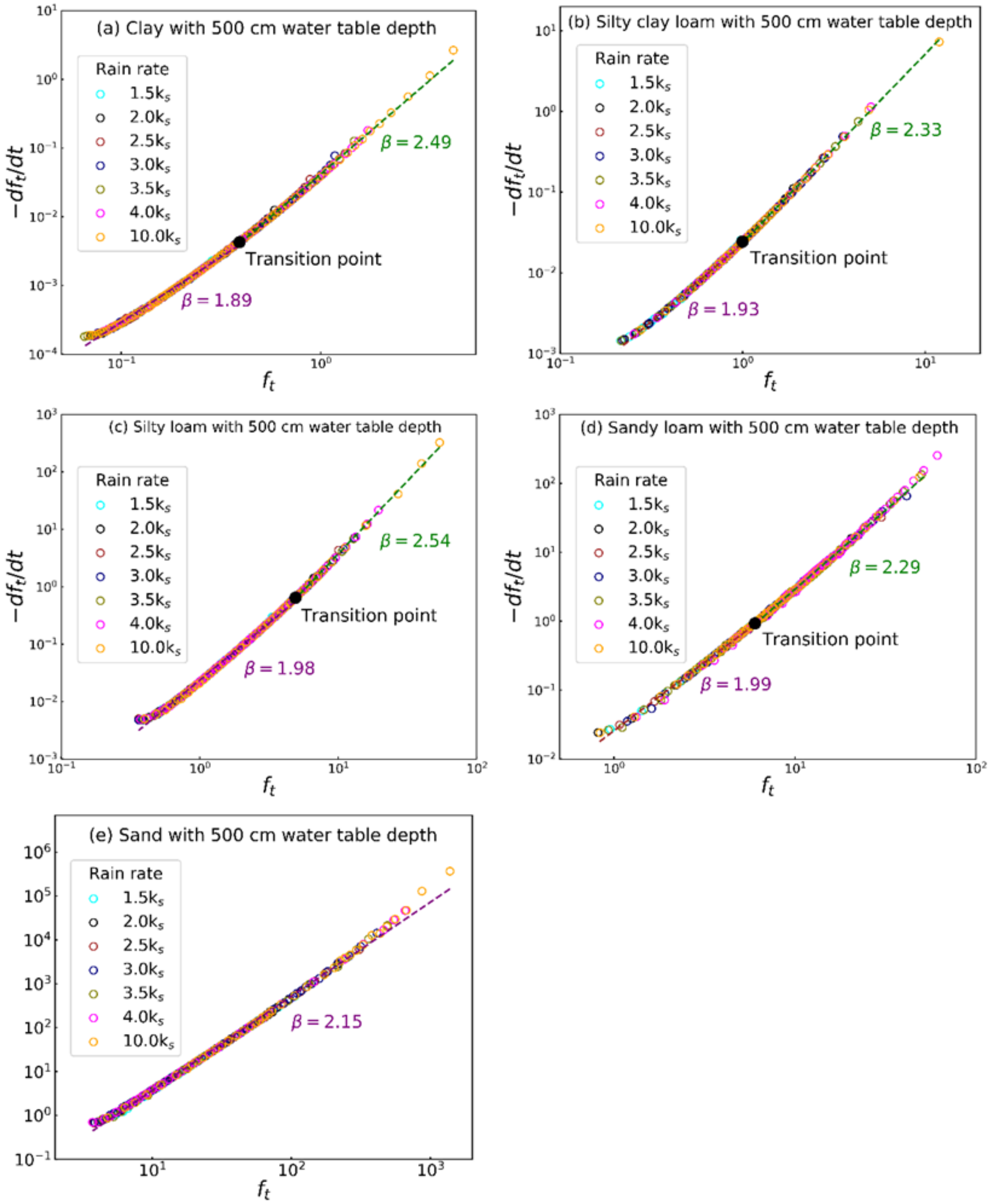

Figure 2.2: Infiltration slope curves for 5 soils with a water table depth of 500 cm: (a) clay, (b) silty clay loam, (c) silty loam, (d) sandy loam, and (e) sand. The data points with the same water table depth and soil texture almost fall on a single curve regardless of rainfall intensity, and the slope of each curve decreases as infiltration proceeds. The infiltration processes for (a), (b), (c), and (d) are divided into early and late stages.

The approximately linear curves in Figures 2.2 and 2.3 suggest that $-\frac{df_t}{dt}$ follows a power law relationship with respect to f_t, confirming the validity of the TCA function presented in

Equation (2.8). However, the data points in each curve can only be considered as a straight line over a certain range of f_t indicating the existence of different regimes during the infiltration process caused by the time evolution of the competition between capillarity and gravity. This means that the exponent β in Equation (2.8) is not a constant, which demonstrates that the TCA relationship is no longer invariant during the infiltration process, especially in the presence of a water table at finite depth.

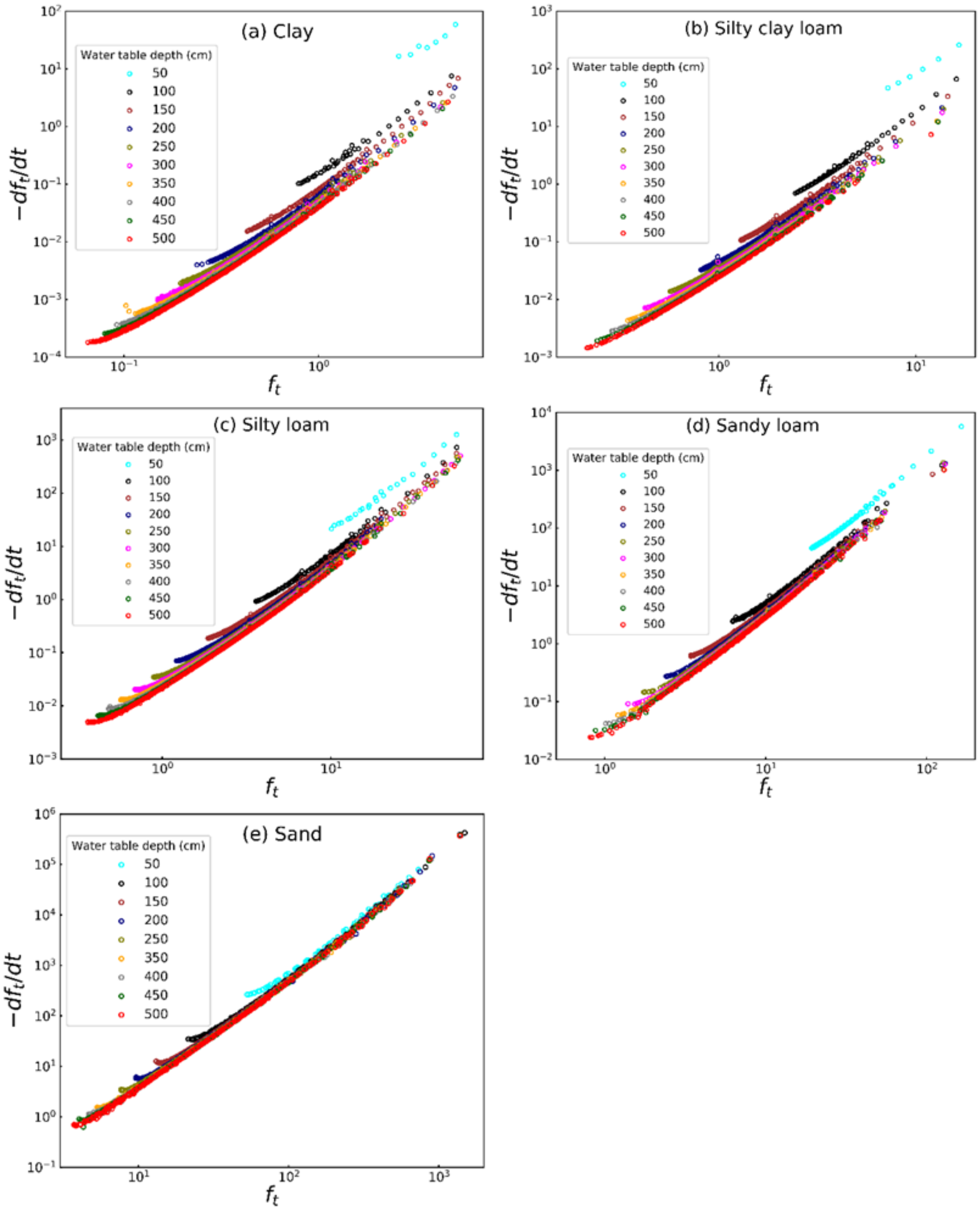

Figure 2.3: Infiltration slope curves for 5 soils with various water table depths: (a) clay, (b) silty clay loam, (c) silty loam, (d) sandy loam, and (e) sand. For a given f_t, $-df_t/dt$ decreases as water table depth increases.

2.3.2. Control of Péclet Number on the Exponent of TCA

As mentioned before, the Péclet number (Pe) is a measure of the relative effect of gravity and capillarity. Therefore, it changes as the wetting front moves down during infiltration. Figure 2.1b shows Pe as a function of γ, the ratio of wetting front depth (L) to water table depth (W), in clay soil with a water table depth of 500 cm. Pe increases as infiltration proceeds since advection due to gravity becomes more dominant.

The relationship between exponent β and Pe was analyzed for different stages of all of the infiltration events. We grouped every 6 consecutive data points of $-\frac{df_t}{dt}$ and f_t into an interval in all infiltration events and fitted a least squares regression line to the 6 paired points for estimating β in Equation (2.8). If the size of the last interval of an infiltration event was smaller than 6, these data were merged into the previous interval. The average Pe of the corresponding interval was computed according to the median time of each interval.

We fitted a least squares regression line to all the paired values of $\beta \sim Pe$ for all the 5 soil types (Figure 2.4a-e). β decreases with increasing Pe. When $Pe < 1$, β decreases roughly from 3.5 to 2 for clay, silty clay loam, and silty loam, and decreases from 3 to 2 for sandy loam and sand. The relationship between Pe and β is nonlinear when $Pe < 1$, and the rapid decrease of infiltration rate during early times after ponding contributes to the scattering of the data points. When $Pe > 1$, a linear relationship is formed between Pe and β for all soil types. During the transition from diffusion dominated to advection dominated infiltration, the exponent is about 2 for all soil types.

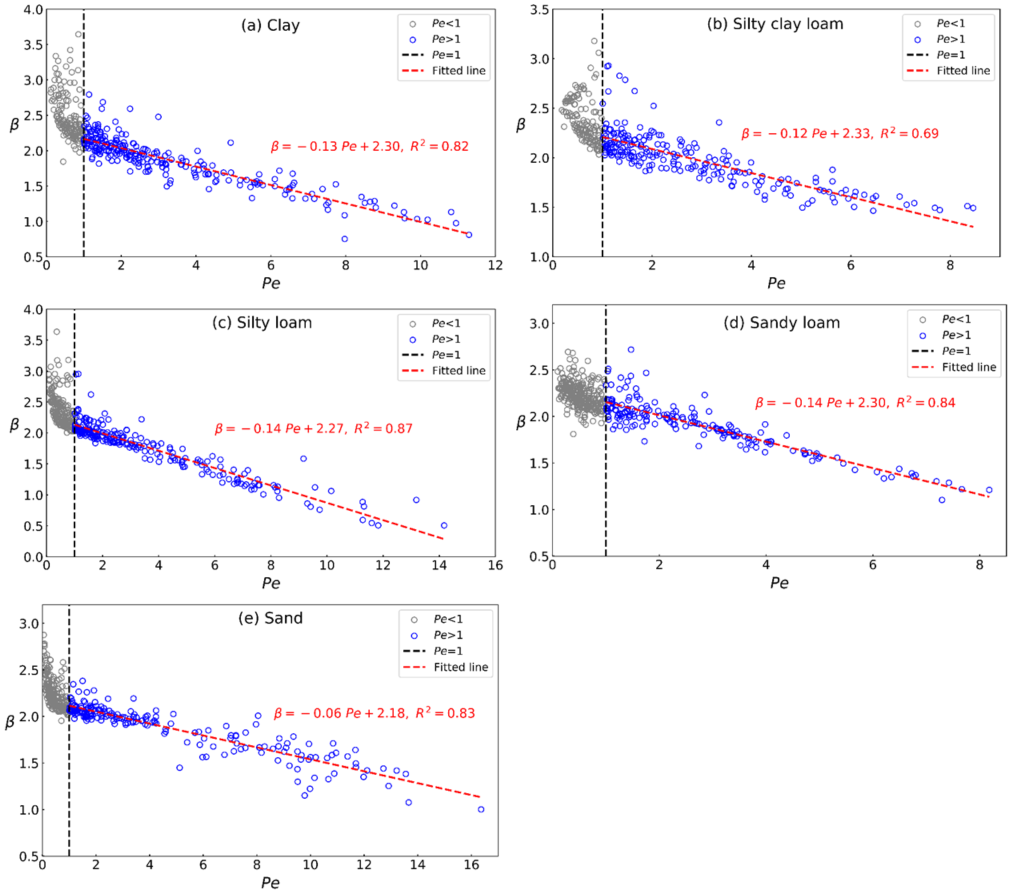

Figure 2.4: Relationships between Péclet number (Pe) and exponent (β)for 5 soils: (a) clay, (b) silty clay loam, (c) silty loam, (d) sandy loam, and (e) sand. For all soils, β decreases with Pe. When $Pe < 1$, the relationship between Pe and β is nonlinear; when $Pe > 1$, there is a linear relationship between Pe and β.

2.3.3 Implications for Infiltration Modeling

The decreasing exponent during infiltration indicates that a single TCA relationship may not accurately capture the entire infiltration process. For example, $\beta = 3$ leads to the two-term Philip Equation; $\beta = 1.5$ leads to the SCS curve number-type Equation (Mishra et al, 2003; Hooshyar & Wang, 2016); and $\beta = 1$ leads to the Horton Equation. As shown in Figure 2.4, β is around 2 when $Pe = 1$, i.e., $\beta > 2$ when $Pe < 1$, and $\beta < 2$ when $Pe > 1$. Therefore, the two-term Philip Equation is more applicable during early times when $Pe < 1$; whereas the SCS curve number-type Equation and the Horton Equation are more applicable during the late times when

$Pe > 1$. The relationship between Pe and β suggests that Péclet number can serve as an indicator for selecting the appropriate TCA function especially during the late times of infiltration. Figure 2.5 presents the frequency distribution of β from all data intervals, showing that most exponents are approximately around the value of 2. It should be noted that the SCS curve number method (i.e., $\beta = 1.5$) is for estimating catchment scale surface runoff, even though the power relation of TCA in this paper is validated at the point scale. This implies that the power law relationship for TCA may indeed be applicable, as a reasonable approximation, for infiltration and surface runoff estimation at the catchment scale.

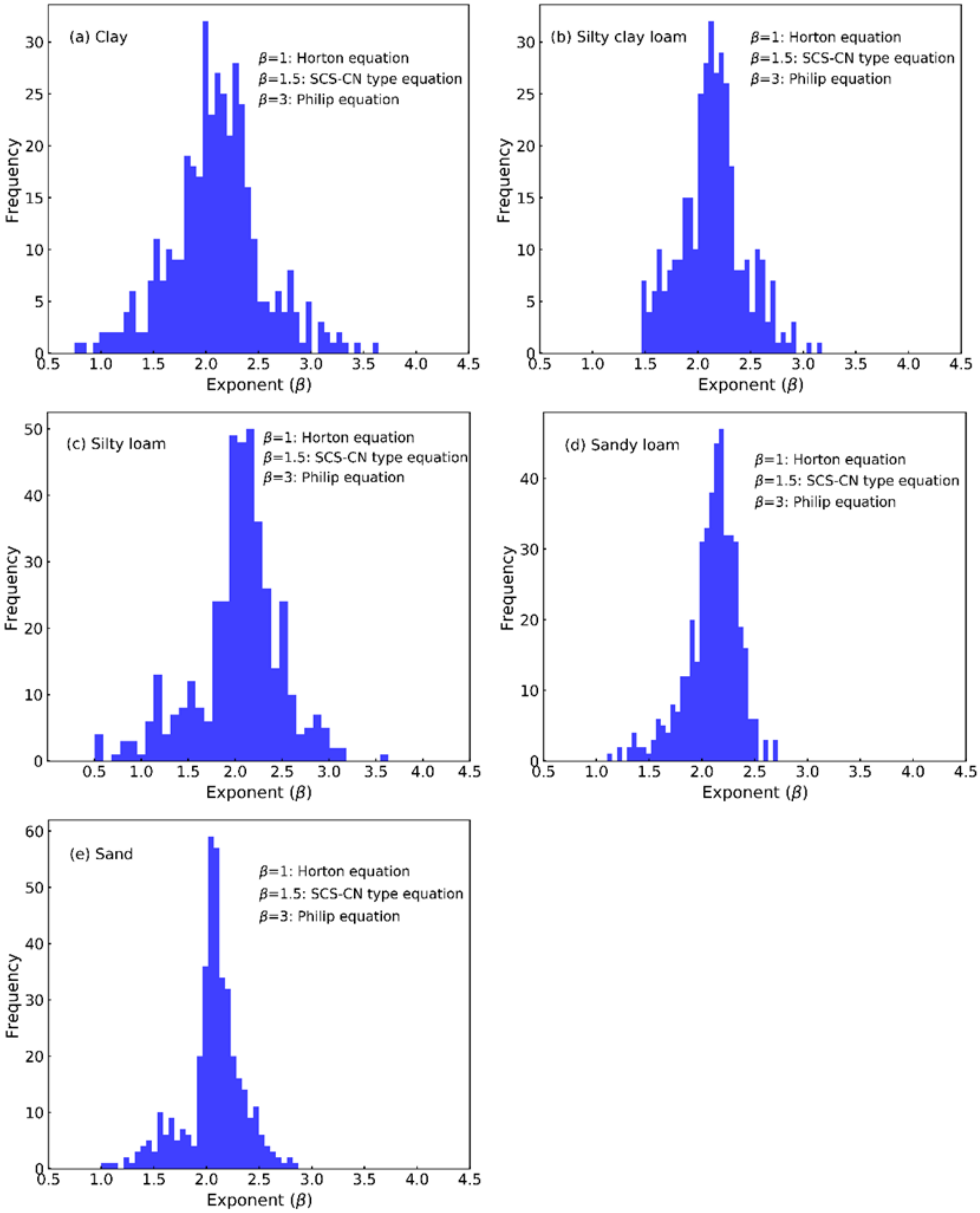

Figure 2.5: Frequency distributions of exponents (β) for 5 soils with various water table depths: (a) clay, (b) silty clay loam, (c) silty loam, (d) sandy loam, and (e) sand. The mode of exponent is approximately 2 for all soils.

For the TCA application in hydrologic modeling, the infiltration process could be divided into a certain number of stages given soil type and water table depth. For example, the individual infiltration event in Figures 2.2a-d could be divided into two stages for hydrologic modeling purposes, and the transition between early stage and late stage can be identified using statistical methods, such as cumulative regression method or maximum likelihood estimation approach; the latter has been used to test the validity of the power law distribution and to determine the starting point of the probability density function (PDF) of the power law distribution (Clauset et al., 2009; Pedretti & Bianchi, 2018). Since the TCA relationship in Figure 2.2 is not a PDF, the cumulative regression method based on least squares regression (Ghosh et al., 2016) is applied to identify the transition point. For each soil type, all pairs of $-\frac{df_t}{dt}$ and f_t are sorted in descending order according to the value of f_t. Linear regressions are implemented from the 1st until the j^{th} pair of data, where $j = 1, 2, 3, 4 \ldots N$, and N is the total number of data pairs. The coefficient of regression (R^2) is computed in each linear regression between $-\frac{df_t}{dt}$ and f_t on a log-log scale. The relationships between R^2 and f_t for different soils are shown in Figure 2.6. With the decrease of $log(f_t)$, R^2 increases to the maximum value (highlighted black point) and then decreases. As shown in Figure 2.6, the maximum R^2 is identified for clay (Figure 2.6a), silty clay loam (Figure 2.6b), silty loam (Figure 2.6c), and sandy loam (Figure 2.6d). Correspondingly, the transition from early stage to late stage infiltration is identified as the point with the maximum R^2, as shown in Figures 2.2a-d. The estimated exponents for early and late stages are shown in Figures 2.2a-d. It is not necessary to divide the infiltration process for sand into two stages (Figure 2.2e) since there is no obvious maximum for R^2 (Figure 2.6e).

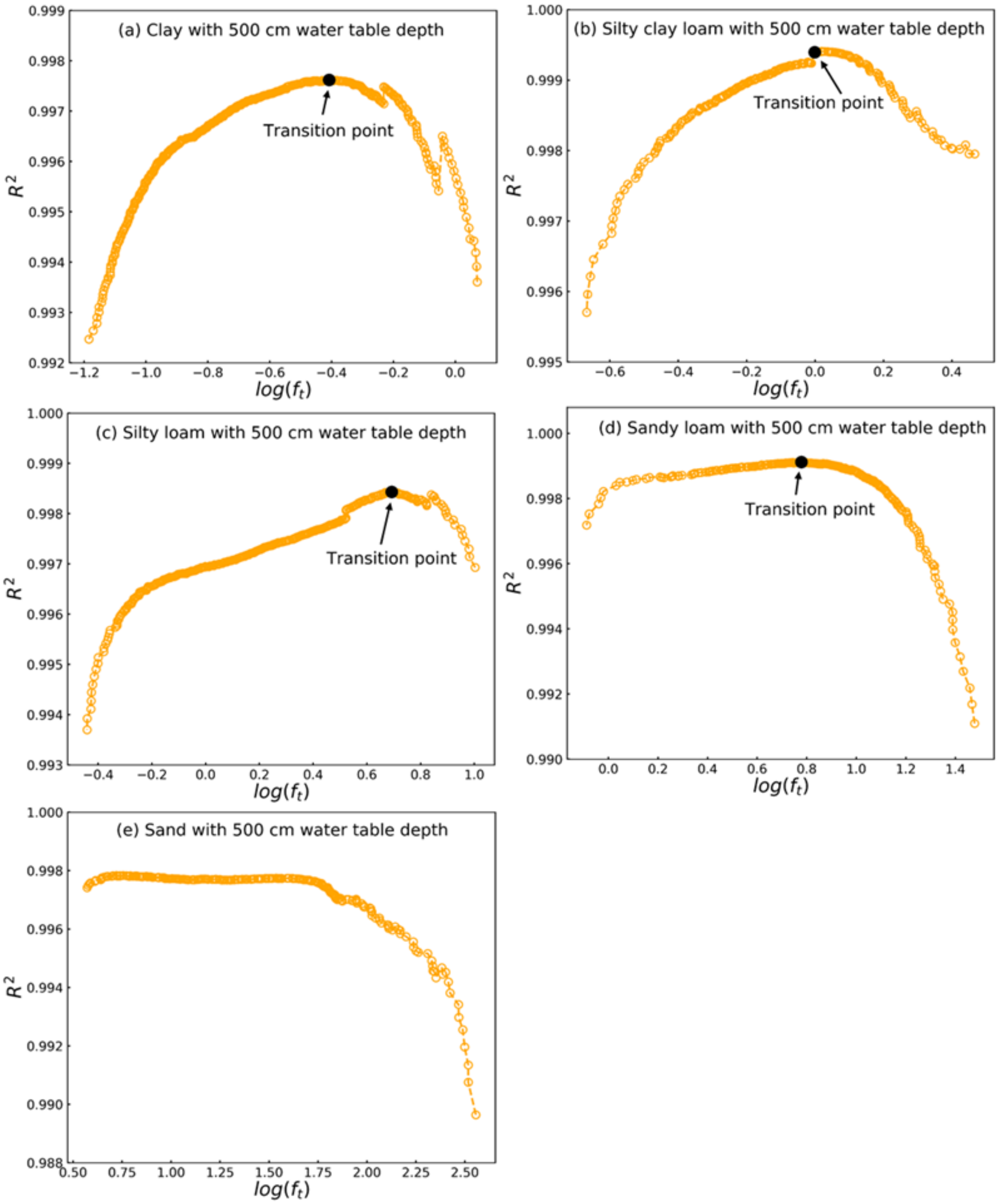

Figure 2.6: R^2 for cumulative regression changes with $log(f_t)$ for 5 soils: (a) clay, (b) silty clay loam, (c) silty loam, (d) sandy loam, and (e) sand.

2.4 Conclusion

A power function relationship is proposed for TCA, linking infiltration rate and its time derivative. Through numerical simulations with different soils, rainfall intensities and water table depths in one-dimensional soil columns, the approximately linear relation between infiltration rate and its time derivative on log-log space were obtained. The exponent in the power function of TCA is not dependent upon rainfall intensity or infiltration history, demonstrating the reasonable validity of the TCA. The decrease of the exponent suggests that the TCA relationship is not invariant during the infiltration process but evolves during different infiltration stages.

The relative effect of gravity and capillarity was quantified in terms of the Péclet number derived from Richards' Equation and the Brooks-Corey model for soil moisture retention, and the relationship between Péclet number (Pe) and exponent (β) was analyzed for different infiltration stages. When $Pe < 1$, β decreases from 3.5 to 2 for clay, silty clay loam and silty loam, and from 3 to 2 for sandy loam and sand with the increase of Pe; when $Pe > 1$, β has a linear relationship with Pe. On the transition from diffusion dominated to advection dominated, the exponent is about 2 for all soils. For application of TCA in hydrologic modeling, infiltration process could be divided into two stages with two exponents. For example, when water table depth is 500 cm, the average exponent for clay, silty clay loam, silty loam and sandy loam is 2.41 during the early stage and 1.95 during the late stage; and infiltration in sand could be modeled as a single stage with an exponent of 2.15. The relationship between Pe and β provides an objective approach to identify the suitable TCA function.

In this paper, for completeness, the Péclet number was also derived using the Mualem-van Genuchten model, in place of the Brooks-Corey model. The results from numerical simulations of soil types (clay and sandy loam) show that the power function relationship can be derived for TCA and that β decreases with Pe in way to similar to what was with the Brooks-Corey model. However, the critical value of Pe for the transition from diffusion-dominated to advection-dominated is now around 0.5 and the corresponding exponent is about 1.5 in clay and 1.0 in sandy loam. Future research will test the applicability of the power function relationship of TCA at the catchment scale, perhaps based on three-dimensional simulations, and to evaluate the effect of spatial soil heterogeneity on the power law exponent.

CHAPTER THREE: A NEW PROBABILITY DISTRIBUTION MODEL AND ITS APPLICATION

3.1 Introduction

Understanding how climate controls catchment streamflow at various timescales is of interest to hydrologists, earth system modelers, and water resources managers. Climate, soil, vegetation, and topography all affect hydrological processes (Eagleson, 1978; Farmer et al., 2003; Troch et al., 2013). The long-term average and shorter-term fluctuations of climate strongly affect the water balance directly and indirectly. Climate variability can control the water balance differently at the daily, monthly, and annual timescales (Jothityangkoon et al., 2001; Atkinson et al., 2002, Zhang et al., 2008). As the two main variables of climate: precipitation serves as the water supply to the catchments from the atmosphere, and potential evapotranspiration determines the water demand to the catchments. The effect of individual variability and co-variability of precipitation and potential evapotranspiration on streamflow are dependent on the timescale at which the streamflow is quantified (Atkinson et al., 2002; Farmer et al., 2003; Zhang et al., 2008). Daily streamflow variation is closely associated with intra-monthly climate fluctuations which are observed in the hyetographs for rainfall events. Intra-monthly variability of precipitation is much larger than that of potential evapotranspiration, and streamflow dynamics at the daily scale are strongly controlled by the daily precipitation interacting with catchment characteristics, such as antecedent soil moisture (Rodriguez-Iturbe et al., 1999; Aubert et al., 2003; Porporato et al., 2004; Botter et al., 2007). Antecedent soil moisture affects both the soil water storage capacity and infiltration capacity in catchments. Higher intensity of daily precipitation with higher frequency of occurrence would create favorable conditions for streamflow generation because of the limited soil retention and/or infiltration capacity (Brutsaert, 2005). Intra-annual and inter-annual climate fluctuations have impacts on daily streamflow through changing the antecedent soil moisture conditions and groundwater table depths (Sivapalan, et al., 2005; Berghuijs et al., 2014, 2016; Perdigão & Blöschl, 2014; Rossi et al., 2015). For example, on the first day of each month (or year), the runoff generation can be different for a given daily precipitation due to the different legacy soil moisture from the previous month (or year). Soil water storage capacity enables catchments to attenuate climate perturbations through hydrological processes of retaining and releasing water (McNamara et al., 2011). The variation in groundwater storage regulates the storm water storage space and the antecedent soil wetness condition (Troch et al., 1993; Soylu et al., 2011; Appels et al., 2017), and it can exhibit both significant seasonal and inter-annual variations because recharge from precipitation varies with time (Fan et al., 2007; Jasechko et al., 2014; McMillan & Srinivasan, 2015). Therefore, in order to fully capture the variation of daily streamflow, it is required to identify the impacts of climate variabilities at different timescales.

Intra-annual variations in precipitation and potential evapotranspiration are crucial characteristics of climate and are largely responsible for the streamflow variability at the monthly scale (Dettinger & Diaz, 2000; Yokoo et al., 2008; Yaeger et al., 2012; Berghuijs et al., 2014). Intra-annual variations in precipitation and potential evapotranspiration are usually described as sinusoidal functions (Milly, 1994; Woods, 2009; Gnann et al., 2019). When precipitation and potential evapotranspiration have similar magnitudes and means, the correlation between precipitation and potential evapotranspiration has significant impacts on the monthly streamflow. Streamflow seasonality can be weak when precipitation and potential evapotranspiration are in phase because the peak of water supply and water demand occur in the same month(s) even though both of them have a strong seasonality. On the other hand, if precipitation and potential evapotranspiration are out of phase, the peak of streamflow can be largely determined by the seasonality of precipitation because the peak of water supply coincides with the lowest water demand (Petersen et al., 2012; Berghuijs et al., 2014). Inter-annual climate variability also has an impact on the monthly water balance by controlling the antecedent soil moisture through storage carryover (Chen et al., 2013). Additionally, the number of rainfall events and the time intervals between rainfall events at the daily scale influence the monthly streamflow as well (Appels et al., 2017).

Inter-annual variation in the water balance has been investigated in many studies (Koster & Suarez, 1999; Arora, 2002; Yang et al., 2007; Istanbulluoglu et al., 2012; Han et al., 2018). It has been found that the inter-annual variability in streamflow is mainly controlled by the inter-annual variability of climate, especially in humid regions (Milly and Dunne, 2002; Yang et al., 2006; Xu et al., 2012). Intra-annual climate variability is also an important determinant of the inter-annual variations in streamflow (Milly & Dunne, 2002; Potter & Zhang, 2009; Jothityangkoon et al., 2009). For example, the same annual precipitation depth could produce different amounts of streamflow if precipitation is concentrated on just several months compared to if precipitation is evenly distributed across all the months. The impacts of daily storminess could also propagate to the annual streamflow, especially in dry catchments (Zanardo et al., 2012).

Mean annual water balances are mainly determined by the long-term average climate, or mean climate condition in terms of dryness index, defined as the ratio of mean annual potential evapotranspiration to mean annual precipitation. The first-order control of the mean climate on the mean annual streamflow has been widely demonstrated using the Budyko framework (Budyko, 1958, 1974; Milly, 1994; Zhang et al., 2001; Yang et al., 2008; Gentine et al., 2012). The scatter of catchments around the original Budyko curve has been interpreted as the result of shorter-term climate variability and catchment characteristics such as vegetation, soil, and topography (Fu, 1981; Porporato et al., 2004; Donohue et al., 2007; Li et al., 2013). Daily precipitation with a larger variance tends to increase mean annual streamflow (Shao et al., 2012), though it has been found the effects of daily storminess are almost negligible when the infiltration excess runoff is not prevalent (Reggiani et al., 2000). Several studies have shown that streamflow tends to be smaller for a given mean annual precipitation when the precipitation and potential evapotranspiration are in phase, and larger when they are out of phase (Milly, 1994; Hickel & Zhang, 2006; Feng et al., 2012; Petersen et al., 2012). However, the opposite could be observed because infiltration excess runoff can contribute significant volumes of streamflow in catchments when the precipitation and potential evapotranspiration are in phase (Potter et al., 2005). The influence of inter-annual climate variability on mean annual streamflow is often disregarded even though it has been demonstrated that the inter-annual variability of precipitation and potential evapotranspiration reduces the mean annual evaporation and increases the mean annual streamflow (Li, 2014).

Existing studies have recognized that streamflow, at each timescale, receives direct and indirect influences from climate variability at various timescales. However, a fundamental research question still remains unresolved: What are the relative impacts of different climate variabilities on streamflow at different timescales under different climatic regimes? For example, for the daily streamflow, which timescale climate variability plays the most important role on the streamflow variation?, and what are the relative magnitudes of the impacts exerted by intra-monthly, intra-annual, and inter-annual climate variability on the daily streamflow?

The main purpose of this paper is to systematically quantify the relative roles of intra-monthly, intra-annual, and inter-annual variability in precipitation (P) and potential evapotranspiration (E_p) on the streamflow at four timescales, i.e., daily, monthly, annual, and long-term. Additionally, this paper shows how the mean annual water balance of each catchment is affected by mean climate, soil water storage capacity as well as different climate variabilities using the Budyko framework. A new probability distributed model is developed in this paper for quantifying the contributions of different climate variabilities by comparing streamflow resulting from different timescale climate inputs. This chapter is organized as follows: In Section 3.2, the probability distributed model is presented, followed by how to apply different timescale climate inputs in the daily water balance model, and lastly, the methods for quantifying the roles of different climate variabilities on streamflow at the four timescales. Results and discussion are presented in Section 3.3, followed by summary in Section 3.4.

3.2 Methodology

3.2.1 A Probability Distributed Water Balance Model

Hydrological models are powerful tools for evaluating and predicting the water balance under different climate conditions by changing the climate inputs. The probability distributed model (PDM) is a kind of conceptual hydrological model which is simple to setup while incorporating important hydrological processes; therefore, a PDM is adopted in this study. PDMs consider catchments as a collection of storage elements with different storage capacities, and the spatial variability of storage capacity is represented by a probability distribution (Moore, 2007). Runoff in a PDM is generated from the saturated elements and by the discharge from soil storage, each is then routed through a storage tank. The generalized Pareto distribution has been widely used in PDMs, such as the Xiananjiang model (Zhao, 1977; Zhao, 1992), VIC model (Wood et al., 1992; Liang et al., 1994), and HyMOD (Moore, 1985; Chen et al., 2013; Razavi & Gupta, 2016). Recently, Wang (2018) proposed a new distribution function for describing the spatial variability of soil water storage capacity and showed that the corresponding soil wetting Equation can lead to the SCS-CN method (SCS, 1972) when the initial soil water storage is set to zero. In addition, this new distribution function can lead to a Budyko-type Equation for the mean annual water balance, further details will be shown in Section 3.4. Consequently, the new distribution function unifies the two runoff calculation methods, i.e., SCS-CN method and PDM, and unifies the water balance at different timescales. Considering the advantage of the new distribution function, it is used to develop a new PDM in this study. The distribution function is shown as follows:

$$F(C) = 1 - \frac{1}{a} + \frac{C+(1-a)S_b}{a\sqrt{(C+S_b)^2-2aS_bC}} \tag{3.1}$$

where C is soil water storage capacity at a point and $C \geq 0$; $F(C)$ is the fraction of the catchment area for which the storage capacity is less than or equal to C; a is the shape parameter with a range of $0 < a < 2$; and S_b is the average soil water storage capacity over the catchment. The new PDM has a similar model structure as HyMOD, except that is has a different method for determining the actual evaporation. Figure 3.1 presents the schematic description of the daily water balance model. As shown in this figure, precipitation is partitioned into soil wetting (i.e., infiltration, W) and runoff (R). Soil wetting, determined by both precipitation (P) and the initial soil water storage (S_0), is computed by the following integration (Moore, 1985):

$$W = \int_{C_0}^{P+C_0}[1 - F(C)]dC \tag{3.2}$$

where C_0 is the point storage capacity corresponding to S_0 in Figure 3.1. Substituting Equation (3.1) into Equation (3.2), soil wetting is obtained:

$$W = \frac{P+S_b\sqrt{(m+1)^2-2am}-\sqrt{[P+(m+1)S_b]^2-2amS_b{}^2-2aS_bP}}{a} \tag{3.3}$$

where,

$$m = \frac{S_0(2S_b - aS_0)}{2S_b(S_b - S_0)} \tag{3.4}$$

If the initial soil water storage is zero ($S_0 = 0$), Equation (3.3) becomes:

$$W = \frac{P + S_b - \sqrt{(P + S_b)^2 - 2aS_bP}}{a} \tag{3.5}$$

The shape parameter can be expressed as (*Wang*, 2018):

$$a = 2\varepsilon(2 - \varepsilon) \tag{3.6}$$

where ε is the initial soil wetting ratio, therefore, Equation (3.5) can be written as:

$$W = \frac{P + S_b - \sqrt{(P + S_b)^2 - 4\varepsilon(2 - \varepsilon)S_bP}}{2\varepsilon(2 - \varepsilon)} \tag{3.7}$$

Equation (3.7) is the root of the following quadratic function:

$$\varepsilon(2 - \varepsilon)W^2 - (P + S_b)W + PS_b = 0 \tag{3.8}$$

Equation (3.8) can also be expressed as a proportion:

$$\frac{P - W}{P - \varepsilon W} = \frac{W - \varepsilon W}{S_b - \varepsilon W} \tag{3.9}$$

Equation (3.9) is the proportionality relationship of the SCS-CN method (SCS, 1972). Therefore, the computation of soil wetting by Equations (3.3) is an extension of the SCS-CN method by explicitly incorporating initial soil moisture.

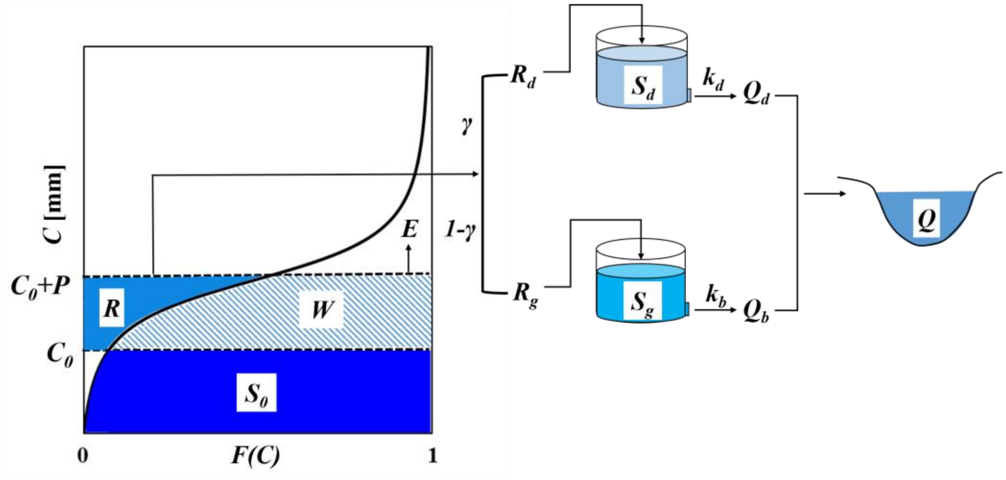

Figure 3.1: The structure of the daily water balance model which unifies the probability distributed model (PDM) and SCS-CN method. C is soil water storage capacity at a point; $F(C)$ is the fraction of the catchment area for which the storage capacity is less than or equal to C; S_0 is the initial soil water storage; P is the precipitation which is partitioned into is the soil wetting (W) and runoff (R); E is the actual evaporation; γ is the partitioning parameter of runoff between the direct runoff (R_d) and groundwater recharge (R_g); S_d and S_g are the storages in the quick storage tank and slow storage tank, respectively; k_d and k_b are the runoff coefficients of direct runoff and baseflow, respectively; Q_d, Q_b, and Q are the flow rates of direct streamflow, baseflow, and total streamflow at the catchment outlet, respectively.

Once soil wetting (W) is computed using Equation (3.3), the sum of soil wetting and initial soil water storage ($Y = W + S_0$) is then partitioned into evaporation (E) and ending soil water storage (S_1), i.e., $Y = E + S_1$. In the HyMOD model, E is assigned as the smaller value between Y and potential evapotranspiration proportional to the catchment saturation degree. Alternatively, in this model, the spatial heterogeneity of soil water storage is considered when determining evaporation. As shown in Figure 3.1, the actual soil water storage varies spatially due to the spatial variability of storage capacity. Therefore, the actual evaporation will also vary spatially even though the potential evapotranspiration is assumed to be spatially uniform. When the soil water storage at every element in a catchment reaches their individual storage capacities (Figure 3.2a) (i.e., the entire catchment is saturated), then the average evaporation over the entire catchment is computed as follows:

$$E_s = \int_0^{E_p} [1 - F(C)] dC \tag{3.10}$$

As presented in Figure 3.2a, the spatially averaged evaporation under conditions when the entire catchment is saturated (E_s) is smaller than E_p, even though the average storage (S_b) is greater than E_p. The reason is that the soil water storage at some elements in the catchment are lower than E_p and the evaporation at those points is equal to the corresponding soil water storage. For the condition when the catchment is not fully saturated (Figure 3.2b) with an average storage of $W + S_0$, evaporation is proportionally reduced from E_s relative to the soil water storage using Equation (3.11):

$$E = \frac{W+S_0}{S_b} E_s \tag{3.11}$$

Therefore, evaporation is computed by the following Equation after substituting Equation (3.1) into Equation (3.10):

$$E = \frac{W+S_0}{S_b} \frac{E_p + S_b - \sqrt{\left(E_p + S_b\right)^2 - 2aS_bE_p}}{a} \tag{3.12}$$

In the daily water balance model, runoff is decomposed into either direct runoff (R_d) or groundwater recharge (R_g) using a partitioning parameter (γ). The direct runoff and groundwater recharge are then stored in a quick storage tank (S_d) and a slow storage tank (S_g), respectively. These tanks are conceptually lumped storages representing the surface water body (S_d) and the unsaturated zone and shallow groundwater aquifer (S_g). Because water in the storage tanks cannot be totally released to the catchment outlet within one day after precipitation, therefore, linear relationships between tank outflows and tank storages are used for the routing processes.

Correspondingly, the total streamflow at the catchment outlet (Q) can be calculated using Equation (3.13-1) through Equation (3.13-8):

$$R = P - W \tag{3.13-1}$$

$$R_d = \gamma R \tag{3.13-2}$$

$$R_g = (1 - \gamma)R \tag{3.13-3}$$

$$Q_d = k_d(S_{d0} + R_d) \tag{3.13-4}$$

$$S_{d1} = (1 - k_d)(S_{d0} + R_d) \tag{3.13-5}$$

$$Q_b = k_b\big(S_{g0} + R_g\big) \tag{3.13-6}$$

$$S_{g1} = (1 - k_b)\big(S_{g0} + R_g\big) \tag{3.13-7}$$

$$Q = Q_d + Q_b \tag{3.13-8}$$

where the reciprocals of parameters k_d and k_b are the average characteristic times of the quick storage tank and slow storage tank; Q_d and Q_b are the flow rates of direct streamflow and baseflow measured at the catchment outlet; S_{d0} and S_{g0} are the initial storages in the quick storage tank and slow storage tank; S_{d1} and S_{g1} are the final storages in the quick storage tank and slow storage tank.

In total, there are five parameters for the daily model: a, S_b , γ, k_b, and k_d. The ranges and units of the parameters are shown in Table 3.1. Monthly and annual streamflow are aggregated from the daily streamflow, and the mean annual streamflow is the average of annual streamflow. The role of the soil water storage capacity and its spatial variability have received considerable attention in the mean annual water balance because the spatially variable storage capacity promotes the mean annual streamflow generation (Milly, 1994). In order to quantify the role of soil water storage capacity and its spatial variability, a base model scenario with a spatially uniform soil water storage capacity is developed for mean annual water balance. In this scenario, the uniform storage capacity is large enough so that no saturation excess runoff occurs, and the actual mean annual evaporation is calculated as the smaller value between the mean annual potential evapotranspiration and precipitation.

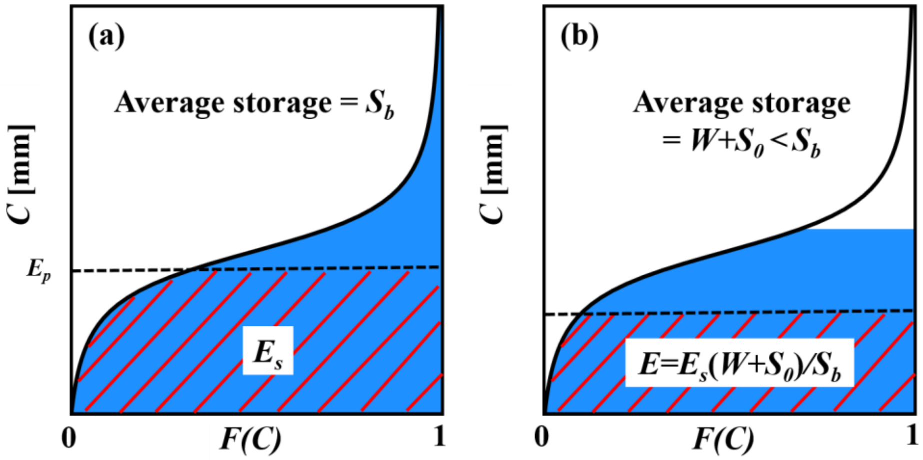

Figure 3.2: Evaporation is calculated based on the cumulative distribution function of soil water capacity when (a) the entire catchment is saturated and (b) the catchment is partially saturated. S_b is the average soil water storage capacity over the catchment; E_p is the potential evapotranspiration; E_s is the average evaporation over the catchment when the entire catchment is saturated.

3.2.2 Climate Inputs to the Daily Water Balance Model

This study uses four patterns of climate forcings. Figure 3.3 shows an example using the climate data over a three-year period from Caney River, Kansas. Figure 3.3a is the observed climate (OC), i.e., the daily time series of precipitation (mm/day) and potential evapotranspiration (mm/day), which encompass climate variability at all timescales. Figure 3.3b is the daily time series of monthly climate, with intra-monthly (IM) variability removed (i.e., daily values within a given month are replaced by their respective monthly mean) while preserving intra-annual (IA) and inter-annual (ITA) variability in forcings, and we denote this type of climate forcings as OC-

IM. Figure 3c is the daily time series of annual climate, with IM and IA variability removed (i.e., daily values are replaced with annual means) but with ITA variability preserved, and we denote this type of climate forcings as OC-IM-IA. Figure 3.3d is the daily time series of mean climate, specified by the long-term average values, without IM, IA and ITA variability in forcings (i.e., no variability in daily forcings), and we denote this type of climate forcings as OC-IM-IA-ITA. Model calibration is conducted using the observed daily precipitation and daily potential evapotranspiration (Figure 3.3a).

Each of the climate forcings is used to drive the daily water balance model to estimate daily streamflow. Comparing the results from OC and OC-IM can show the role of IM on streamflow. Likewise, comparing the results from OC-IM and OC-IM-IA can show the role of IA on streamflow, and comparing the results from OC-IM-IA and OC-IM-IA-ITA can show the role of ITA on streamflow.

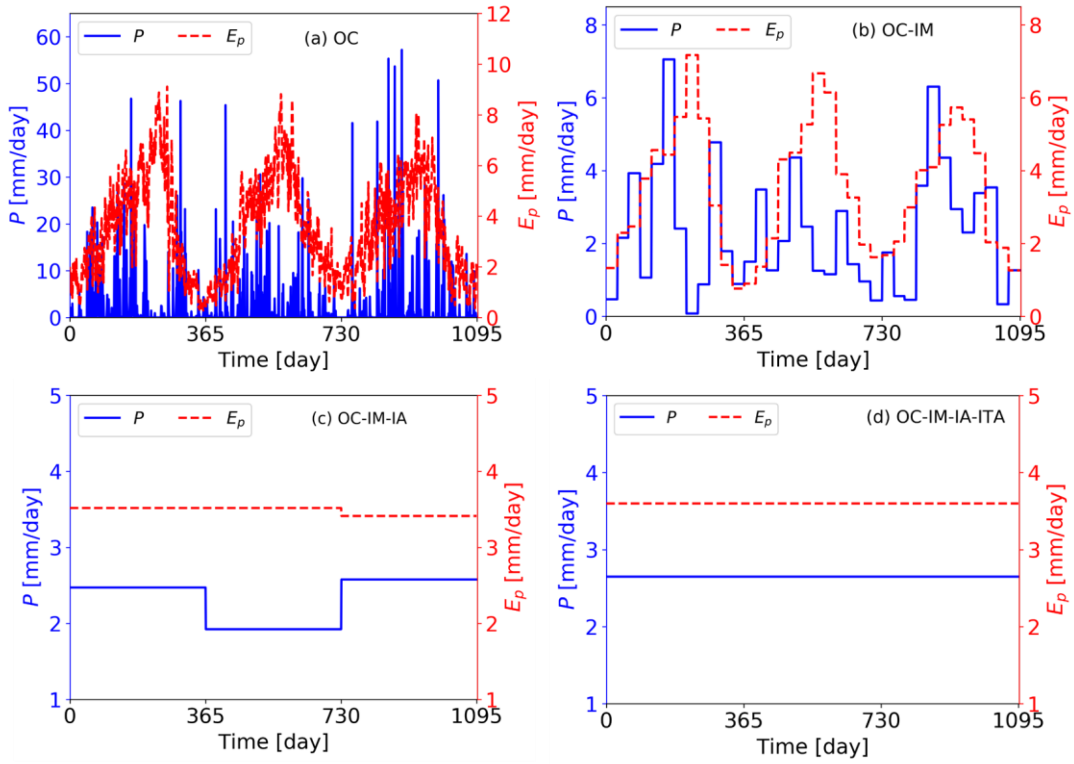

Figure 3.3: Examples of different temporal patterns of climate inputs for Caney River in Kansas (USGS gage number: 07172000) during the period of 2000-2002: (a) observed climate (OC), (b) climate without intra-monthly variability (OC-IM), (c) climate without intra-monthly and intra-annual variability (OC-IM-IA), and (d) mean climate, i.e., climate without intra-monthly, intra-annual, and inter-annual variability (OC-IM-IA-ITA). The blue solid line represents precipitation (*P*) and the red dashed line represents potential evapotranspiration (E_p).

3.2.3 Study Catchments and Data

Seventy-eight catchments from Model Parameter Estimation Experiment (MOPEX) (Duan et al., 2006) were used for this study. These catchments were selected due to their minimum human interferences (Wang and Hejazi, 2011) and snow effects to streamflow. The fraction of precipitation falling as snow (*SF*) was estimated from the empirical precipitation phase probability function proposed by Dai (2008) using daily average temperature and daily precipitation (Lute & Abatzoglou, 2014). The catchments with mean annual *SF* smaller than 15% (Berghuijs et al., 2014; Gao et al., 2014) were selected in this study. The area of study catchment ranges from 134 to 9886 km^2 and the dryness index ranges from 0.27 to 1.33. The hydrologic model used in this study is most useful for catchments where the saturation excess runoff regime is dominant. Therefore, catchments with a dryness index larger than 1.5 were not considered in this study because infiltration excess runoff generation would be significant in these catchments (Pilgrim et al., 1988). Observed daily streamflow for the years 1979-2003 is obtained through the MOPEX website (https://www.nws.noaa.gov/ohd/mopex/mo_datasets.htm), and extended through 2015 using the U.S. Geological Survey's (USGS) National Water Information System (https://waterdata.usgs.gov/nwis/sw). Daily precipitation and daily reference potential evapotranspiration are extracted from a gridded surface meteorological data set (gridMET) for the years 1979-2015 with a spatial resolution of ~4 km (http://www.climatologylab.org/gridmet.html) (Abatzoglou, 2013). Daily reference potential evapotranspiration in gridMET is calculated using the Penman-Monteith Equation (Monteith, 1964; Allen et al, 1998; Abatzoglou & Ficklin, 2017). Mean annual potential evapotranspiration values from MOPEX website are used for scaling the reference potential evapotranspiration in each study catchment.

3.2.4 Parameter Estimation and Model Performance

There are five parameters (i.e., a, S_b , γ, k_b, and k_d) in the daily water balance model. The parameters are conceptual representations of catchment characteristics. Thus, it is difficult to assign values using direct observations, instead, they can be determined through calibration. Available data are divided into three periods: 1) the warm-up period (1979-1980), 2) the calibration period (1981-1998), and 3) the validation period (1999-2015). Model parameters are calibrated using a Shuffled Complex Evolution Method (SCE-UA) (*Duan et al.*, 1992) and an open source python package SPOTPY (*Houska et al.*, 2015). The objective function (*OBJ*) consists of 6 components, including 3 Nash-Sutcliffe Efficiencies (*NSE*) (Nash and Sutcliffe, 1970; Moriasi et al., 2007) and 3 Volumetric Fit Efficiencies (*VFE*) (Wang et al., 2009) corresponding to daily, monthly, and annual streamflows, as shown:

$$OBJ = \left|1.0 - NSE_{daily}\right| + \left|1.0 - NSE_{monthly}\right| + \left|1.0 - NSE_{annual}\right| + \left|1.0 - VFE_{daily}\right| + \left|1.0 - VFE_{monthly}\right| + \left|1.0 - VFE_{annual}\right| \tag{3.14}$$

$$NSE_{daily} = 1 - \frac{\sum_{d=1}^{D}\left(Q_s^d - Q_o^d\right)^2}{\sum_{d=1}^{D}\left(Q_o^d - \overline{Q_{o,daily}}\right)^2} \tag{3.15-1}$$

$$NSE_{monthly} = 1 - \frac{\sum_{m=1}^{M}\left(Q_s^m - Q_o^m\right)^2}{\sum_{m=1}^{M}\left(Q_o^m - \overline{Q_{o,monthly}}\right)^2} \tag{3.15-2}$$

$$NSE_{annual} = 1 - \frac{\sum_{y=1}^{Y}\left(Q_s^y - Q_o^y\right)^2}{\sum_{y=1}^{Y}\left(Q_o^y - \overline{Q_{o,annual}}\right)^2} \tag{3.15-3}$$

$$VFE_{daily} = \frac{\sum_{d=1}^{D} Q_s^d}{\sum_{d=1}^{D} Q_o^d} \tag{3.15-4}$$

$$VFE_{monthly} = \frac{\sum_{m=1}^{M} Q_s^m}{\sum_{m=1}^{M} Q_o^m} \tag{3.15-5}$$

$$VFE_{annual} = \frac{\sum_{y=1}^{Y} Q_s^y}{\sum_{y=1}^{Y} Q_o^y} \tag{3.15-6}$$

where Q_o^d (Q_o^m, Q_o^y) is the observed daily (monthly, annual) streamflow on the d^{th} day (m^{th} month, y^{th} year); Q_s^m (Q_s^m, Q_s^y) is the simulated daily (monthly, annual) streamflow; $\overline{Q_{o,daily}}$ ($\overline{Q_{o,monthly}}$, $\overline{Q_{o,annual}}$) is the observed mean daily (monthly, annual) streamflow during the calibration period; and D (M, Y) is the total number of days (months, years) for calibration.

Including daily, monthly, and annual streamflow in the objective function for calibration ensures that the model performance is satisfactory at multiple timescales (Schaake et al., 1996; Hay et al., 2006; Sudheer et al., 2007). In addition, using two performance metrics in calibration, *NSE* and *VFE*, will simultaneously improve estimation of the hydrograph and of volumetric fitting. The value of *NSE* ranges from $-\infty$ to 1, with a value of 1 representing a perfect estimation of observed variability. *VFE*, ranging from $-\infty$ to ∞, reflects model bias with a value of 1 corresponding to no model bias. The same objective function weights for *NSE* and *VFE* are used for 3 timescales modeled in this study. Parameter values are chosen for each catchment by minimizing the objective function and fixing them for each model run.

3.2.5 Roles of Climate Variability on Streamflow at Different Timescales

3.2.4.1 Daily, Monthly, and Annual Streamflow

The role of each climate variability in daily, monthly, or annual streamflow is defined as its ability to explain streamflow variability at each timescale. This ability is quantified by the difference in *NSE* values from the simulated streamflow using the climate inputs at two consecutive timescales. Quantifying the role of climate variability in this study uses *NSE* because it is an indicator for evaluating the overall model behavior with an emphasis on the timing and shape of the hydrograph which reflects the sensitivity of streamflow to climate fluctuations. Additionally, *NSE* can be applied to streamflow at different timescales. A consistent index across timescales helps systematically compare the roles of each climate variability on streamflow at multiple timescales. The role of each climate variability in terms of ΔNSE is normalized by the *NSE* value resulting from the observed climate, shown in the following Equation:

$$\rho_{k,j} = \frac{NSE_{i,j} - NSE_{i+1,j}}{NSE_{1,j}} \tag{3.16}$$

where $\rho_{k,j}$ represents the relative role of different climate variabilities ($k = IM, IA, ITA$) on the j^{th} (j = 1, 2, 3) timescale streamflow. For example, Figure 3.4a shows the flow chart for quantifying the roles of different climate variabilities on the daily streamflow (j = 1). The role of IM climate variability on the daily streamflow is quantified as the difference in *NSE* from the model driven by OC forcings (Figure 3.3a) and by OC-IM forcings (Figure 3.3b), i.e., $NSE_{1,1} - NSE_{2,1}$. The role of IA climate variability on daily streamflow is quantified as the difference in *NSE* from the model driven by OC-IM (Figure 3.3b) and by OC-IM-IA (Figure 3.3c), i.e., $NSE_{2,1} - NSE_{3,1}$. Likewise, the role of IA climate variability on the daily streamflow variability is quantified as the difference in *NSE* driven by OC-IM-IA (Figure 3.3c) and by OC-IM-IA-ITA (Figure 3.3d), i.e., $NSE_{3,1} - NSE_{4,1}$. Note that, since $NSE_{4,j}$ represents the performance of the model forced with the mean climate, the modeled streamflow will approach the observed long-term average causing the *NSE* to be very close to zero. Recall, a value of "0" for *NSE* means that a model can only simulate the mean of the observed data. Similarly, the roles of the climate variabilities at the three timescales on monthly streamflow (j = 2), and annual streamflow (j = 3) are quantified based on Equation (3.16). For daily, monthly, and annual streamflow, the streamflow variability is decomposed into the fractional contributions from IM, IA, and ITA climate variability, therefore, the sum of the relative roles of the three climate variabilities equals 1 for each timescale streamflow, i.e., $\sum \rho_{k,j} = 1$, $k = IM, IA, ITA$, for each j.

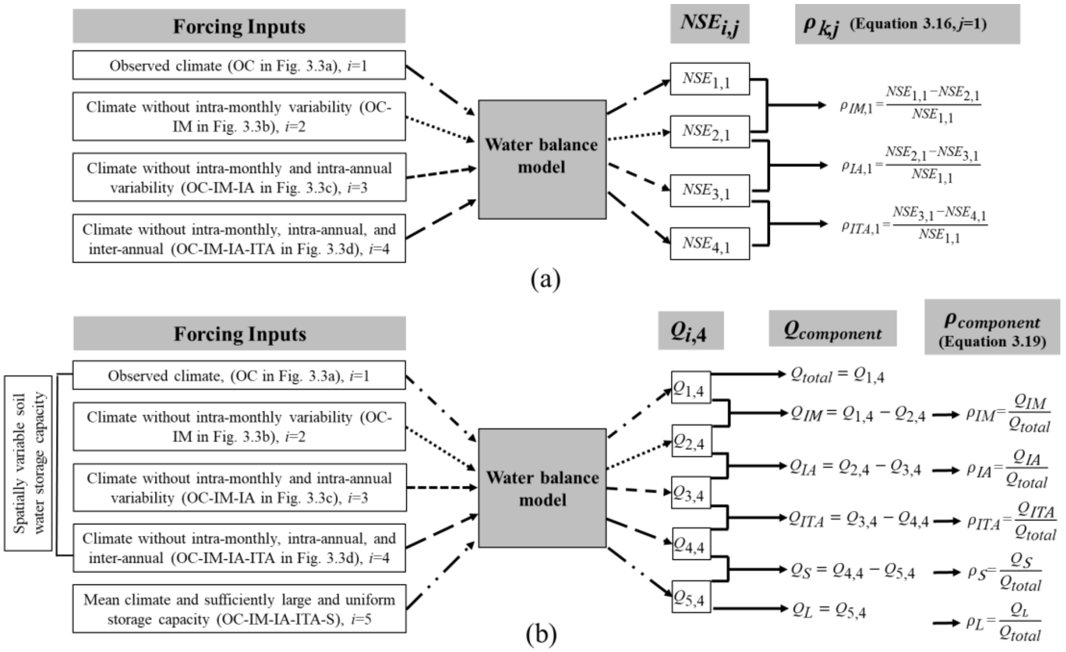

Figure 3.4: (a) The flow chart for quantifying the relative effects of climate variability on daily streamflow. $NSE_{i,j}$ represents the NSE value for the j^{th} timescale streamflow (j = 1, 2, 3 represents the daily, monthly, and annual streamflow, respectively, and j = 1 is shown in the figure for an example) forced by the i^{th} timescale climate forcing; $\rho_{k,j}$ denotes the role of climate variability (k= IM, IA, ITA) on streamflow, (b) The flow chart for quantifying the relative effects of different components on mean annual streamflow. The subscript "4" in $Q_{i,4}$ represents the streamflow at the mean annual scale, and the subscript i represents the five input scenarios. Q_{IM}, Q_{IA}, Q_{ITA}, Q_S, Q_L are the 5 components of the total mean annual streamflow caused by the IM climate variability, IA climate variability, ITA climate variability, storage capacity with its spatial variability, and mean climate, respectively; and ρ_{IM} , ρ_{IA}, ρ_{ITA}, ρ_S, ρ_L are the corresponding relative roles.

3.2.5.2 Mean Annual Water Balance

Following Milly (1994), the roles of climate variabilities on the mean annual water balance are defined as their contributions to the total streamflow generation and are quantified through the streamflow differences with different forcing inputs. In addition to the climate variability, the roles of the long-term average climate and soil water storage capacity with its spatial variability are evaluated for the mean annual water balance in order to compare to the results of other studies. The total mean annual streamflow in each catchment is decomposed into 5 components, as follows:

$$Q_{total} = Q_{IM} + Q_{IA} + Q_{ITA} + Q_S + Q_L \tag{3.17}$$

$$Q_{IM} = Q_{1,4} - Q_{2,4} \tag{3.18-1}$$

$$Q_{IA} = Q_{2,4} - Q_{3,4} \tag{3.18-2}$$

$$Q_{ITA} = Q_{3,4} - Q_{4,4} \tag{3.18-3}$$

$$Q_S = Q_{4,4} - Q_{5,4} \tag{3.18-4}$$

$$Q_L = Q_{5,4} \tag{3.18-5}$$

where the subscript "4" in $Q_{i,4}$ represents the streamflow at the mean annual scale, and the subscript *i* represents different forcings with a full range from 1 to 5; $Q_{1,4}$, $Q_{2,4}$, $Q_{3,4}$, and $Q_{4,4}$ are the simulated mean annual streamflow forced by OC, OC-IM, OC-IM-IA, and OC-IM-IA-ITA, as shown in Figure 3a, 3b, 3c, 3d, respectively. Climate variabilities at finer timescales promotes more streamflow generation, i.e., $Q_{1,4} > Q_{2,4} > Q_{3,4} > Q_{4,4}$. $Q_{1,4} \sim Q_{4,4}$ are simulated from the water balance model with spatially variable storage capacity. $Q_{5,4}$ (or Q_L) is the simulated streamflow forced by mean climate without considering the storage capacity, and we denote this model scenario as OC-IM-IA-ITA-S. Therefore, Q_{IM}, Q_{IA}, Q_{ITA}, Q_S, Q_L are the 5 components of the total mean annual streamflow caused by IM climate variability, IA climate variability, ITA climate variability, storage capacity with its spatial variability, and long-term average climate, respectively. By summing Equations (3.18-1) ~ (3.18-5) on both hand sides, it can be obtained that $Q_{IM} + Q_{IA} + Q_{ITA} + Q_S + Q_L = Q_{1,4}$. Comparing it with Equation (3.17), one can obtain $Q_{1,4} = Q_{total}$, i.e., $Q_{1,4}$ can be considered as the sum of different streamflow components. The contribution of each component is normalized by the total mean annual streamflow:

$$\rho_{component} = \frac{Q_{component}}{Q_{total}} \tag{3.19}$$

where $Q_{component}$ represents the components of total streamflow as mentioned in Equation (3.17); $\rho_{component}$ denotes the relative effects of climate variability or soil water storage capacity on the mean annual streamflow. The decomposition process and the role quantification process for the mean annual streamflow are shown in Figure 4b. Since the total volume of mean annual streamflow is decomposed into the fractional contributions from IM, IA, ITA climate variability, mean climate, and storage capacity with its spatial variability, the sum of the relative roles of these five components equals 1, i.e., $\sum \rho_{component} = 1$.

3.3 Results and Discussion

3.3.1 Model Performance

The calibrated parameters for 12 catchments (locations shown in Figure 3.10) are listed in Table 3.1. Values of the shape parameter (a) for these catchments are close to the upper limit (i.e., 2). Considering all catchments used in the study, the shape parameter values ranges from 1.85 to 1.90 for 4 catchments, with the remaining catchments having a value greater than 1.90, indicating an "S" shape of the cumulative distribution function (CDF) for soil water storage capacity (Wang, 2018). The "S" shape of a CDF curve consists of both a convex and a concave segment, which introduces more flexibility for simulating runoff generation under different wetness conditions (Jayawardena & Zhou, 2000).

The *NSE* values for the daily, monthly, and annual streamflow during calibration and validation periods are shown in Figure 3.5a and Figure 3.5b. Generally, *NSE* is greater at coarser timescales. The average *NSE* during the calibration (validation) period is 0.61 (0.61), 0.86 (0.84), 0.90 (0.85) for the daily, monthly, and annual streamflow, respectively. During validation, 53%

of catchments have an *NSE* value greater than 0.6 for daily streamflow, 79% of catchments have an *NSE* value greater than 0.8 for monthly streamflow, and 59% of catchments have an *NSE* value greater than 0.85 for annual streamflow. A comparison between the observed mean annual streamflow and simulation is presented in Figure 3.5c for all study catchments. The relative error for the validation period is 5.9% on average, and the root mean square error is 32.8 mm/year.

The percent bias (*PBIAS*) is calculated as well for evaluating the model performance. It is expected that the *PBIAS* will be small in all catchments during calibration period because the volumetric fit efficiency (*VFE*) effectively controls the model bias and it accounts for 50% of the weight in the objective function for calibration. Results show that the average *PBIAS* during the calibration period is -0.14%. Only 5 catchments have an absolute value of *PBIAS* between 0.5% and 6%, with all other catchments having an absolute value of *PBIAS* smaller than 0.5%. The cumulative probability of the *PBIAS* during validation is shown in Figure 3.5d. The average *PBIAS* during validation is -0.09% for all the catchments, and 87% of the catchments have a *PBIAS* within ±10%, indicating that no significant bias exists in the model (Moriasi et al., 2007; Gupta et al., 2009). Since the streamflow at a coarser timescale is aggregated from the daily streamflow, the percentage bias is same across different timescales. Note that the model performance is not dependent on the catchment drainage area (see Figure S3.1 in the Supporting Information).

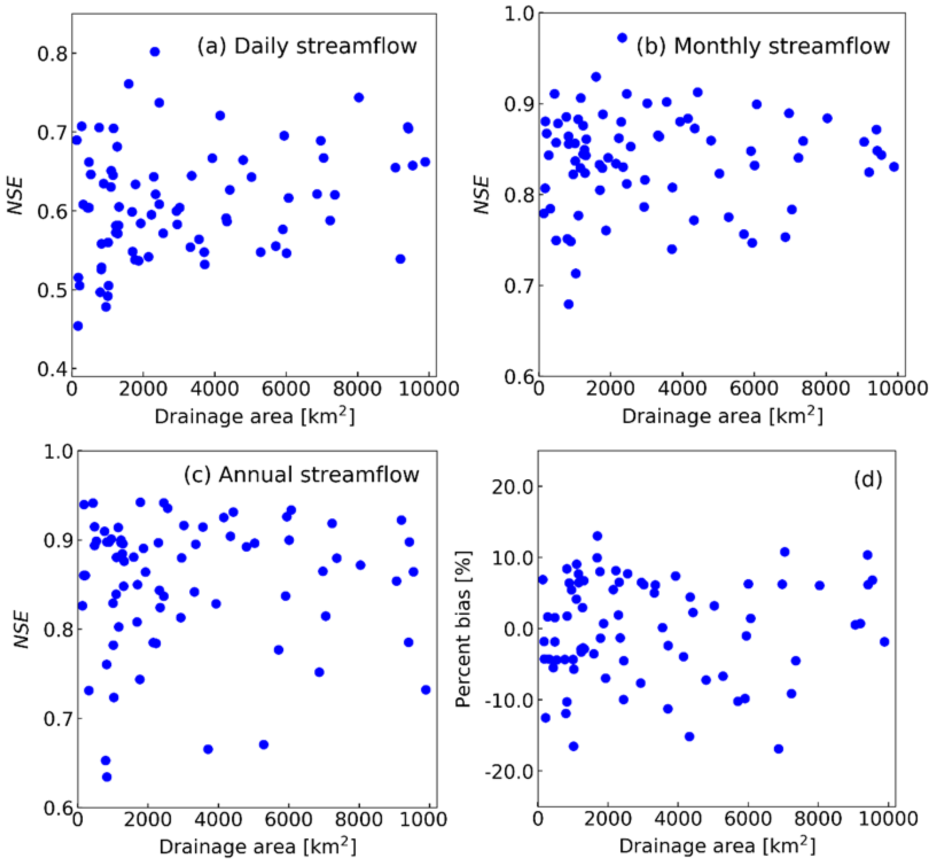

Figure S3.1: The relationship between drainage area and Nash-Sutcliffe Efficiency (*NSE*) values for (a) daily, (b) monthly, (c) annual streamflow, and (d) the relationship between drainage area and percent bias.

The model performance is satisfactory for the daily, monthly, annual, and mean annual water balance considering its parsimonious model structure (Perrin et al., 2001; McIntyre et al., 2005; Moriasi et al., 2007; Wang et al., 2009). To compare the model performance with other models, HyMOD (Moore, 1985) was used for all study catchments. The performance of the two models are shown in Figure S3.2 of the Supporting Information. The comparison shows that our model is superior to HyMOD in simulating the daily and monthly streamflow, and has a similar efficiency in simulating the annual streamflow. The average bias in simulating streamflow using the new PDM is smaller than the bias from HyMOD. Note that in the Supporting Information, the model used in this study is referred to as PDM-CN model for simplification since the distribution function for soil water storage capacity used in our PDM leads to the SCS-CN method.

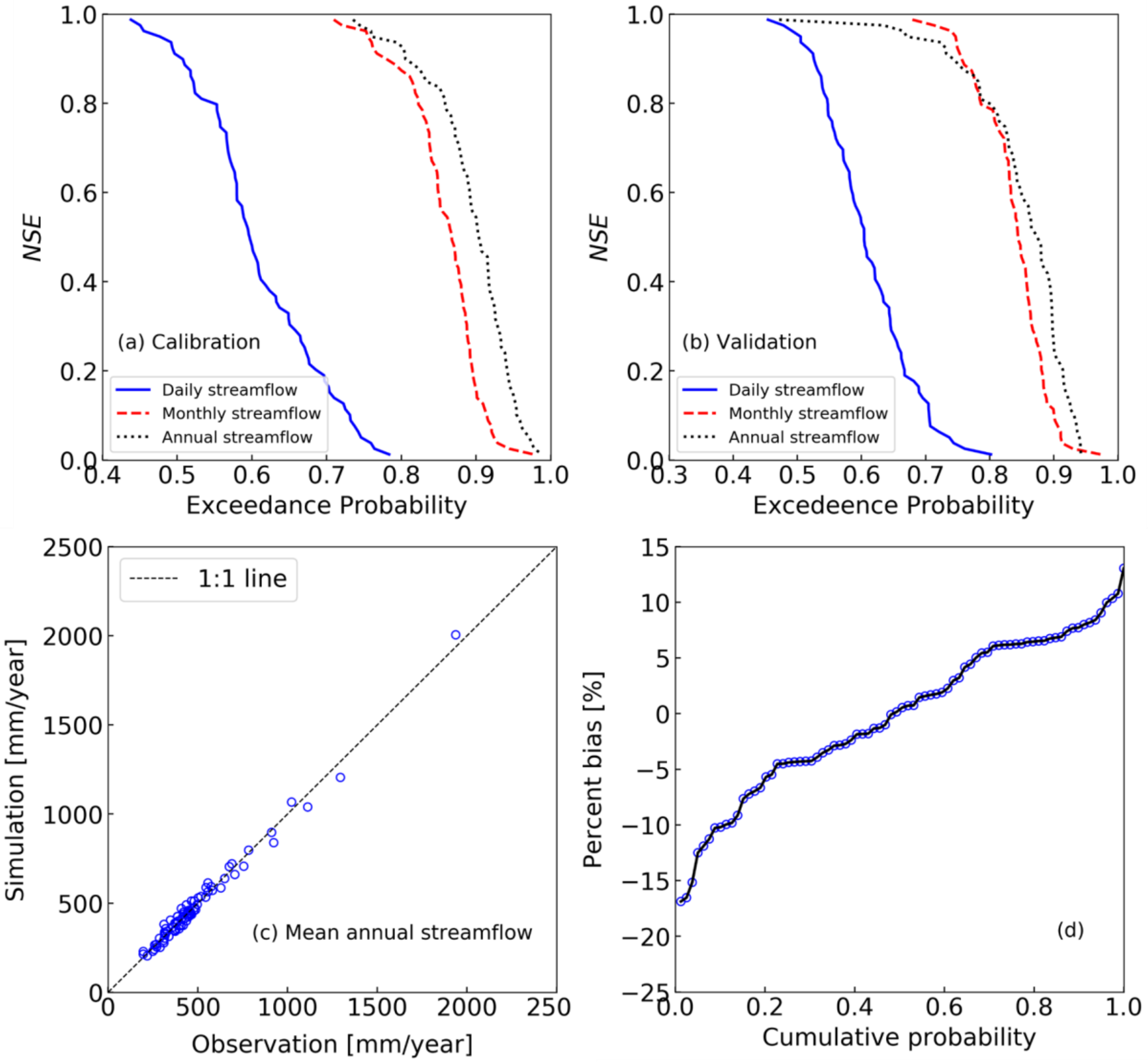

Figure 3.5: The performance of the water balance at different timescales: (a) NSE of the streamflows during the calibration period, (b) NSE of the streamflows during the validation period, (c) a comparison of the observed and calculated mean annual streamflow during the validation period, and (d) the cumulative distribution of model bias during the validation period.

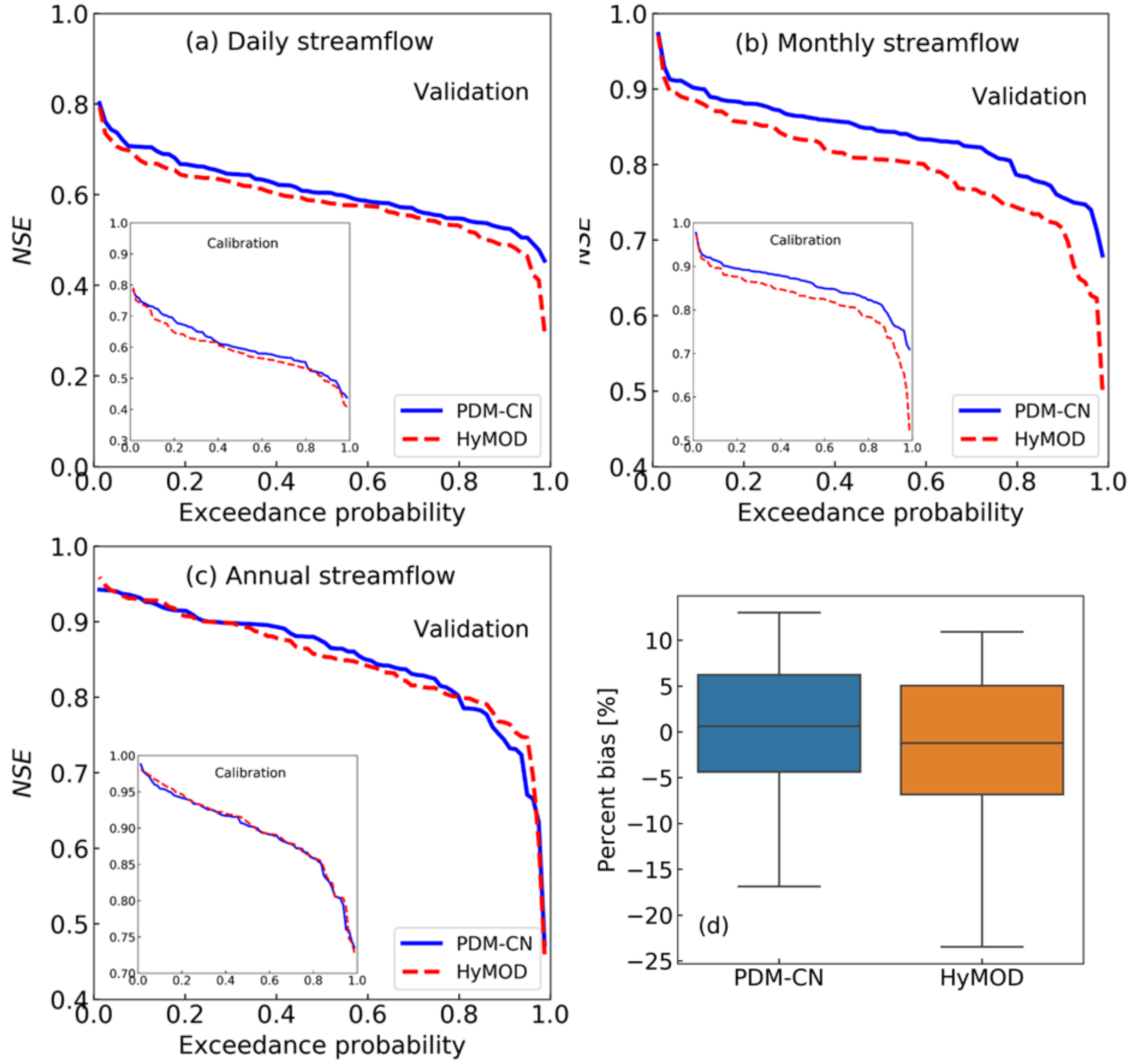

Figure S3.2: Comparisons between the model used in this study (PDM-CN) and the HyMOD in terms of the NSE during the validation and calibration periods for (a) daily streamflow, (b) monthly streamflow, (c) annual streamflow, and (d) the percent bias of streamflow during the validation period.

3.3.2 The Roles of Climate Variabilities on Streamflow

The relative roles of different climate variabilities on the streamflow at different timescales for the 78 study catchments are presented in Figure 3.6. In the daily streamflow, the average relative role of intra-monthly climate variability is the largest, accounting for 51.2% of the daily streamflow variability (Figure 3.6a). Intra-annual climate variability has the second most contribution, explaining 40.1% of the daily streamflow variability (Figure 3.6a). The relative role of inter-annual variability is much smaller, only explaining 8.7% of the daily streamflow variation. However, daily data are not fully accessible in many catchments, therefore, making it difficult to accurately simulate the daily streamflow. Additionally, the high contribution of the intra-annual variability indicates significant storage variation at the daily scale resulting from the intra-annual climatic fluctuations. Flashiness is one of the most significant characteristics of daily streamflow, thus the Richards-Baker flashiness index (*R-B* Index) (Baker et al., 2004) is calculated for daily streamflow during the validation period (1999-2015) to further present the sensitivity of daily streamflow to different climate variabilities. Streamflow with a larger *R-B* Index experiences a larger day-to-day variation. The results show that the *R-B* Index for the simulated streamflow with OC input is 0.26 on average among the study catchments, and is reduced to 0.02 when using OC-IM climate input. There is almost no flashiness in the simulated streamflow when OC-IM-IA climate is used, and there is no flashiness in streamflow using mean climate, i.e., OC-IM-IA-ITA. Figure 3.7a shows a three-year daily streamflow hydrograph with different climate inputs for Smith River in California (USGS gage number: 11532500). The difference in flashiness of the simulated streamflow modeled with different climate inputs further manifests the essential role played by intra-monthly climate variability on daily streamflow. Additionally, intra-annual climate variability generally determines the shape of daily streamflow at the monthly scale, and it is also a key component for daily streamflow variation.

In the monthly water balance, the role of intra-annual climate variability is the largest, on average explaining 75.4% of the variation in monthly streamflow (Figure 3.6b). The role of inter-annual climate variability is notable, contributing 17.6% of the monthly streamflow variation, while the role of intra-monthly climate variability is much smaller (7.0%). The central role of intra-annual climate variability on the monthly water balance is also supported by the Pardé coefficient, which is an indicator for identifying the mean seasonal flow regime (*Pardé*, 1933). Figure 3.7b shows the distribution of the Pardé coefficient for Smith River. The streamflow seasonality is almost fully determined by the intra-annual climate variability since other climate variabilities explain less variation in monthly streamflow. The overwhelming control of the intra-annual climate variability on the monthly streamflow variability reduces the difficulty in model prediction compared to the daily timescale because monthly climatic data are more accessible. The much smaller role of the intra-monthly variability indicates that the irregular effects of daily storminess are smoothed out at the monthly scale by the soil water storage capacity. This is supported by *Wang et al.* (2011) which found that the daily inputs did not improve the performance of the monthly water balance much, through comparing a monthly water balance model with two daily water balance models in simulating the monthly streamflow. Figure 3.8a shows the relative role of intra-annual climate variability on monthly streamflow variation as a function of dryness index. In wetter areas, more variance in monthly streamflow could be explained by the intra-annual climate variability than in drier areas. However, the intra-annual climate variability still explains more than half of the variation in monthly streamflow for drier catchments.

In the annual water balance, the inter-annual climate variability explains the most variation (81.4% on average) in the annual streamflow (Figure 3.6c). The intra-annual climate variability also has a considerably contribution (17.5%). However, the impacts of intra-monthly variability are further diluted in the annual streamflow compared to that in the monthly streamflow. Figure 3.7c shows the simulated annual streamflow in Smith River with different climate inputs. The power of inter-annual climate variability over annual streamflow can also be reflected by the coefficient of variation (*CV*) of simulated annual streamflow. The *CV* value increases from 0, when using mean climate, to 0.0155 using annually variable climate and does not change much with smaller timescale climate variability indicated by Figure 3.7c. Figure 3.8b shows that the relative contribution of inter-annual climate variability on the annual streamflow variation is larger in wetter catchments than in drier catchments. In some humid catchments, the contribution of the inter-annual variability is up to 100%. Figure 3.8c shows a positive relationship between the relative role of intra-annual climate variability on the annual streamflow and the dryness index. Therefore, the impact of intra-annual variability is larger in drier regions. This result generally agrees with the result from Milly and Dune (2002), which found that the inter-annual variance in streamflow was explained more by annual climate anomalies than by seasonality, especially in humid catchments. Figure 3.8b and 3.8c show the significant controls of the mean climate (in terms of dryness index) on the relative sensitivity of annual streamflow to different climate variabilities. The large scatter in Figure 3.8b-c indicates that other catchment characteristics also have contribution in determining the relative role of climate variability.

Figure 3.6d shows the relative roles of each climate variability on the mean annual streamflow. Note that the values in Figure 3.6d are not supposed to be compared with values of relative roles from the water balance at smaller timescales (Figure 3.6a-c), because the method to calculate the relative roles of climate variability on the mean annual streamflow is different. Among different climate variabilities, intra-annual climate variability is the most important, contributing 64.2%, on average, to the part of mean annual streamflow that generated by climate variabilities. It should be pointed out that the inter-annual climate variability also plays a substantial role in the mean annual streamflow, contributing 22.4%, on average, to the climate variability-generated mean annual streamflow. This result supports a previous research in *Li*

(2014), which showed that the inter-annual variability of precipitation and potential evapotranspiration reduces the mean annual evapotranspiration based on a stochastic soil moisture model. The reduction in evaporation ratio can reach 8-10% for the range of precipitation and potential evapotranspiration variability used in the study, which means that the inter-annual climate variability promotes the streamflow generation.

Figure 3.6 shows that at the daily, monthly, and annual timescales, the variation in streamflow is largely determined by the climate variability at the same temporal scale. Specifically, for the annual streamflow, the inter-annual variability plays the most important role, and so on. Following this pattern, the long-term climate condition (in terms of dryness index) should be most important for the mean annual water balance; this claim has been widely confirmed in other studies (Budyko, 1958, 1974; Milly, 1994; Zhang et al., 2001; Yang et al., 2008; Gentine et al., 2012).

The relative roles of climate variability have also been evaluated based on simulation results from HyMOD. The results from the model developed in this paper and that based on HyMOD are summarized in Table S3.1 and S3.2, respectively. It shows that the results from these two models are consistent. It is possible that a different combination of weights in the objective function could lead to different model efficiency. However, the relative contribution of each climate variability is normalized by the model behavior from the observed daily climate as shown in Equations (3.16) and (3.19), which suggests an insensitivity of the relative effects of climate variability to the weights used in calibration. Moreover, Table S3.3 in the Supporting Information shows the results of the relative roles of climate variability based on the simulation results with the parameters calibrated by *NSE* only (not using *VFE*). As shown in Table S3.1 and Table S3.3, no noticeable difference is observed between the results from the two calibration objective functions (i.e., *NSE* and *VFE* versus *NSE* only).

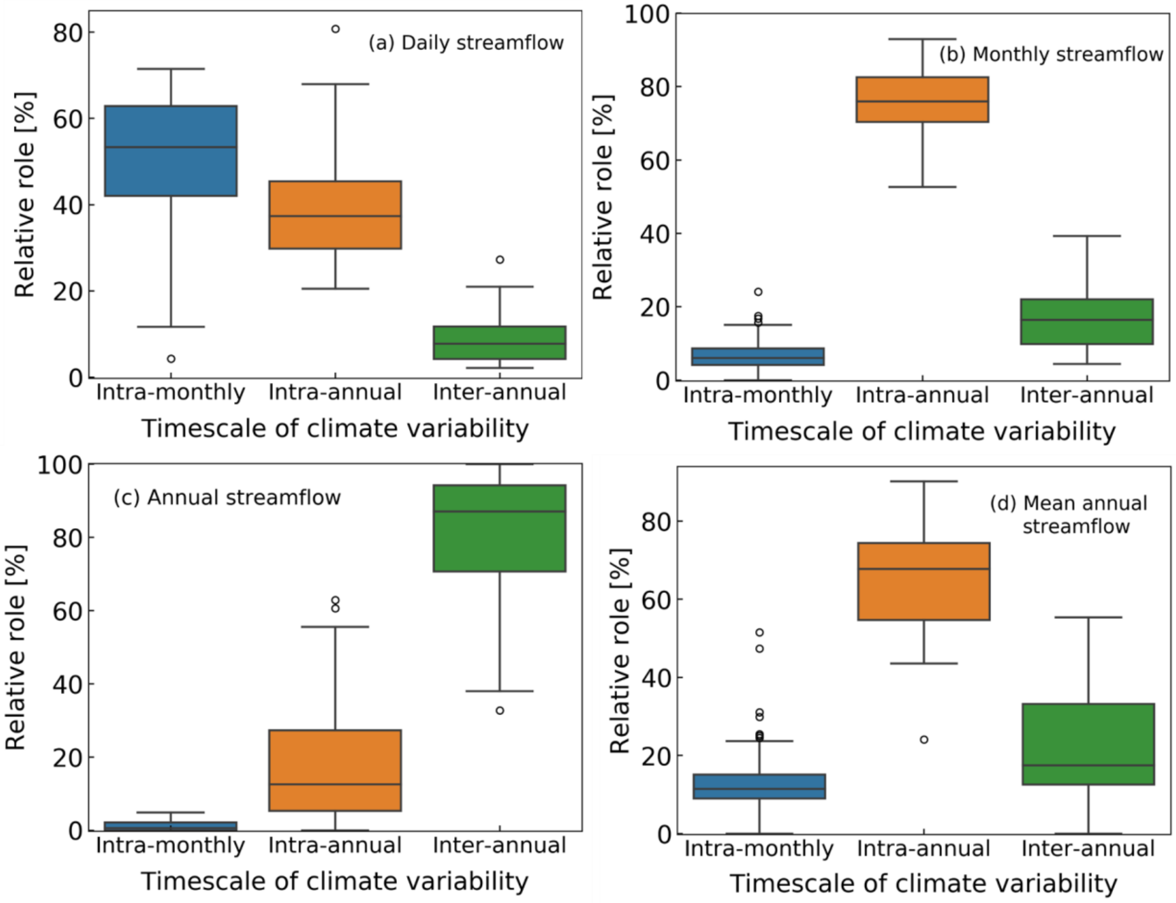

Figure 3.6: The relative roles of climate variability on streamflow at the (a) daily, (b) monthly, (c) annual, and (d) mean annual scales.

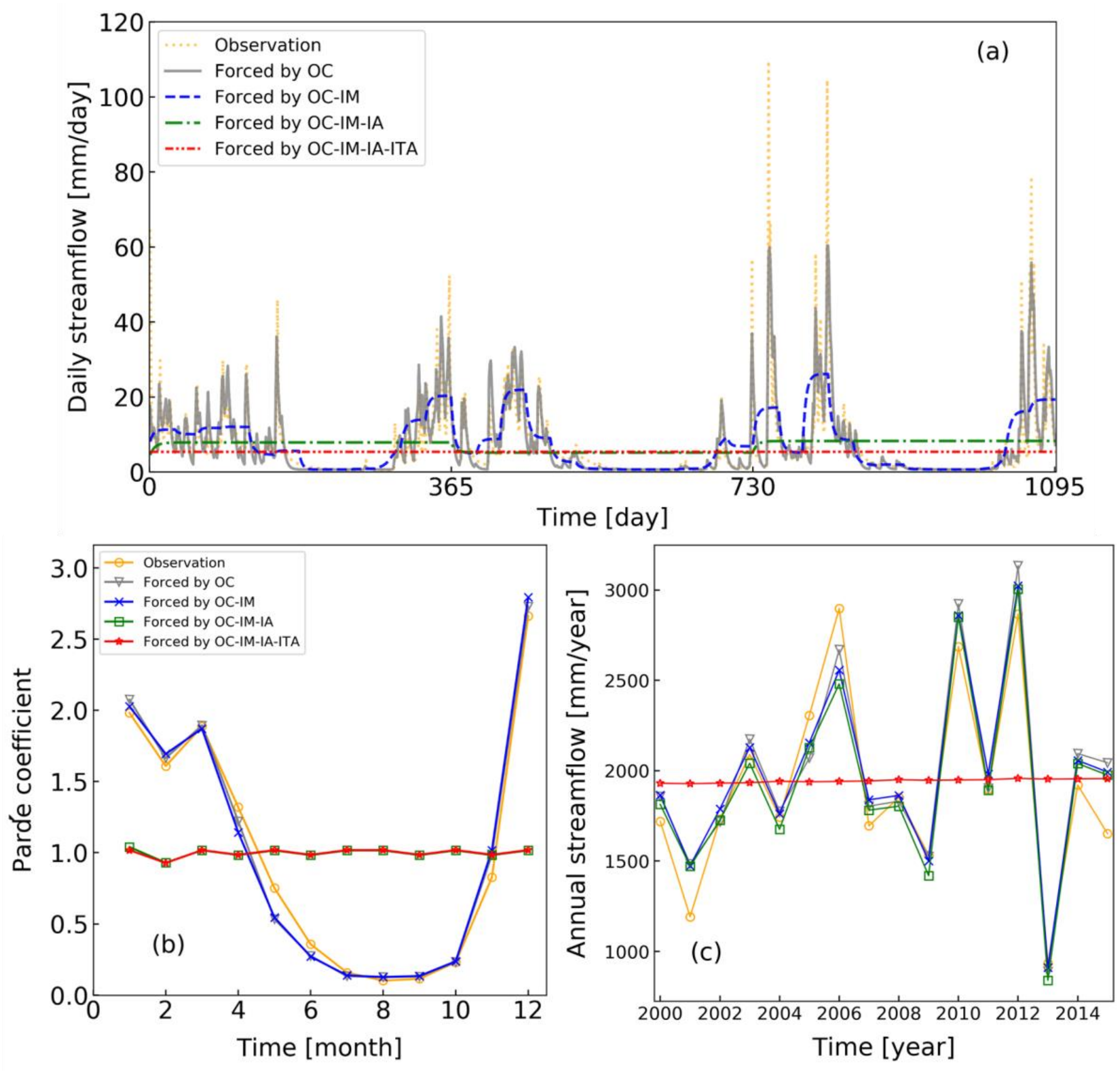

Figure 3.7: Controls of climate forcings and its variability on (a) daily streamflow during 2010-2012, (b) mean Pardé coefficient for each month during the 2000-2015, and (c) annual streamflow during 2000-2015 in Smith River, California (USGS gage number: 11532500).

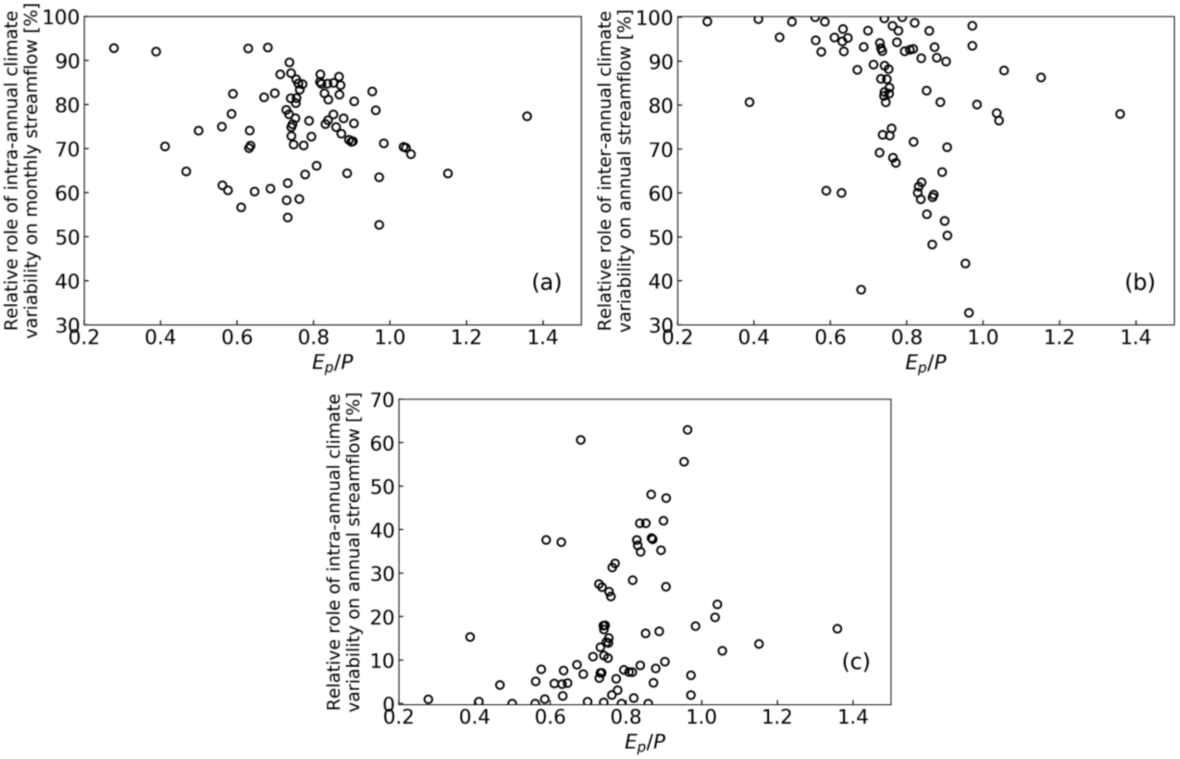

Figure 3.8: (a) The relationship between the relative role of intra-annual climate variability on monthly streamflow and dryness index (Ep/P), (b) the relationship between the relative role of inter-annual climate variability on annual streamflow and Ep/P, (c) the relationship between the relative role of intra-annual climate variability on annual streamflow and Ep/P.

Table S1: The relative roles (%) of climate variability on streamflow based on simulation results from PDM-CN with model parameters calibrated by both NSE and Volumetric Fit Efficiency (*VFE*).

Timescale of streamflow	**Timescale of climate variability**		
	Intra-monthly	Intra-annual	Inter-annual
Daily$^+$	51.2	40.1	8.7
Monthly$^+$	7.0	75.4	17.6
Annual$^+$	1.2	17.5	81.4
Mean annual*	1.4	7.8	2.9

+ The relative roles for daily, monthly, and annual streamflow are quantified by Equation 3.16
* The relative roles for mean annual streamflow are quantified by Equation 3.19

Table S2: The relative roles (%) of climate variability on streamflow based on simulation results from HyMOD with model parameters calibrated by both *NSE* and *VFE*.

Timescale of streamflow	**Timescale of climate variability**		
	Intra-monthly	Intra-annual	Inter-annual
Daily	51.9	38.9	9.2
Monthly	7.7	73.8	18.5
Annual	1.6	17.6	80.8
Mean annual	2.2	8.7	3.4

Table S3: The relative roles (%) of climate variability on streamflow based on simulation results from PDM-CN with the model parameters calibrated by only *NSE*.

Timescale of streamflow	**Timescale of climate variability**		
	Intra-monthly	Intra-annual	Inter-annual
Daily	51.0	40.3	8.7
Monthly	7.0	75.6	17.4
Annual	1.1	16.9	82.1
Mean annual	1.3	7.7	2.9

3.3.3 Budyko Framework

In addition to the climate variability, the direct contributions of the mean climate and soil water storage capacity are also evaluated in the mean annual water balance (Figure 3.9). Among all the factors, the mean climate is the dominant factor controlling the precipitation partitioning, contributing 58.6 %, on average, to the mean annual streamflow. The soil water storage capacity with its spatial variability is the second contributing factor and contributes on average 29.3% of the mean annual streamflow. The spatial heterogeneity of soil water storage not only promotes the streamflow generation directly but also suppresses the evaporation over the catchment as shown in Figure 2. The impact of daily storminess on the mean annual water balance is small for the study catchments. This result is similar to Reggiani (2000) who found that the storminess has an almost negligible effect on the mean annual water balance when infiltration excess runoff is negligible.

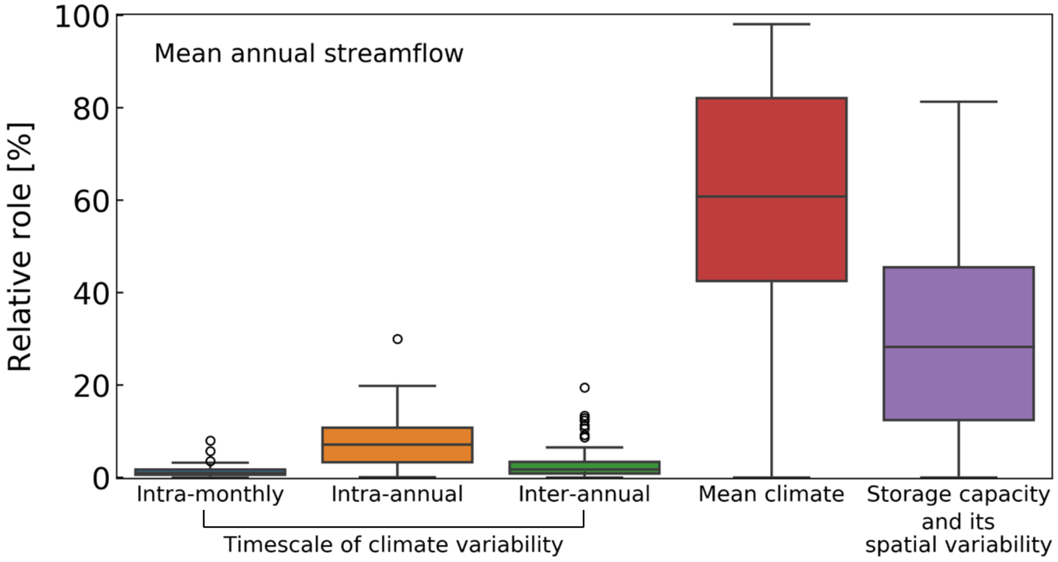

Figure 3.9: The relative roles of intra-monthly, intra-annual, inter-annual climate variability, mean climate, soil water storage capacity and its spatial variability on the mean annual streamflow across the catchments.

Figure 3.10 shows how the mean annual evaporation ratio (i.e., $\frac{E}{P}$) for the 12 catchments in Table 3.1 deviates from the asymptotes (black dashed lines) in the Budyko framework. Each data point in Figure 3.10 (except for the observation) is a simulated evaporation ratio using the indicated forcing for each catchment. When neglecting climate variability and soil water storage capacity as well as its spatial heterogeneity, the mean annual evaporation of a catchment is the highest (red circles), falling on the asymptotes (dashed black lines). In a catchment with a dryness index smaller than 1, the evaporation is equal to the potential evapotranspiration. Conversely, a catchment with a dryness index larger than 1, the evaporation is equal to precipitation. A horizontal line with $\frac{E}{P} = 1$, is referred to as the upper bound in this paper (dashed dotted red line) which is not possible exceeded at the mean annual scale because of mass balance principle. The deviation from the upper bound (dashed dotted red line) to the asymptotes (dashed black lines) could be interpreted as the direct contribution of mean climate to mean annual streamflow. This deviation decreases to 0 when the dryness index is greater than 1. It suggests that the mean climate has direct contribution to mean annual streamflow only in catchments with a dryness index less than 1. The direct contribution from mean climate to the mean annual streamflow is the remaining amount of precipitation after the possible maximum evaporation; under this condition climate variability and soil water storage capacity are not considered. The catchments with dryness index less than 1 have the possible maximum evaporation less than precipitation. However, the mean climate can play roles in streamflow generation in drier areas through the coevolution with other catchment properties such as the soil water storage capacity and vegetation. Soil water storage capacity and climate variability promote streamflow generation, therefore, the evaporation ratio further deviates from the asymptotes when more factors are considered and eventually approaches the observed value when all factors are considered (Milly, 1994; Westhoff et al., 2016).

The contribution of each catchment characteristic to the mean annual streamflow versus dryness index ($\frac{E_p}{P}$) is shown in Figure 3.11. It is apparent that the direct contribution of mean climate decreases with dryness index and is 0 for catchments when the dryness index is equal to or larger than 1 (Figure 3.11a). Other catchment characteristics including the storage capacity interact with the local climate, therefore, a clear pattern would also be found between the relative role of the spatially variable storage capacity with the dryness index (Figure 3.11b). The contributions of storage capacity and climate variabilities increase as climate becomes drier (Figure 3.11b, c, d). The scatter in Figure 3.11 suggests that the contribution of each component is not only dependent on the mean climate but also other unconsidered factors (e.g., sub-daily rainfall variability and topography).

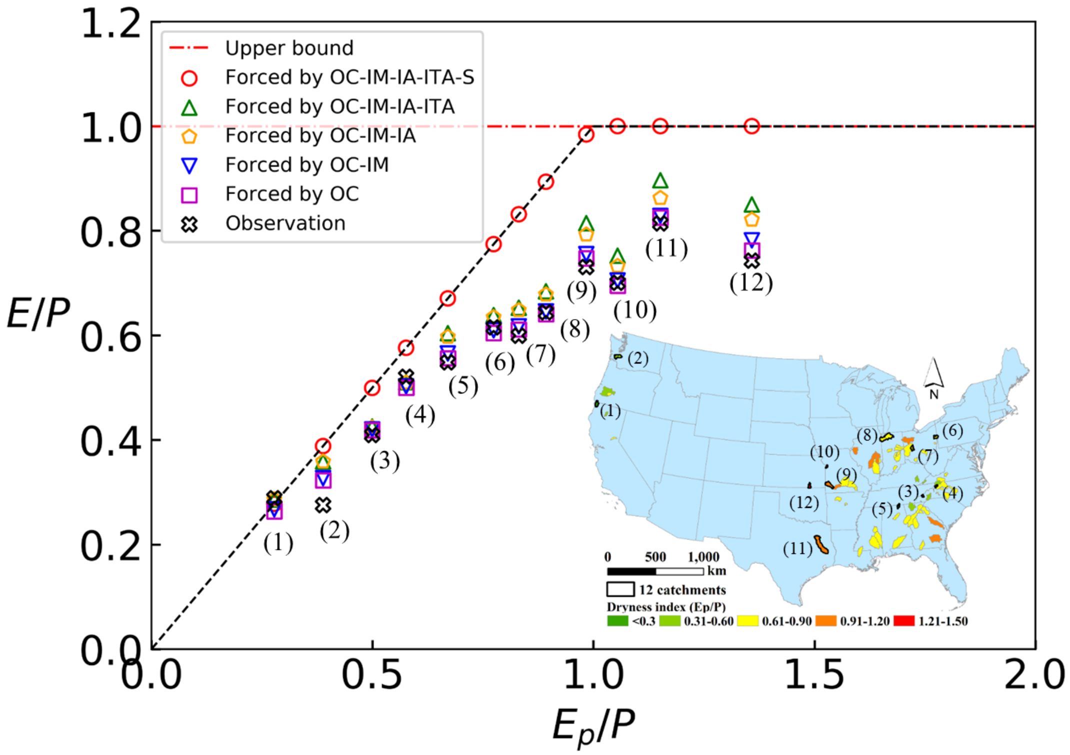

Figure 3.10: The effects of soil water storage capacity and its spatial variability, mean climate, inter-annual climate variability, intra-annual climate variability, and intra-monthly climate variability on the mean annual evaporation ratio (*E/P*) in the Budyko framework.

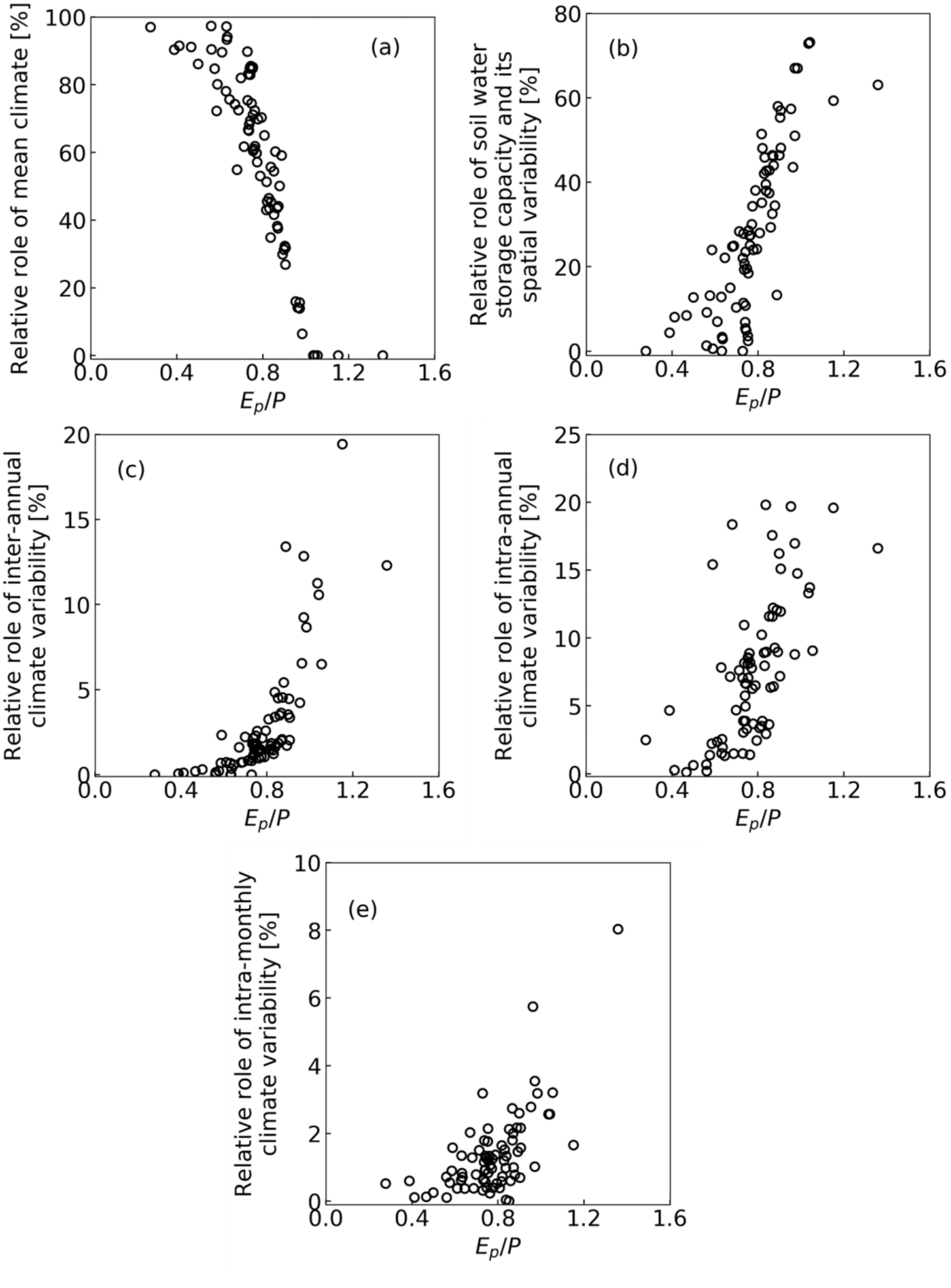

Figure 3.11: The relationships between the climate dryness index (Ep/P) and the relative effects of (a) mean climate, (b) soil water storage capacity and its spatial variability, (c) inter-annual climate variability, (d) intra-annual climate variability, and (e) intra-monthly climate variability on the mean annual streamflow.

3.3.4 A Unified Framework for Water Balance Models

The developed daily water balance model provides a unified framework for modeling streamflow at different timescales. For the traditional daily, monthly, annual, and long-term water balance models, the timescale and time step of climate inputs are same as those of streamflow to be modelled (Figure 3.12). For example, monthly water balance models (Thomas, 1981; Makhlouf & Michel, 1994) take monthly precipitation and potential evapotranspiration as the inputs as shown in Figure 3.12-b1. Model complexity and parameter uncertainty is a trade-off during model development (Perrin et al., 2001; Zhang et al., 2008). Generally, as the model timescale becomes coarser, the model performance is not sacrificed in return for simpler model complexity (Jothityangkoon et al., 2001). But the model complexity as well as the number of parameters should be flexible in different catchments and based on different research purposes. Assuming the time lag for the quick storage tank is much less than one month, the monthly water balance model is obtained by removing the routing of quick storage as shown in Figure 3.12-b2 (i.e., k_d=1 in Equations 3.13-4 and 3.13-5) and the Equations for the remaining components are same as those of daily water balance model. The monthly water balance model shown in Figure 3.12-b2 has a similar performance as the ‘abcd’ model (see Figure S3.3 in Supporting Information), which is a state-of-the-art monthly water balance model with 4 parameters (Thomas, 1981). In Equation (3.3), precipitation is partitioned into soil wetting and runoff; whereas, in the ‘abcd’ model, the sum of precipitation and initial storage is partitioned into runoff and the sum of ending storage and evaporation. However, Equation (3.3) with $S_0 = 0$ leads to the same functional form as the ‘abcd’ model for calculating runoff. Assuming that the time lag for the slow storage tank is less than one year, the routing of slow storage could be removed, resulting in the two-parameter (a, S_b) annual model as shown in Figure 3.12-c2 (i.e., k_d =1 in Equations 3.13-4 and 3.13-5, and k_b=1 in

Equations 3.13-6 and 3.13-7). Driven by annual precipitation and potential evapotranspiration (Figure 3.12-c1), the annual water balance model calculates annual soil wetting (and streamflow as $P - W$) by Equation (3.3) and annual evaporation by Equation (3.12). The soil water storage carryover in the annual water balance model is considered through the initial storage in Equation (3.3).

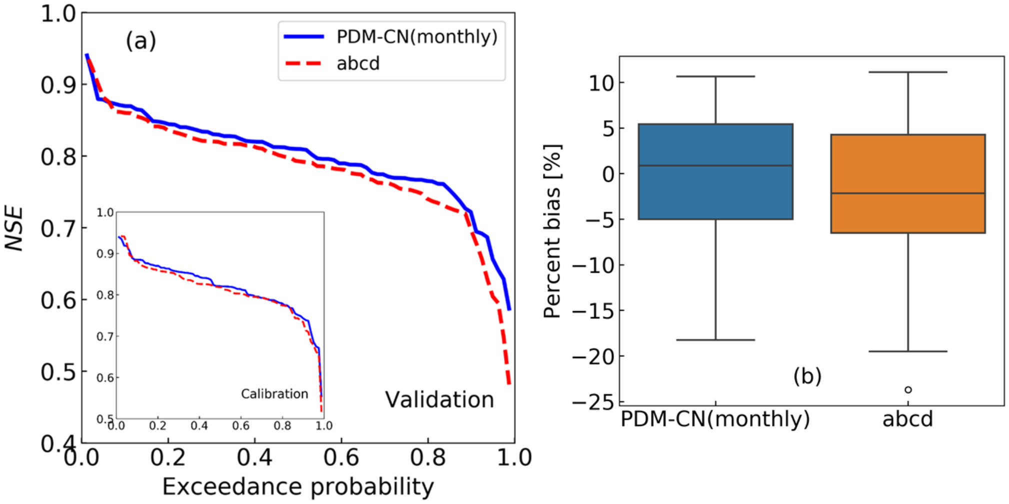

Figure S3.3: Comparisons between the monthly PDM-CN model in the unified model framework and the 'abcd' model in terms of (a) the *NSE* for streamflow during the calibration and validation periods, and (d) the percent bias of streamflow during the validation period.

Since soil water storage carry-over is not necessary for mean annual water balance, the mean annual water balance model is obtained by removing the initial soil water storage (i.e., $S_0 = 0$) from the annual water balance as shown in Figure 3.12-d2. Equation (3.3) becomes:

$$W = \frac{P+S_b-\sqrt{(P+S_b)^2-2aS_bP}}{a} \tag{3.20}$$

Substituting Equation (3.20) into Equation (3.12) and dividing P on both hand sides, one obtains:

$$\frac{E}{P} = \frac{\Phi^{-1}+1-\sqrt{(\Phi^{-1}+1)^2-2a\Phi^{-1}}}{a} \cdot \frac{\frac{E_p}{P}+\Phi-\sqrt{\left(\frac{E_p}{P}+\Phi\right)^2-2a\Phi\frac{E_p}{P}}}{a} \tag{3.21}$$

where $\Phi = \frac{S_b}{P}$ is soil storage index. Equation (3.21) shows that $\frac{E}{P}$ is a function of $\frac{E_p}{P}$, Φ, and a. This mean annual water balance model can be interpreted as the two-stage precipitation partitioning (L'vovich, 1979). At the first stage, a portion of precipitation is partitioned to soil wetting; at the second stage, a portion of soil wetting is partitioned into evaporation. If all the precipitation becomes soil wetting at the first stage (i.e., $P = W$), the two-stage partitioning is simplified as a one-stage partitioning (i.e., precipitation is partitioned into evaporation and streamflow directly). For the one-stage partitioning, the available water for evaporation is precipitation, and the average soil water storage capacity (i.e., S_b) in Figure 3.12-d2 is set as P. Correspondingly, Equation (3.21) becomes the one-parameter Budyko Equation (Wang and Tang, 2014):

$$\frac{E}{P} = \frac{\frac{E_p}{P}+1-\sqrt{\left(\frac{E_p}{P}+1\right)^2-2a\frac{E_p}{P}}}{a} \tag{3.22}$$

The five-parameter daily water balance model (Figure 3.12a), which unifies the probability distributed model and the SCS-CN method (Wang, 2018), can be easily modified to a coarser modeling timescale by removing unnecessary components (Figures 3.12b, c, d). The Equations for the common components among different timescale models remain the same. The four-parameter monthly model (Figure 3.12b) is obtained by removing the routing of quick flow; and the two-parameter annual model (Figure 3.12c) is obtained by further removing the routing of slow flow; the two-parameter mean annual model (Figure 3.12d) is obtained by neglecting initial storage in the annual model. The two-parameter mean annual model (Equation 3.21) can be further simplified as a one-parameter Budyko model (Equation 3.22). However, the HyMOD cannot lead to the Budyko model by the same simplification. It should be noted that the common parameters (e.g., a) among the different timescale models (Figure 3.12) have different values due to the timescale effect (Deng et al., 2018). To avoid the effect of climate timescale on model parameters, precipitation and potential evapotranspiration at the daily time step (Figure 3.3) can be used for modelling streamflow at different timescales. In this case, the common parameters for modeling streamflow at different timescales have the identical values.

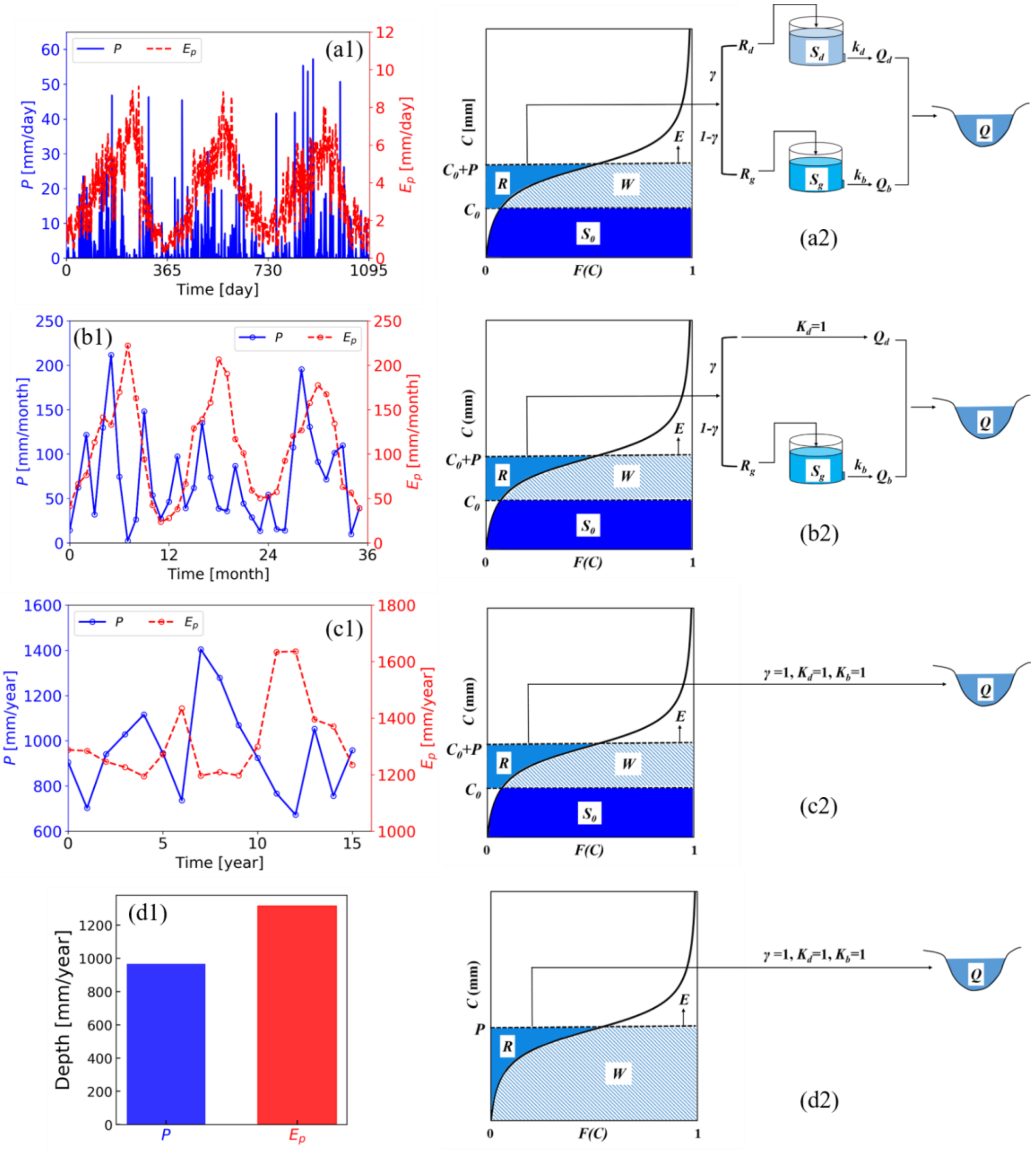

Figure 3.12: Climate inputs at different timescales (left column) and their corresponding water balance model structures (right column): (a) daily model, (b) monthly model, (c) annual model, (d) mean annual model.

3.4 Conclusion

A probability distributed model was developed based on a new distribution function for describing the spatial variability of soil water storage capacity which leads to the SCS-CN method. In this study, the spatial variability of the soil water storage was assumed to have impacts on both runoff generation and evaporation. The daily water balance model built in this study provides a framework for unifying water balance from daily to mean annual scale. Parameters (5 in total) were calibrated using the SCE-UA algorithm with the objective function being the weighted combination of Nash-Sutcliffe efficiencies and volumetric fit efficiencies from daily, monthly, and annual streamflow. The relative effects of climate variabilities, i.e., intra-monthly, intra-annual, and inter-annual variability of precipitation and potential evapotranspiration, on the streamflow at different timescales were evaluated by comparing the simulated streamflow from different timescale climate scenarios. The results show that at the daily, monthly, and annual scales, streamflow variation is mostly influenced by the climate variability at the same timescale. Daily streamflow receives significant contribution from intra-annual climate variability but much smaller contribution from inter-annual climate variability. Monthly streamflow is notably affected by inter-annual climate variability, and annual streamflow is considerably affected by intra-annual climate variability. As for the mean annual streamflow, intra-annual climate variability is the predominant contributor among all the climate variabilities, and our study shows that inter-annual climate variability affects the mean annual streamflow considerably.

It should be noted that this study only tried to investigate the relative roles of different climate variabilities in a broader sense, while other catchment characteristics are not explored thoroughly but are also important to the water balance. This study helps gain insight into the general control of the climatic fluctuations on the water balance. While, the results from this paper are more applicable to humid catchments since the model developed is a saturation excess model. Infiltration excess regime will be incorporated in future research.

CHAPTER FOUR: COMBINED EFFECTS OF WATER STORAGE CAPACITY AND CLIMATE ON LONG-TERM BASEFLOW

4.1 Introduction

Baseflow originates from groundwater and subsurface storage (Payn et al., 2012; Richardson et al., 2020; Segura et al., 2019), therefore it is a relatively stable component of the total streamflow (Brutsaert & Nieber, 1977; Shaw et al., 2013; Wang & Cai, 2009). With continued population growth and changing climate, changes in baseflow is of interest in impacting water availability (Ficklin et al., 2016; Miller et al., 2016; Tan et al., 2020). Baseflow discharge affects the transport and concentration of contaminants in rivers, and thus is closely related to water quality (Gomez-Velez et al., 2015; Jordan et al., 1997). As an integral part of natural flow regime, baseflow is also crucial for maintaining aquatic ecosystems since it is associated with various physicochemical aspects of streams such as water temperature and channel geomorphology besides water quantity and quality (Hare et al., 2021; Poff et al., 1997; Price, 2011). Hence, understanding the controls of baseflow generation is of great importance to advance hydrologic sciences.

Since baseflow is one of the reflections of the catchment's hydrological functioning, it is expected that both climate forcings and physical catchment properties control mean annual baseflow (Price, 2011). Baseflow is commonly quantified using two metrics: baseflow index – defined as the ratio of mean annual baseflow to mean annual streamflow, and baseflow coefficient – defined as the ratio of mean annual baseflow to mean annual precipitation. These normalized characteristics of baseflow facilitate revealing general relationship between baseflow and climate forcings and physical catchment properties across various water resources regions, and lead to fundamental understanding of spatial variability of long-term water balance. Sivapalan et al.

(2011) and Wang & Wu (2013) identified the relative availability of mean annual water (precipitation) and energy (potential evapotranspiration) as the primary determinant controlling the baseflow coefficient in the contiguous U.S. Meira Neto et al. (2020) developed analytical solutions with similar assumptions as Budyko Equation and further demonstrated the role of mean annual climate on baseflow in the U.S. Besides mean annual climate, seasonality of precipitation and potential evapotranspiration was shown to affect baseflow as well (Beck et al., 2013). Further, landscape characteristics, including geology, topography, and soil type, have also been found to exert significant control on baseflow (Haberlandt et al., 2001; Mwakalila et al., 2002). For example, Longobardi & Villani (2008) found that catchment permeability is a major factor affecting baseflow index in a Mediterranean region. In addition to permeability, Santhi et al. (2008) found that relief and gradient are highly correlated to baseflow volume and baseflow index in the U.S. Bloomfield et al. (2009) argued that catchment lithology has the first-order control on the baseflow index in a basin located in the U.K.

However, there was no general consensus on which index is most useful in capturing the impacts of catchment landscape, and how climate and landscape play relative roles on mean annual baseflow across different geographical regions and climatic settings. Recently, Gnann et al. (2019) disentangled the impacts of mean annual climate and landscape based on the generalized proportionality relationship (Ponce & Shetty, 1995). By applying their method to catchments from both the continental U.S. and U.K., they found that catchment wetting potential, a parameter which indicates the catchment soil water storage capacity, is essential to explain the different responses of long-term baseflow in different regions. Soil water storage capacity could be considered as a comprehensive index characterizing catchment landscape since it is related to various landscape properties such as topography and the hydraulic property of soil (Gao et al., 2019; Huang et al., 2003; McGuire et al., 2005). A direct dependence between soil water storage capacity and baseflow generation is intuitive as a larger storage capacity could retain more precipitation given a precipitation depth and antecedent soil moisture condition. Moreover, the spatial variability of storage capacity within a catchment influences runoff generation directly as well (Jothityangkoon et al., 2001; Liang et al., 1994; Milly, 1994; Moore, 1985). Lacey & Grayson (1998) found that the accurate description of spatial variability of geology could reduce the prediction error of baseflow index significantly, supporting the importance of the spatial variability of landscape in affecting baseflow index.

However, the role of soil water storage capacity on mean annual baseflow is not yet fully quantitatively expressed. The wetting potential parameter in the generalized proportionality relationship is helpful in explaining the baseflow variability between catchments concluded by Gnann et al. (2019). However, the quantitative relationship between wetting potential and catchment soil water storage capacity is not clear. Therefore, the purpose of this study is to encompass catchment soil water storage capacity in a probability distribution model directly by incorporating a cumulative distribution function of soil water storage capacity, and to investigate the roles of climate and soil water storage capacity on mean annual baseflow quantitatively. Analysis of this study will advance the understanding of spatial variability in precipitation partitioning across catchments.

The remaining part of the paper proceeds as follows. Section 4.2 describes the analytical expressions for mean annual water balance and also provides a method for analyzing the role of climate variability on baseflow, the study catchments and data along with the parameter estimation technique. Section 4.3 discusses the controls of mean annual climate, soil water storage capacity, and climate variability on baseflow index and baseflow coefficient in the study catchments. Section 4.4 provides the emerging conclusions from the study.

4.2 Methodology

4.2.1 Two-stage Partitioning of Mean Annual Precipitation

Long-term water balance is usually formulated as a one-stage precipitation partitioning process, in which, mean annual precipitation (P) is partitioned into mean annual streamflow (Q) and evaporation (E), with an assumption of steady-state storage condition (Budyko, 1974; Zhang et al., 2001):

$$P = Q + E \tag{4.1}$$

where Q could be further partitioned into fast flow (Q_f) and slow flow also called baseflow (Q_b):

$$Q = Q_f + Q_b \tag{4.2}$$

Q_f includes infiltration excess and/or saturation excess runoff and subsurface flow; and Q_b is from groundwater discharge. To study the long-term baseflow explicitly, Q_b and Q_f need be differentiated; therefore, the two-stage precipitation partitioning framework is adopted in this paper. The two-stage partitioning framework is an empirical analysis proposed by L'vovich (1979) on the basis of data from a large number of catchments around the world, and this framework describes the fundamental catchment functions explicitly at the annual scale (Troch et al., 2009). At the first stage, P is partitioned into Q_f and catchment wetting or infiltration (W):

$$P = Q_f + W \tag{4.3}$$

At the second stage, W is further partitioned into Q_b and E:

$$W = Q_b + E \tag{4.4}$$

The units for P, Q, E, Q_f, Q_b, and W are mm.

4.2.2 Mean Annual Baseflow

As mentioned in the Introduction, soil water storage capacity and its spatial variability are essential landscape properties affecting the water balance at long-term scale. In order to explicitly take the spatially variable soil water storage capacity into account, the functional forms for Equation (4.3) and Equation (4.4) are derived based on the following cumulative distribution function for soil water storage capacity (Wang, 2018):

$$F(C) = 1 - \frac{1}{a} + \frac{C+(1-a)S_b}{a\sqrt{(C+S_b)^2 - 2aS_bC}} \tag{4.5}$$

where C (mm) is soil water storage capacity at a point and $C \geq 0$. Soil water storage capacity in this paper is defined as the maximum pore space in unsaturated zone and shallow aquifer across the catchment, and the value of storage capacity is determined by soil porosity and thickness (Gao et al., 2021). $F(C)$ is the fraction of the catchment area for which the storage capacity is less than or equal to C; S_b (mm) is the average soil water storage capacity over the catchment; a (-) is the shape parameter and has a relation with the initial soil wetting ratio (the relation will be presented in Section 4.2.3.2) in the SCS curve number method (SCS, 1972; Wang 2018) which determines the value of a ranges between 0 and 2, and a smaller value of a means more catchment area with low storage capacity. The conceptual water balance model used here is fundamentally a probability distribution model (PDM) at the mean annual scale, which is referred to as PDM-MA hereinafter. Following the principle of probability distribution model (Liang et al., 1994; Moore, 1985), catchment wetting (mm) can be computed for a given amount of precipitation combined with the spatial distribution of soil water storage capacity; but here the precipitation is the mean annual value:

$$W = \int_0^P [1 - F(C)]dC \tag{4.6}$$

Substituting Equation (4.5) into Equation (4.6), the mean annual catchment wetting at the first stage is computed by the following Equation:

$$W = \frac{P+S_b-\sqrt{(P+S_b)^2-2aS_bP}}{a} \tag{4.7}$$

The spatial variability of actual soil water storage affects evaporation, since the actual evaporation at point scale is the minimum value between the actual storage and potential evapotranspiration. If the catchment is fully saturated, the actual evaporation reaches to its maximum value E_s (mm) which is assumed to be determined by the distribution of storage and mean annual potential evapotranspiration (E_P (mm)) in the catchment (Yao et al., 2020):

$$E_s = \int_0^{E_P} [1 - F(C)]dC \tag{4.8}$$

Replacing $F(C)$ in Equation (4.8) with Equation (4.5), we obtain:

$$E_s = \frac{E_P+S_b-\sqrt{(E_P+S_b)^2-2aS_bE_P}}{a} \tag{4.9}$$

While the catchment is generally not fully saturated, and the corresponding actual evaporation is assumed to be decreased proportionally from E_s relative to the degree of saturation in the catchment:

$$E = \frac{W}{S_b}E_s \tag{4.10}$$

Combining Equation (4.9) and Equation (4.10), the mean annual evaporation at the second stage is calculated by:

$$E = \frac{W}{S_b}\frac{E_P+S_b-\sqrt{(E_P+S_b)^2-2aS_bE_P}}{a} \tag{4.11}$$

Though the method for estimating evaporation (i.e., Equations 4.8-11) was originally proposed for daily water balance model, it has been demonstrated that this method has a good performance in estimating evaporation at longer timescales (Yao et al., 2020).

Substituting Equations (4.7) and (4.11) into Equation (4.4), the Equation for mean annual baseflow is obtained:

$$Q_b = \frac{P+S_b-\sqrt{(P+S_b)^2-2aS_bP}}{a}\left[1-\frac{1+\frac{E_p}{P}\frac{P}{S_b}-\sqrt{\left(1+\frac{E_p}{P}\frac{P}{S_b}\right)^2-2a\frac{E_p}{P}\frac{P}{S_b}}}{a}\right] \tag{4.12}$$

Likewise, the mean annual streamflow is obtained by substituting Equation (4.11) into Equation (4.1):

$$Q = P-\frac{\frac{P}{S_b}+1-\sqrt{(\frac{P}{S_b}+1)^2-2a\frac{P}{S_b}}}{a}\frac{E_p+S_b-\sqrt{\left(E_p+S_b\right)^2-2aS_bE_p}}{a} \tag{4.13}$$

The analytical formulations of Q_b and Q (i.e., Equation (4.12) and Equation (4.13)) based on the spatial distribution of storage capacity combined with the two-stage precipitation partitioning framework can further lead to the formulations of BFI and BFC. While the two-stage precipitation partitioning framework is previously known to be theorized by Ponce & Shetty (1995) using the generalized proportionality relationship originated from the SCS curve number method (SCS, 1972). For the sake of comparison, we also derived Equations for BFI and BFC based on the generalized proportionality relationship.

4.2.3 Baseflow Index

4.2.3.1 Formulation Based on Distribution Function

The expression for BFI based on the spatial distribution function of water storage capacity is obtained after dividing Equation (4.12) by Equation (4.13):

$$BFI = \frac{a-1-\varphi\psi^{-1}+\sqrt{(1+\varphi\psi^{-1})^2-2a\varphi\psi^{-1}}}{A-1-\varphi\psi^{-1}+\sqrt{(1+\varphi\psi^{-1})^2-2a\varphi\psi^{-1}}} \tag{4.14}$$

where $A = \frac{a^2}{1+\psi-\sqrt{(1+\psi)^2-2a\psi}}$ (-) is used for simplifying the Equation; $\varphi = \frac{E_P}{P}$ (-) is the climate aridity index; and $\psi = \frac{S_b}{P}$ (-) is defined as storage capacity index in this paper, which reveals the capability of catchment to hold water supply from precipitation. For example, $\frac{S_b}{P} = 2$ indicates that the average storage capability is twice the precipitation at the mean annual scale. Therefore, BFI is controlled by climate aridity index and soil water storage capacity in terms of $\frac{S_b}{P}$ and the shape parameter (i.e., a). Soil water storage capacity with its spatial variability plays an important role in baseflow through two aspects. First, it affects catchment wetting at the first stage which is the source of water for the second-stage partitioning; subsequently, it influences evaporation at the second stage which competes water with baseflow. Equation (4.14) is plotted in Figures 1a and 1b to show the controls of $\frac{E_P}{P}$, $\frac{S_b}{P}$, and a on BFI. Given $\frac{S_b}{P}$ and a, BFI decreases with $\frac{E_P}{P}$, since evaporation demand is stronger in drier climate leading to a smaller contribution of baseflow to total streamflow. Given $\frac{E_P}{P}$ and a, BFI increases with $\frac{S_b}{P}$ (Figure 4.1a). A larger storage capacity facilitates catchment wetting (i.e., less Q_f) at the first-stage partitioning as suggested by Equation (4.7); as a result, baseflow contributes more to total streamflow (i.e., larger BFI).

As shown in Figure 4.1a, when $\frac{S_b}{P}$ is small (i.e., $\frac{S_b}{P} < 1$), BFI is less sensitive to $\frac{S_b}{P}$ in arid region compared to that in humid region; whereas, when $\frac{S_b}{P}$ is large (i.e., $\frac{S_b}{P} > 1$), BFI is less sensitive to $\frac{S_b}{P}$ in humid region. Taking the curves with $\frac{S_b}{P} = 0.1$ and $\frac{S_b}{P} = 0.5$ for examples, the catchment with a relatively larger storage capacity could store more precipitation. When the climate is humid, the evaporation in both catchments is small due to the limited energy, therefore, the significant difference in catchment wetting from the first-stage partitioning makes BFI much different between catchments. While under arid climate condition, the impact of the large evaporation at the second stage in both catchments overshadows the impact of storage capacity leading to the small difference in BFI between catchments. However, the impact of climate on BFI inverses when $\frac{S_b}{P}$ is large. Taking the curves with $\frac{S_b}{P} = 2.0$ and $\frac{S_b}{P} = 3.0$ for illustration, both catchments have enough capacity to storage precipitation, therefore produce similar amount of fast flow and wetting at the first stage. In a humid climate, the limited energy supply results in small evaporation in both catchments leading to similar baseflow at the second stage. Thus, even a larger storage capacity has a small impact on BFI in a humid climate. While in an arid climate, more catchment wetting could be lost through evaporation in the catchment with a smaller storage capacity. That is because given a soil porosity, the groundwater table is shallower in the catchment with a smaller storage capacity, leading to a larger evaporation from storage. Correspondingly, BFI is much smaller in the catchment with a smaller storage capacity index.

The shape parameter affects BFI in a more complex way as shown in Figure 4.1b. A large value of a promotes catchment wetting (i.e., less Q_f) at the first-stage partitioning indicated by Equation (4.7) since a larger shape parameter means that the distribution of storage capacity is less left skewed (Wang, 2018). Similarly, a larger value of a causes a larger E_s for a given E_P at the second-stage partitioning based on Equation (4.9). Given a value of $\frac{E_P}{P}$, the catchment with a larger a produces more catchment wetting at the first stage. When the climate is more humid, more wetting is partitioned into baseflow because of the limited energy supply for evaporation, resulting in a larger contribution of baseflow to the total streamflow (i.e., larger BFI). However, when the climate is arid, even though the catchment with a larger shape parameter has more wetting from the first stage, the larger shape parameter causes larger evaporation at the second-stage partitioning since soil water is limited compared with evaporation demand, leading to a smaller contribution of baseflow to the total streamflow (i.e., smaller BFI). As shown in Figure 4.1b, the $\frac{E_P}{P}$ at the transition point of the effects of shape parameter increases with $\frac{S_b}{P}$, due to the reason that a larger storage capacity could attenuate the impact of evaporation on the partitioning of wetting at the second stage. $\frac{S_b}{P}$ and a affect the values of BFI when $\frac{E_P}{P}$ approaches 0 as shown in Figure 4.1a and Figure 4.1b. For a given a, the maximum value of BFI increases with $\frac{S_b}{P}$ since a larger storage capacity facilitates baseflow generation. The maximum value of BFI is smaller than 1, and it approaches 1 when $\frac{S_b}{P} \geq 1$ and $a \rightarrow 2$.

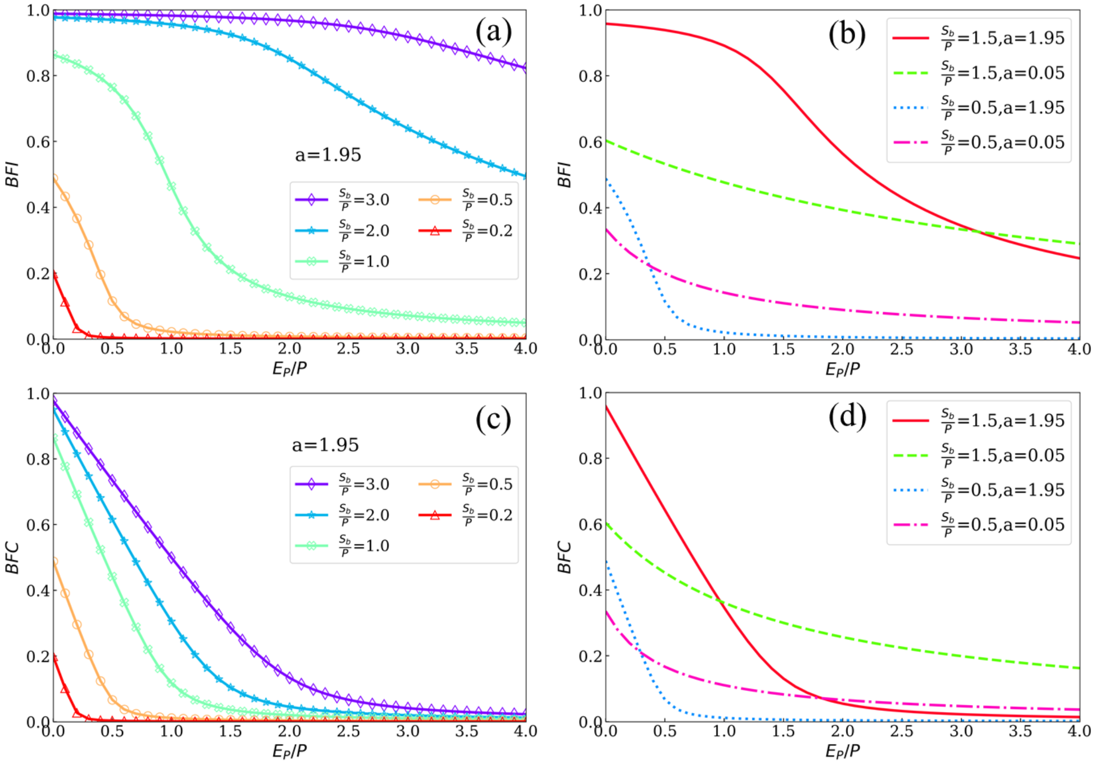

Figure 4.1: The controls of climate aridity index $\left(\frac{E_P}{P}\right)$ and storage capacity index $\left(\frac{S_b}{P}\right)$ on (a) baseflow index (BFI) based on Equation (4.14) and (c) baseflow coefficient (BFC) based on Equation (4.18) for a given shape parameter, (i.e., $a = 1.95$); the controls of shape parameter (i.e., a) on (b) BFI and (d) BFC for given $\frac{S_b}{P}$ (i.e., $\frac{S_b}{P} = 1.5$ and 0.5).

4.2.3.2 Formulation Based on Generalized Proportionality

In the Ponce & Shetty formulations, W reaches an upper limit, i.e., catchment wetting potential (W_P (mm)), when P and Q_f grow unlimited (Ponce & Shetty, 1995; Sivapalan et al., 2011). The catchment wetting potential can be considered analogous to soil water storage capacity (Gnann et al., 2019). Here, we define a dimensionless number, $\zeta = \frac{W_P}{P}$ (-), for the generalized proportionality relationship, and ζ is analogous to $\frac{S_b}{P}$. Correspondingly, the equation of BFI based on the generalized proportionality relationship is obtained as follows:

$$BFI = \begin{cases} \frac{B}{(1-\zeta\lambda_p)^2\left\{[1-\eta(2\lambda_W-1)][1-\zeta(2\lambda_p-1)]-(1-\zeta\lambda_p)^2\right\}+B}, & P > \lambda_P W_P \text{ and } W > \lambda_W V_P \\ 0, & P > \lambda_P W_P \text{ and } W \leq \lambda_W V_P \\ 1, & P \leq \lambda_P W_P \text{ and } W > \lambda_W V_P \\ \text{does not exist,} & P \leq \lambda_P W_P \text{ and } W \leq \lambda_W V_P \end{cases} \quad (4.15)$$

where $B = \left\{(1-\eta\lambda_w)[1-\zeta(2\lambda_p-1)] - (1-\zeta\lambda_p)^2\right\}^2$; $\eta = \frac{V_P}{P}$ (-) quantifies the climate dryness condition and is analogous to $\frac{E_P}{P}$; V_P (mm) is the vaporization potential, indicting the limit of energy (Gnann et al., 2019); λ_P (-) and λ_w (-) are the initial abstraction coefficients for fast flow and baseflow generations, respectively. In the case of $P > \lambda_P W_P$ and $W > \lambda_W V_P$, given certain values of λ_P and λ_w (e.g., λ_P =0.05, λ_W =0.02, the median values in Gnann et al. (2019)), the controls of $\frac{V_P}{P}$ and $\frac{W_P}{P}$ on BFI, shown in Figure 4.2a, are generally consistent with the findings based on Equation (4.14) shown in Figure 4.1a. That is, BFI increases with $\frac{W_P}{P}$ for a given $\frac{V_P}{P}$, and BFI decreases with $\frac{V_P}{P}$ for a given $\frac{W_P}{P}$. The agreement between Equation (4.14) and Equation (4.15) is expected since the cumulative distribution function in Equation (4.5) also leads to a proportionality relationship (Wang, 2018).

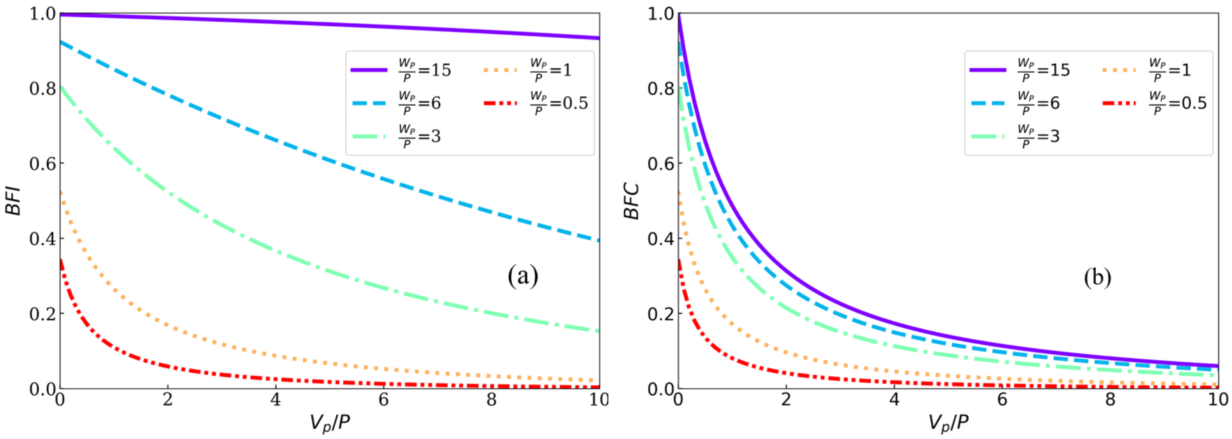

Figure 4.2: The controls of $\frac{V_P}{P}$ and $\frac{W_P}{P}$ on (a) baseflow index (BFI) based on Equation (4.15) and (b) baseflow coefficient (BFC) based on Equation (4.19), with fixed values of λ_P (=0.05) and λ_W (=0.02) which are the median values in Gnann et al. (2019).

However, the parameterizations for the initial abstraction terms between these two proportionality relationships are different. Equation (4.15) was developed based on the generalized proportionality relationship of the SCS curve number method (SCS, 1972), in which the partitioning of P into W and Q_f is quantified by:

$$\frac{W-\lambda_P W_P}{W_P-\lambda_P W_P}=\frac{Q_f}{P-\lambda_P W_P} \tag{4.16}$$

where $P \geq \lambda_P W_P$. If $P < \lambda_P W_P$, $Q_f = 0$ and $W = P$. Catchment wetting in Equation (4.7) can be obtained from the following proportionality relationship:

$$\frac{W-\varepsilon W}{S_b-\varepsilon W}=\frac{Q_f}{P-\varepsilon W} \tag{4.17}$$

where εW can be interpreted as "initial abstraction"; and ε is the initial catchment wetting ratio, which has a relationship with the shape parameter, i.e., $a = 2\varepsilon(2-\varepsilon)$. Readers are referred to (Wang, 2018) for the detailed derivation of Equation (4.17). The initial abstraction for fast flow in Equation (4.16) is proportional to catchment wetting potential. However, the initial abstraction term in Equation (4.17) is proportional to actual wetting instead of wetting potential. Equation (4.17) is more reasonable than Equation (4.16) considering the boundary condition of Budyko-type equation (Wang, 2018), and the parameterization for initial abstraction in Equation (4.17) allows a single formula (Equation (4.14)) instead of a piecewise function of BFI in Equation (4.15). Moreover, the basis for the generalized proportionality relationship (Equation (4.16)), i.e., the SCS curve number method, is empirical (Ponce & Shetty, 1995), and studies found it is difficult to quantitatively link the parameters in the generalized proportionality relationship to the catchment and climatic properties (Gnann et al., 2019; Sivapalan et al., 2011; Tang & Wang, 2017); whereas, the basis for the proportionality relationship in Equation (4.17) is the cumulative distribution function (Equation (4.5)) which quantifies the spatial variability of soil water storage capacity and can be linked to the landscape characteristics in a straightforward way.

4.2.4 Baseflow Coefficient

4.2.4.1 Formulation Based on Distribution Function

We can have the formulation for BFC, which is based on the distribution function of water storage capacity, through dividing Equation (4.12) by P on both hand sides:

$$BFC = \frac{1+\psi-\sqrt{(1+\psi)^2-2a\psi}}{a}\left[1-\frac{1+\varphi\psi^{-1}-\sqrt{(1+\varphi\psi^{-1})^2-2a\varphi\psi^{-1}}}{a}\right] \tag{4.18}$$

Figures 4.1c and 4.1d show the control of $\frac{E_P}{P}$, $\frac{S_b}{P}$, and a on BFC. Similar to BFI, for given $\frac{S_b}{P}$ and a, BFC decreases with $\frac{E_P}{P}$ as shown in Figure 4.1c because more precipitation leaves catchments through evaporation rather than baseflow. Given $\frac{E_P}{P}$ and a, BFC increases as $\frac{S_b}{P}$ since a larger storage capacity could store more precipitation, i.e., a larger W, which promotes the generation of baseflow at the second stage. However, BFC is not sensitive to $\frac{S_b}{P}$ in arid climate no matter the magnitude of $\frac{S_b}{P}$, and this is different from the impact of $\frac{S_b}{P}$ on BFI. Precipitation is mainly partitioned into evaporation in arid climate, and the difference in baseflow caused by different storage capacities is diluted since baseflow is relatively small compared with precipitation.

The impact of a on BFC is dependent on $\frac{E_P}{P}$ as shown in Figure 4.1d. BFC is positively related to a in a relatively humid condition; whereas it is negatively related to a in an arid condition. In humid region, a mainly plays a role at the first-stage partitioning, and catchment wetting increases with a; whereas, in arid region, a mainly plays a role at the second-stage partitioning, and evaporation increases with a.

The maximum value of BFC when $\frac{E_P}{P}$ approaches 0 is affected by $\frac{S_b}{P}$ and a similar to BFI. That is, the maximum value of BFC is positively related to $\frac{S_b}{P}$ and a, since both catchment wetting and baseflow increases with $\frac{S_b}{P}$ and a in a very humid condition.

4.2.4.2 Formulation Based on Generalized Proportionality

By replacing Equation (4.12) with the baseflow equation in the Ponce & Shetty formulations (Ponce & Shetty, 1995), and normalizing it by precipitation, the formula of BFC based on the generalized proportionality relationship can be obtained:

$$BFC = \begin{cases} \frac{B}{[1-\zeta(2\lambda_p-1)]\left\{[1-\eta(2\lambda_W-1)][1-\zeta(2\lambda_p-1)]-(1-\zeta\lambda_p)^2\right\}}, & P > \lambda_P W_P \text{ and } W > \lambda_W V_P \\ 0, & P > \lambda_P W_P \text{ and } W \leq \lambda_W V_P \\ \frac{(1-\eta\lambda_W)^2}{1+\eta(1-2\lambda_W)}, & P \leq \lambda_P W_P \text{ and } W > \lambda_W V_P \\ 0, & P \leq \lambda_P W_P \text{ and } W \leq \lambda_W V_P \end{cases} \quad (4.19)$$

Figure 4.2b shows the controls of $\frac{V_P}{P}$ and $\frac{W_P}{P}$ on BFC in the case of $P > \lambda_P W_P$ and $W > \lambda_W V_P$ given the same values of λ_P (=0.05) and λ_W (=0.02) as those in Figure 4.2a, and it displays a highly similar pattern of BFC as a function of $\frac{E_P}{P}$ and $\frac{S_b}{P}$ (Figure 4.1c). The similarity between Figure 4.2b and Figure 4.1c further demonstrates the capability of the proposed mathematical analysis for the two-stage partitioning of precipitation.

Considering the solid mathematical and physical basis and the concise functional forms, Equation (4.14) and Equation (4.18), which are on the basis of spatial distribution of soil water storage capacity, are used for analyzing the control of mean annual climate and landscape on mean annual baseflow in this paper.

4.2.5 Impacts of Climate Variability on Mean Annual Baseflow

Existing studies have revealed that variability in climate forcings, including the intra-monthly, intra-annual, and inter-annual variability, has large impacts on mean annual streamflow (Berghuijs et al., 2014; Li, 2014; Potter et al., 2005; Reggiani et al., 2000; Shao et al., 2012). However, few studies have quantified the impacts of climate variability on mean annual baseflow using probability distribution model. The roles of finer time scale climate forcings on BFI and BFC were analyzed in this paper to further quantify the added error on BFI and BFC estimates due to aggregation of forcings.

Following Yao et al. (2020), the quantification was conducted based on numerical simulations driven by climate inputs at the daily time step. Due to the timescale effect of parameters (Deng et al., 2018), the values of S_b and a at the mean annual scale cannot be applied to the model with daily time step. Therefore, the two-stage precipitation partitioning model at the mean annual scale was modified to the daily scale which is referred to as PDM-D since it is a probability distribution model at the daily scale. At the daily time step, antecedent soil water storage (S_0 (mm)) should be taken into account since water balance is unsteady. The total storage after daily precipitation ($W + S_0$) is partitioned into evaporation (E), baseflow (Q_b), and ending storage (S_1 (mm)) at the second partitioning stage:

$$W + S_0 = E + Q_b + S_1 \tag{4.20}$$

Based on the principle of the PDM, daily catchment wetting could be obtained by the following integration (Liang et al., 1994; Moore, 1985):

$$W = \int_{C_0}^{P+C_0} [1 - F(C)]dC \tag{4.21}$$

where C_0 (mm) is the point-scale initial storage in the unsaturated area within the catchment. Substituting Equation (4.5) into Equation (4.21), catchment wetting at the daily scale can be expressed as:

$$W = \frac{P+S_b\sqrt{(m+1)^2-2am}-\sqrt{[P+(m+1)S_b]^2-2amS_b{}^2-2aS_bP}}{a} \tag{4.22}$$

where $m = \frac{S_0(2S_b-aS_0)}{2S_b(S_b-S_0)}$. Daily fast flow is the remaining part of precipitation after soil wetting:

$$Q_f = P - W \tag{4.23}$$

The value of daily catchment E is determined by the equation similar to Equation (4.11) but with S_0:

$$E = \frac{W+S_0}{S_b}\frac{E_P+S_b-\sqrt{(E_P+S_b)^2-2aS_bE_P}}{a} \tag{4.24}$$

Daily baseflow is assumed to have a linear relationship with the net storage (Fenicia et al., 2006):

$$Q_b = k(W + S_0 - E) \tag{4.25}$$

where k (-) is the baseflow discharge coefficient between 0 and 1. Substituting Equation (4.21) into Equation (4.22), Q_b is modeled as follows:

$$Q_b = k(W + S_0)\left[1 - \frac{E_P+S_b-\sqrt{(E_P+S_b)^2-2aS_bE_P}}{aS_b}\right] \tag{4.26}$$

Correspondingly, the storage at the end of each day is obtained by:

$$S_1 = (1-k)(W + S_0)\left[1 - \frac{E_P+S_b-\sqrt{(E_P+S_b)^2-2aS_bE_P}}{aS_b}\right] \tag{4.27}$$

Mean annual streamflow, including fast flow and baseflow, is aggregated from the daily values. Since mean annual streamflow is of interest here, streamflow routing is not necessary in this model.

To analyze the impacts of climate variability, four sets of BFI and BFC were obtained and compared for each catchment driven by four climate inputs, i.e., observed climate (i.e., daily climate), climate forcings without intra-monthly variability (i.e., monthly climate), climate forcings without intra-annual variability (i.e., annual climate), and climate forcings without inter-annual variability (i.e., mean annual climate), respectively. Readers are referred to Yao et al., (2020) for the detailed descriptions of climate inputs incorporating variability at different time scales.

4.2.6 Study Catchments and Data

The controls of climate and soil water storage capacity on baseflow index and baseflow coefficient are evaluated for 311 catchments from U.S. Model Parameter Estimation Experiment (MOPEX) (Duan et al., 2006), and 131 catchments from U.K. Benchmark Network (UKBN2; Harrigan et al., 2018) covering a wide range of prevailing climate. These catchments are well suited for quantifying the climate and landscape controls on long-term baseflow since the human interferences in these catchments are relatively small.

The selected catchments have drainage areas larger than 10 km^2, and have data records of daily precipitation, potential evapotranspiration, and streamflow for at least 10 water years (from 1 October through 30 September), and the percentage of missing streamflow data within each water year is less than 5%. For the U.S. catchments, the precipitation and streamflow data were obtained from the MOPEX dataset, and the daily reference evapotranspiration data, which were estimated by the Penman-Monteith equation, were extracted from a gridded surface meteorological dataset (gridMET) with a spatial resolution of ~4 km (Abatzoglou, 2013). The monthly potential evapotranspiration provided by the University of Montana (Zhang et al., 2010) was used to scale the reference evapotranspiration. For the UKBN2 catchments, the daily precipitation and streamflow data were obtained from the National River Flow Archive (NRFA), and the daily potential evapotranspiration data based on the Penman-Monteith method were extracted from CHESS-PE (Robinson et al., 2020). The snow fall fraction of precipitation of MOPEX catchments was estimated from the empirical precipitation phase probability function proposed by Dai (2008), and the snow fall fraction of precipitation of UKBN2 catchments was available in the UKBN2 dataset. To minimize the effect of snow on the long-term water balance partitioning, we considered the fraction of precipitation falling as snow in the selected catchments is less than 20% (Gnann et al., 2019). The baseflow for the study catchments was estimated through baseflow separation using the recursive digital filter method with forward, backward, and forward steps with a filter parameter of 0.925 (Lyne & Hollick, 1979). It has been demonstrated that the baseflow estimation through different methods agree well for catchments in the study area (Gnann et al., 2019).

All the hydroclimatic data were aggregated to their mean annual values for further analysis in the PDM-MA model, and the spatial distribution of mean annual precipitation, potential evapotranspiration, total streamflow, and baseflow for the two regions are displayed in Figure S4.1 in the Supporting Information (SI). The median values of mean annual precipitation, potential evapotranspiration, total streamflow, and baseflow for the MOPEX (UKBN2) catchments are 1010 (1104) mm, 1104 (496) mm, 359 (732) mm, and 149 (292) mm, respectively. Precipitation in these two regions is similar, but the potential evapotranspiration in the MOPEX catchments is relatively larger, indicating that the average climate in U.S. catchments is more arid than that in U.K. catchments, which is demonstrated by the spatial distribution of climate aridity index as shown in Figure S4.2. As a result, the median values of mean annual streamflow and baseflow in the U.S. catchments are much less than those in the U.K. catchments.

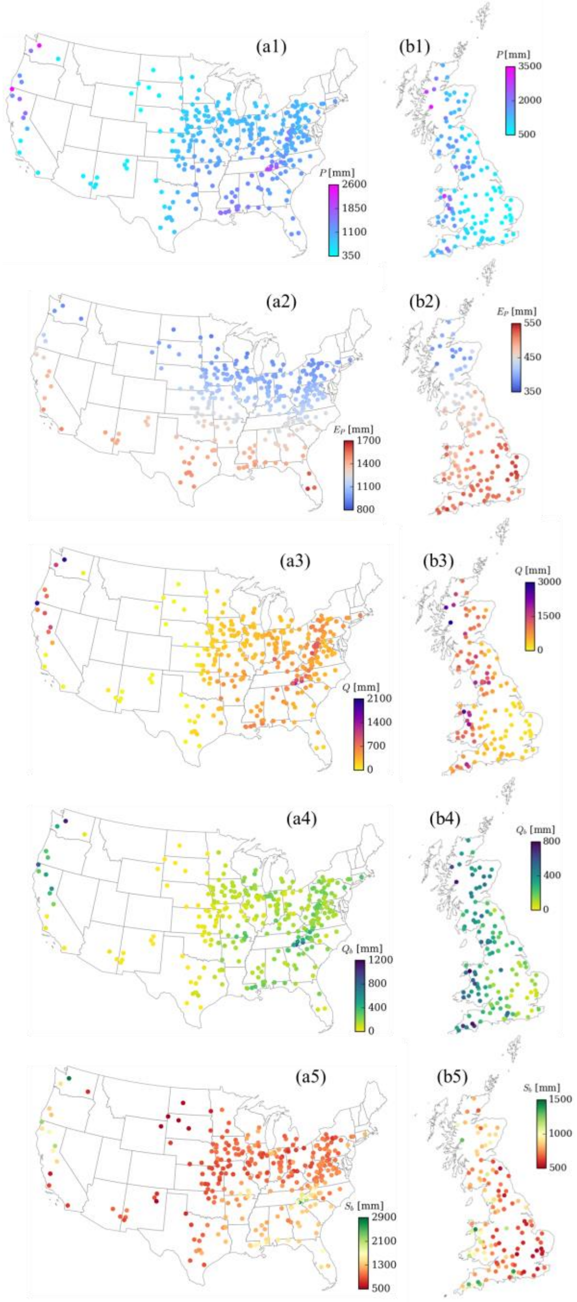

Figure S4.1: The spatial distribution of mean annual precipitation (P), potential evapotranspiration (E_P), streamflow (Q), baseflow (Q_b), and soil water storage capacity (S_b) in (a1-a5) the MOPEX catchments and (b1-b5) the UKBN2 catchments.

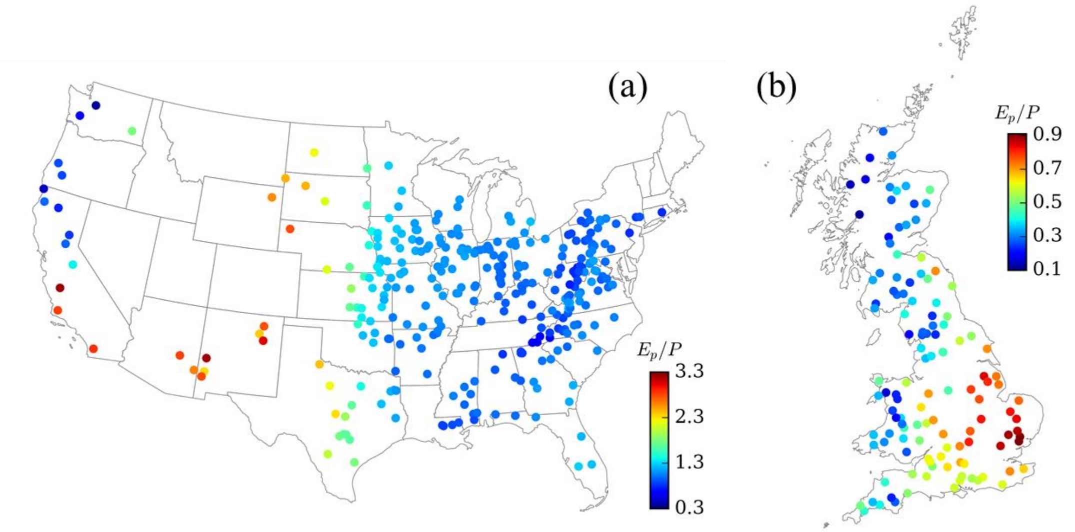

Figure S4.2: The climate aridity index $\left(\frac{E_P}{P}\right)$ in (a) the MOPEX catchments and (b) the UKBN2 catchments.

4.2.7 Parameter Estimation

4.2.7.1 PDM-MA Model

It is a challenge to directly measure the soil water storage capacity and its spatial variability in catchments or analytically solve S_b and a from Equation (4.12) and Equation (4.13). In this study, the values of S_b and a for each catchment were solved numerically based on Equation (4.12) and Equation (4.13) using the nonlinear least-squares method. Q and Q_b in these two equations are the mean annual streamflow and the mean annual baseflow, respectively, and the latter was obtained through the recursive digital filter method as described in Section 4.2.6. The range of a is from 0 to 2 (Wang, 2018), and the range of S_b is from 0 to 50000 mm (Gnann et al., 2019). The large upper limit used for S_b guarantees that the solution is not subject to the range of the parameter. The objective function is to minimize the relative error between the observed Q_b and the modeled one from Equation (4.12), and the relative error between the observed Q and its modeled counterpart from Equation (4.13). S_b and a are determined at the mean annual scale in this study instead of inter-annual scale in order to eliminate the potential influence of carryover storage between years.

4.2.7.2 PDM-D Model

There are 3 parameters (i.e., S_b, a, and k) in the daily water balance model. The range of S_b is between 50 mm and 1500 mm (Kollat et al., 2012); a is between 0 and 2 (Wang, 2018); and k ranges from 0 to 1. The parameters were estimated through calibration using the Shuffled Complex Evolution Method (SCE-UA) in the SPOTPY python package (Duan et al., 1992; Houska et al., 2015). The objective function is to minimize the sum of two relative errors: the relative error between the simulated mean annual streamflow (Q_{sim}) and its observed value (Q_{obs}), and the relative error between the simulated mean annual baseflow ($Q_{b,sim}$) and its observed value ($Q_{b,obs}$), and these mean annual values were aggregated from the daily values:

$$OBJ = \frac{|Q_{sim} - Q_{obs}|}{Q_{obs}} + \frac{|Q_{b,sim} - Q_{b,obs}|}{Q_{b,obs}} \tag{4.28}$$

The data used for daily model are required to be continuous; therefore, the length of the data used for the daily model for parameter estimation is shorter than that for the mean annual water balance in some study catchments, but the minimum length of data records is 10 years. The available data was divided into three periods: warm-up, calibration, and validation. The first two years were used for model warm-up to eliminate the impact of uncertain initial condition (Kim et al., 2018). If the number of remaining years of data (N) is an even number, one half of the remaining data were used for calibration and the other half was used for model validation. While if N is an odd number, data of (N+1)/2 years were used for calibration and the remaining data were used for validation.

4.3 Results and Discussion

4.3.1 Estimated Parameters

4.3.1.1 PDM-MA Model

The estimated parameters (i.e., S_b and a) for the PDM-MA model have a good performance in modelling the mean annual Q and Q_b (Figure 4.3). Almost all the pairs of data fall on the 1:1 line, while there are 7 catchments with the relative error between the modeled value and the observation of Q higher than 10% due to the uncertainty of the data or the limitation of the parsimonious mean annual baseflow model. These 7 catchments were removed from further analysis. Both the Q and Q_b of the remaining catchments have the relative error smaller than 0.2% on average.

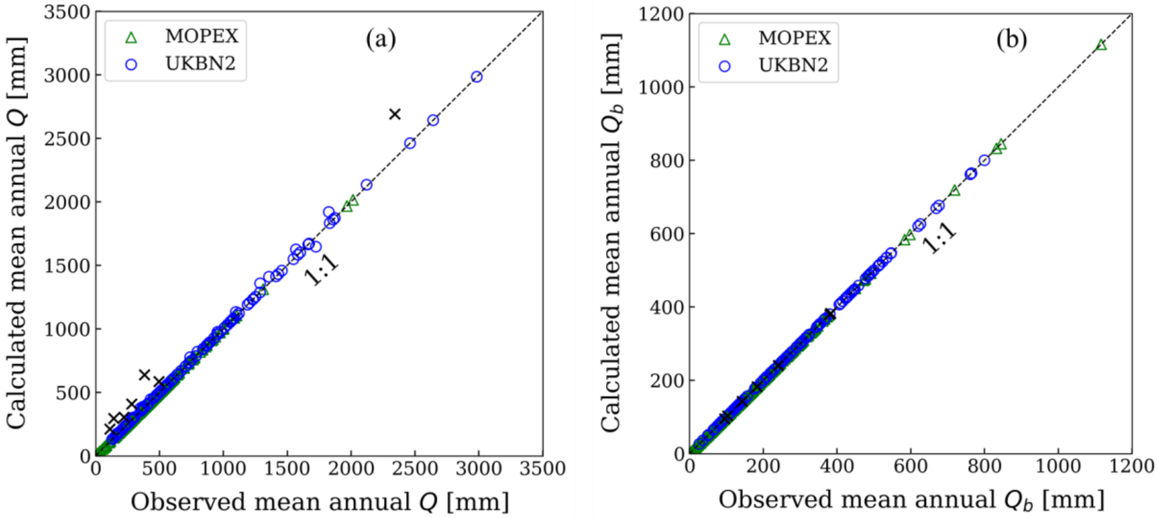

Figure 4.3: The performance of the estimated average soil water storage capacity (S_b) and the shape parameter (a) in modeling (a) the mean annual total streamflow (Q), and (b) the mean annual baseflow (Q_b) in the PDM-MA model. Cross denotes catchments with the relative error between the modeled Q and the observed Q higher than 10%.

The estimated S_b displays a significant spatial variability among the study catchments. It ranges from 478 (502) mm to 2829 (1436) mm with median value of 1037 (769) mm in the U.S. (U.K.) catchments (Figure S4.1-a5 and S4.1-b5). Considering that both BFI and BFC are directly related to the ratio of S_b and P, storage capacity, i.e., $\frac{S_b}{P}$, is shown in Figure 4.4 and discussed in detail. Comparing the spatial distribution of $\frac{S_b}{P}$ with that of $\frac{E_P}{P}$ in Figures S4.2 in SI, one can find that the catchment with a larger $\frac{E_P}{P}$ generally has a larger $\frac{S_b}{P}$ among the selected catchments in both study regions, such as those in the southwestern U.S. and the southeastern U.K. The $\frac{S_b}{P}$ in the UKBN2 catchments are generally smaller than those in the MOPEX catchments, similarly for $\frac{E_P}{P}$. Moreover, the relationship between $\frac{S_b}{P}$ and $\frac{E_P}{P}$ follows a logarithmic function as shown in Figure 4.4c. Storage capacity is one of the emergent properties of a catchment and serves as a buffer for vegetation to cope with water stress. Therefore, vegetation in catchments with drier climate is more likely to develop a stronger root system to store more water during wet seasons and access to the deeper groundwater for compensating the water shortage during dry seasons leading to a larger storage capacity (de Boer-Euser et al., 2016; Gao et al., 2014; Troch et al., 2009). Whereas, when the climate becomes even drier, the optimal strategy of vegetation for dealing with water stress turns to rapid growth instead of extending their root zone system (Gentine et al., 2012). As a result, $\frac{S_b}{P}$ increases rapidly with $\frac{E_P}{P}$ but potentially levels off when $\frac{E_P}{P}$ is large as presented in Figure 4.4c.

The spatial distributions of the estimated shape parameter (a) across the continental U.S. and U.K. can be seen in Figures 4.5a and 4.5b, respectively. All the smaller values of a are in catchments with humid climate such as those in the northwestern U.S., the northeastern U.S., and the middle of U.K. This phenomenon could be explained as a result of catchment coevolution that the functional features of catchment adapt over time to the nature of climate forcing through ecological, pedological, and geomorphological processes (Blöschl et al., 2013; Troch et al., 2015). Specifically, the ample precipitation in humid climate forces the catchment to behave in a way that can quickly discharge the incoming water by allowing more water to be partitioned into fast flow, and thus lead to a smaller value of a. Figure 4.5c shows the frequency distribution of the estimated shape parameter in the study catchments. Most of the estimated a are close to its upper bound (i.e., 2), suggesting that the spatial variability of soil water storage capacity within catchment is not much different in most of the study catchments. The median value of the estimated a is 1.90, indicating an "S" shape for the cumulative distribution function of soil water storage capacity (Wang, 2018). This result is in agreement with Sivapalan et al. (1997) which also showed "S" shapes for the soil water storage capacity based on topographic wetness index in catchments from different regions around the world.

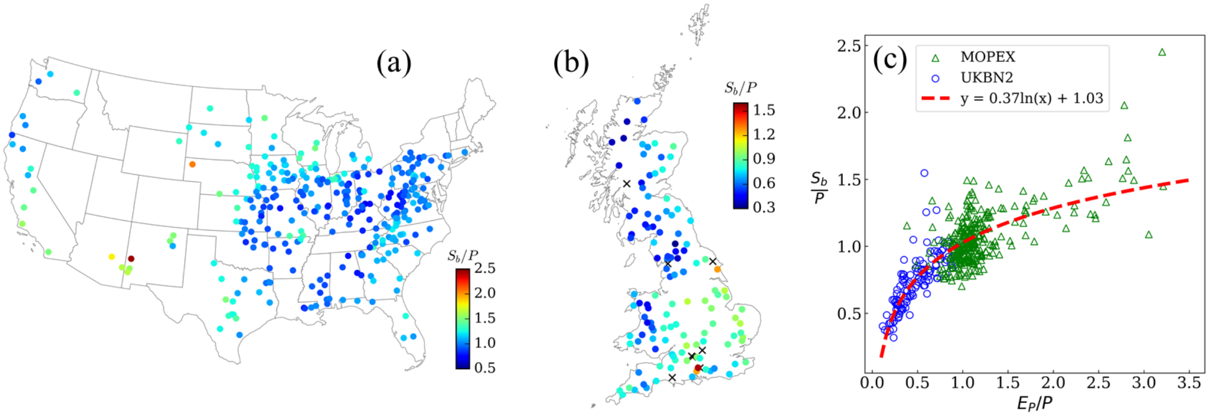

Figure 4.4: The spatial distribution of storage capacity index $\left(\frac{S_b}{P}\right)$ in (a) the MOPEX catchments and (b) the UKBN2 catchments; (c) the relationship between $\frac{S_b}{P}$ and climate aridity index $\left(\frac{E_P}{P}\right)$. Cross denotes catchments with the relative error between the modeled Q and the observed Q higher than 10%.

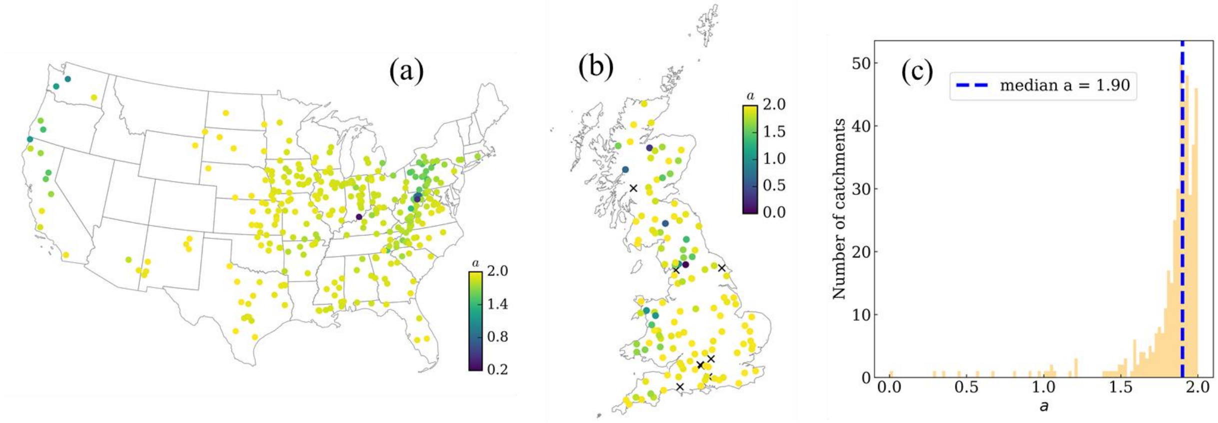

Figure 4.5: The spatial distribution of the shape parameter (i.e., a) in (a) the MOPEX catchments and (b) the UKBN2 catchments; (c) the frequency distribution of a. Cross denotes catchments with the relative error between the modeled Q and the observed Q higher than 10%.

4.3.1.2 PDM-D Model

The median values of the estimated S_b, a, and k are 239.5 mm, 1.989, and 0.0026, respectively, for all the study catchments in the daily water balance model. The modelled mean annual Q and Q_b in both calibration and validation periods were compared with their observed counterparts (Figure S4.3 in SI). A simple linear regression model was fitted between the modelled and observed values. During the calibration (validation) period, the slope of the linear regression and the coefficient of determination (R^2) were 1.01 (1.02) and 0.98 (0.96) for mean annual Q, and 0.99 (0.89) and 0.99 (0.91) for mean annual Q_b. In the daily model, small biases for mean annual baseflow and total streamflow (or fast flow) are not achieved simultaneously for some catchments, due to the uncertainty of the daily baseflow estimated from the separation method. However, the model performance is satisfactory for serving the purpose of investigating the role of climate variability on baseflow.

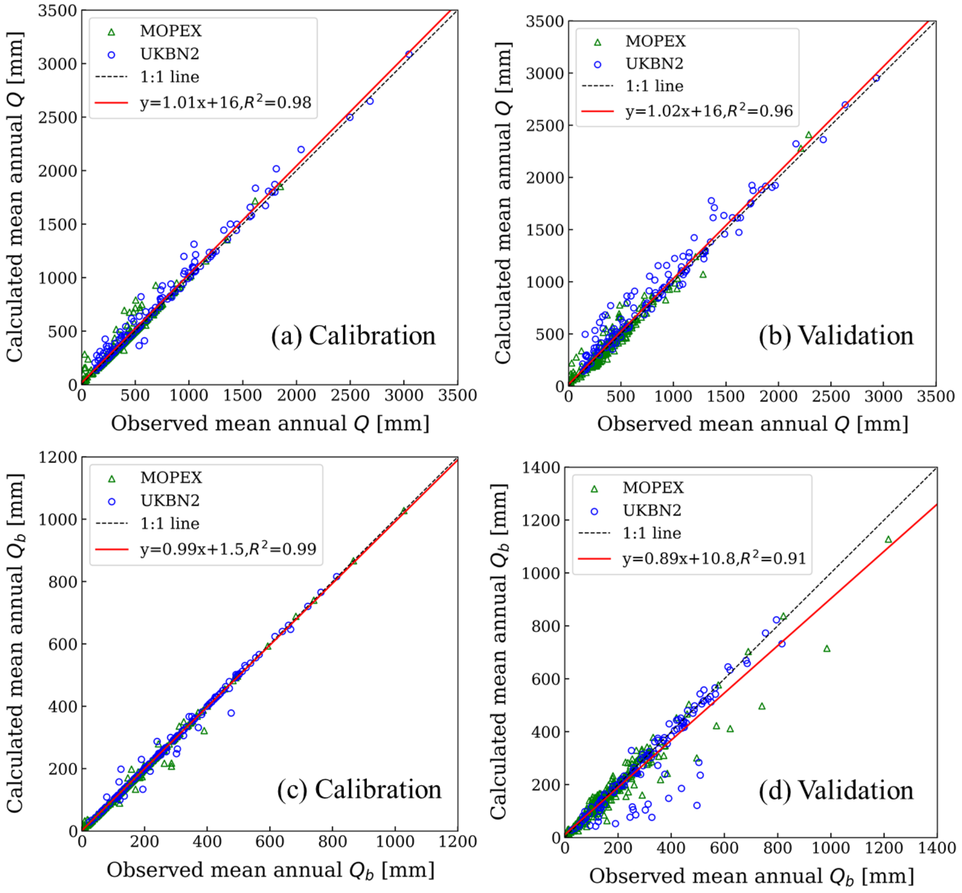

Figure S4.3: The performance of the daily water balance model in modeling the mean annual total streamflow (Q) during (a) the calibration and (b) the validation periods; the performance of the daily water balance model in modeling the mean annual baseflow (Q_b) during (c) the calibration and (d) the validation periods.

4.3.2 Baseflow Index

The observed BFI for all the study catchments is shown in Figure 4.6a as a function of $\frac{E_P}{P}$ and $\frac{S_b}{P}$ (represented by colors). The strong mediating effect of soil storage capacity causes the scattering of observations in the figure. However, since most of the study catchments have a similar shape parameter close to the upper bound, the observed baseflow indexes still present a systematic pattern when the storage capacity is considered. The dashed curves are plotted based on the theoretical values calculated by Equation (4.14) for $\frac{S_b}{P}$ =1.5, 1.1, 0.9, 0.6 and 0.4, and a=1.90

which is the median of the estimated values from all the study catchments. Note that these dashed curves serve as a reference for explaining the distribution of the observed points instead of trying to fit against the observations since different points in this figure have different values of a and $\frac{S_b}{P}$. Obviously, the group of catchments with similar values of a and $\frac{S_b}{P}$ is around the same theoretical curve of Equation (4.14). Generally, drier climate is associated with smaller BFI while the impact of climate is mediated by soil water storage capacity. Consistent with the theoretical curves, larger $\frac{S_b}{P}$ is associated with higher BFI when the catchments have a similar climate aridity index. Figures 4.6b and 4.6c present the BFI for the MOPEX and UKBN2 catchments, respectively. Surprisingly, the controls of $\frac{E_P}{P}$ and $\frac{S_b}{P}$ on BFI are consistent in the contiguous U.S. and U.K. catchments which have remarkably different mean annual climates.

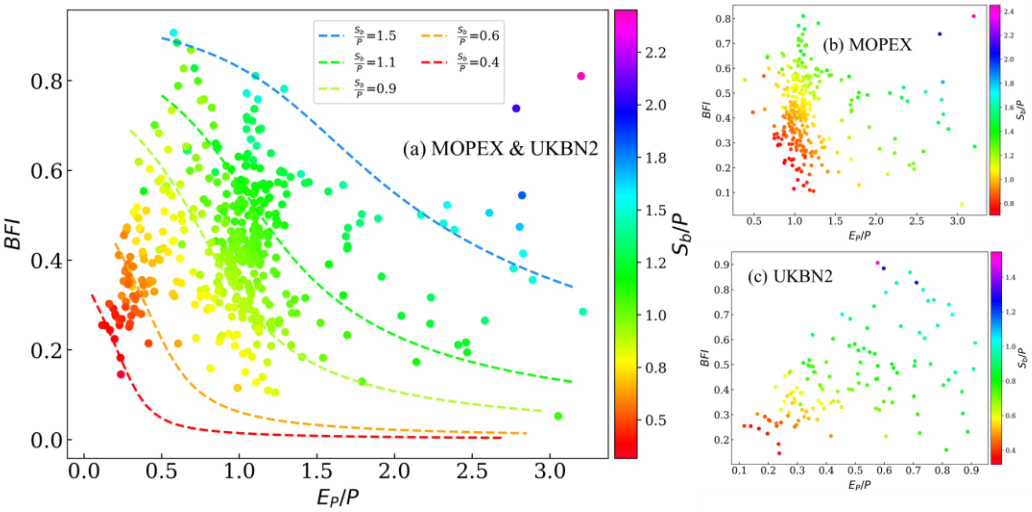

Figure 4.6: The controls of climate aridity index $\left(\frac{E_P}{P}\right)$ and storage capacity index $\left(\frac{S_b}{P}\right)$ on baseflow index (BFI) in the MOPEX and the UKBN2 catchments. The curves are obtained based on Equation (4.14) with $\frac{S_b}{P}$ =1.5, 1.1, 0.9, 0.6 and 0.4, and a=1.90 which is the median of the estimated values from all the study catchments.

4.3.3 Baseflow Coefficient

The observed BFC versus $\frac{E_P}{P}$ colored according to their $\frac{S_b}{P}$ values for all the study catchments is presented in Figure 4.7a. The reference curves are plotted based on the theoretical values calculated by Equation (4.18) with the same parameters used for those in Figure 4.6a. Similar to BFI, the observed BFC generally decreases with $\frac{E_P}{P}$ but mediated by $\frac{S_b}{P}$. BFC increases significantly with $\frac{S_b}{P}$ in humid climate, while it converges to a narrow domain when the climate is dry due to the prevalence of evaporation at the second-stage partitioning. Figures 4.7b and 4.7c display the observed BFC for the MOPEX and UKBN2 catchments, respectively. The climate aridity index in the MOPEX catchments spreads in a wide range from around 0.5 to larger than 3.0, and the BFC approximately presents a monotonical decreasing trend with $\frac{E_P}{P}$. While in the UKBN2 catchments if $\frac{S_b}{P}$ is not considered, BFC seems to increase with $\frac{E_P}{P}$ when the climate is very humid ($\frac{E_P}{P} < 0.5$) but decrease with $\frac{E_P}{P}$ when $\frac{E_P}{P}$ is larger (Figure 4.7c). However, if we group the UKBN2 catchments into different clusters based on the value of $\frac{S_b}{P}$, BFC in each cluster presents a decreasing trend with $\frac{E_P}{P}$ as well. This result underlines the importance of considering $\frac{S_b}{P}$ when analyzing the relationship between BFC and $\frac{E_P}{P}$.

The comparison between Figure 4.6a and Figure 4.7a suggests that storage capacity index has less impact on BFC than on BFI, and the observed BFC is more clustered in a smaller domain in the plot especially for the MOPEX catchments. This prompts researchers to ask the question whether there is a baseflow Budyko curve which captures the observations of BFI as a function of $\frac{E_P}{P}$ similar as the relationship between mean annual evaporation ratio ($\frac{E}{P}$) and $\frac{E_P}{P}$ in the Budyko framework (Budyko, 1974). Meira Neto et al. (2020) have successfully developed a deterministic curve for capturing the BFC of 378 catchments in the contiguous U.S. Figure 4.8 shows that their equation is in good agreement with the observations from the MOPEX catchments as well, confirming the predominant control of mean annual climate on BFC in the U.S. The relationship between BFC and $\frac{E_P}{P}$ in the MOPEX catchments can also be well approximated by a single curve from Equation (4.18) with the median values of $\frac{S_b}{P}$ and a for the MOPEX catchments (i.e., $\frac{S_b}{P}$ = 1.03 and a = 1.88) as shown in Figure 4.8. For this curve, when $\frac{E_P}{P} = 0,$ BFC = 0.8 instead of 1 (Wang & Wu, 2013), meaning that there is always some precipitation partitioned into fast flow even in very humid catchments, and this is in line with Meira Neto et al. (2020). However, the deterministic formulation obtained from the catchments in the contiguous U.S. is no longer applicable to the catchments in the U.K. where $\frac{E_P}{P}$ is much smaller as pointed by Gnann et al. (2019). It can be inferred that BFC decreases with increasing $\frac{E_P}{P}$, but the role of storage capacity on mean annual baseflow is significant in very humid catchments, leading to the high variability of observed BFC among the catchments in the U.K.

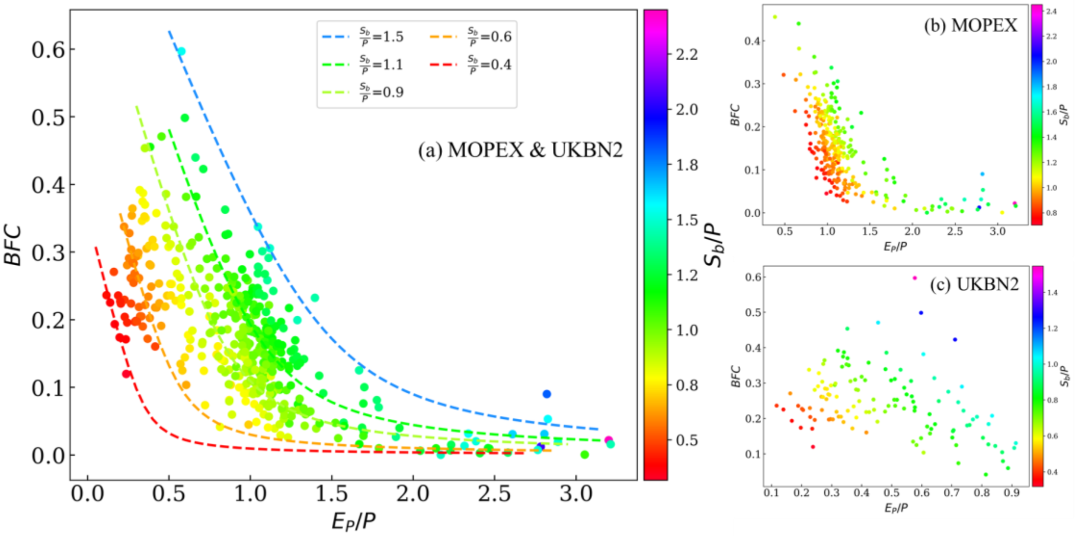

Figure 4.7: The controls of climate aridity index $\left(\frac{E_P}{P}\right)$ and storage capacity index $\left(\frac{S_b}{P}\right)$ on baseflow coefficient (BFC) in the MOPEX and the UKBN2 catchments. The curves are obtained based on Equation (4.18) with $\frac{S_b}{P}$ =1.5, 1.1, 0.9, 0.6 and 0.4, and a=1.90 which is the median of the estimated values from all the study catchments.

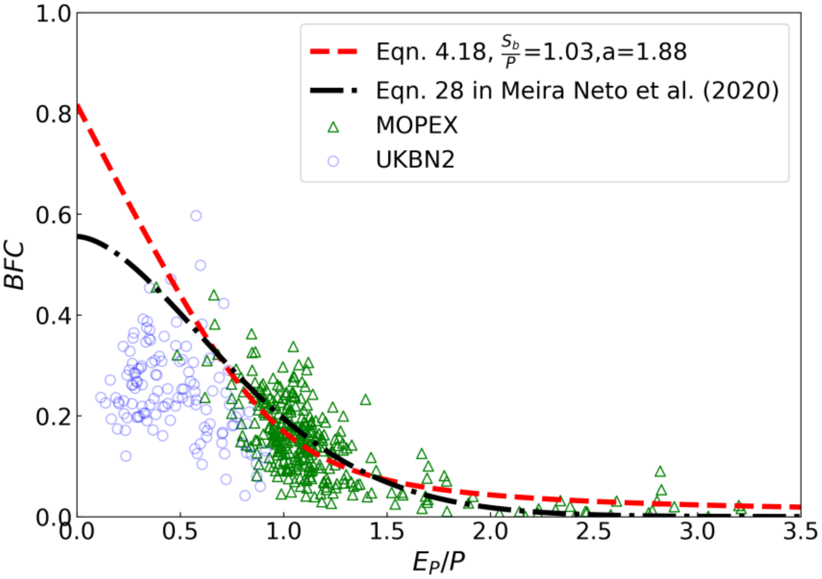

Figure 4.8: Comparison of observed relation and Equation (4.18) with $\frac{S_b}{P}$ =1.03 and a =1.88, and comparison of observed relation and Equation (4.28) from Meira Neto et al. (2020) between baseflow coefficient (BFC) and climate aridity index $\left(\frac{E_P}{P}\right)$.

4.3.4 Impacts of Climate Variability on Mean Annual Baseflow

As introduced in Section 4.2.5, four sets of BFI and BFC were obtained for each catchment from the PDM-D model driven by four climate inputs, i.e., daily climate, monthly climate, annual climate, and mean annual climate, respectively. Figures 4.9a, 4.9b, and 4.9c present the comparisons of the simulated BFI forced by different climate inputs, and Figures 4.9d, 4.9e, 4.9f for BFC. The deviations of the points from the 1:1 line in Figure 4.9a (4.9d) reflect the role of intra-monthly variability in climate inputs on BFI (BFC) since monthly time series of climate does not encompass intra-monthly variability in climate inputs, which is included in the climate forcings/inputs at daily time scale. Likewise, the deviations in Figure 4.9b (4.9e) represent the role of intra-annual variability in climate inputs (i.e., seasonality) on BFI (BFC), and the deviations in Figure 4.9c (4.9f) indicate the importance of inter-annual variability in climate forcings on BFI (BFC). It can be found that BFI is significantly affected by climate forcings prescribed at different time scales, and BFC is much less affected. That is because the fast flow, which is a component of total streamflow, is sensitive to finer time scale climate inputs, while the storage capacity attenuates the effects of variability in climate forcings on baseflow. Almost all points in Figures 4.9a-4.9c are above the 1:1 line, indicating that BFI decreases as more temporal variabilities in climate forcings are considered, because the estimated fast flow increases significantly, and this change in fast flow is much larger compared to that in baseflow. In quantifying the role of climate forcings at different time scales, representing the intra-annual variability has the largest impacts on BFI and BFC. This result is in line with (Beck et al., 2013) which found that the seasonality of precipitation and potential evapotranspiration are important for estimating BFI using regression analysis.

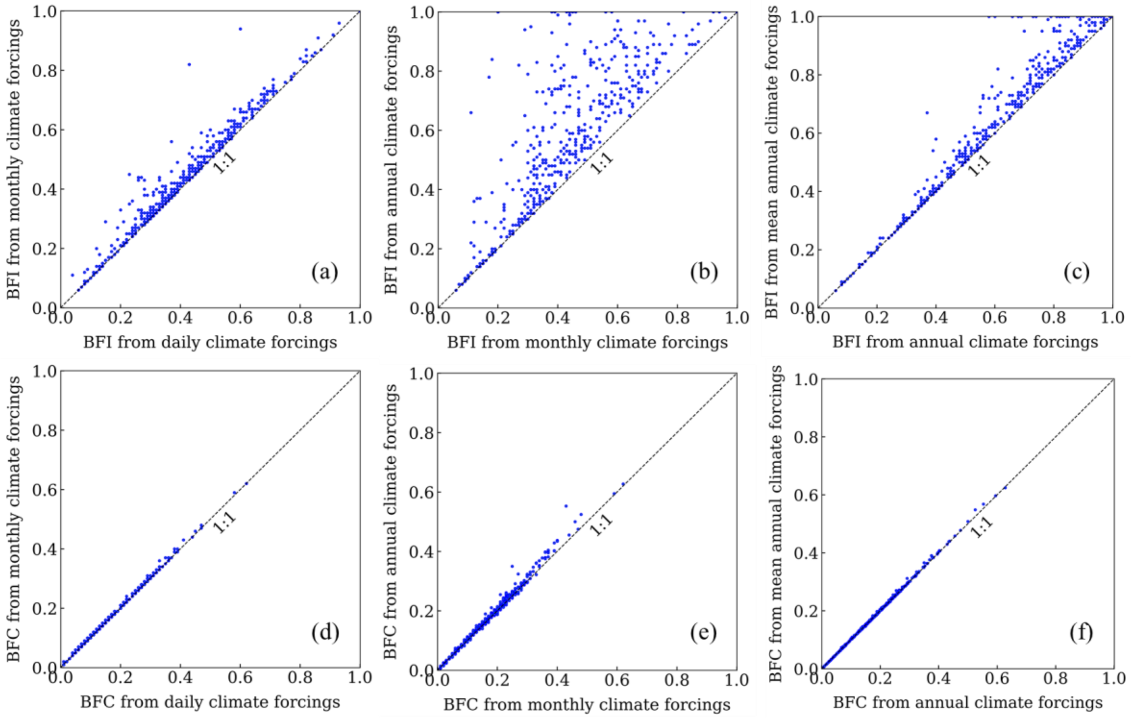

Figure 4.9: Comparisons between the simulated baseflow indexes (BFI) forced by different climate inputs (a, b, c); and comparisons between the simulated baseflow coefficients (BFC) forced by different climate inputs (d, e, f).

4.4 Conclusion

This study has examined the roles of climate and storage capacity on the long-term baseflow by developing new equations for characterizing water competitions in the two-stage precipitation partitioning framework. Particularly, baseflow index and baseflow coefficient are presented as functions of climate aridity index, soil water storage capacity index, and a shape parameter quantifying the spatial heterogeneity of soil water storage capacity. The new method was applied to 435 catchments from both the contiguous U.S. and U.K. to explain different baseflow responses quantitatively. Findings from the study revealed the critical role of soil water storage capacity on baseflow. Most study catchments showed a similar shape parameter; therefore, impact of landscape characteristics on baseflow was mainly attributed to storage capacity index.

In general, baseflow index or baseflow coefficient increases with storage capacity index given a climate condition, and it decreases with climate aridity index given a storage capacity index.

This study explicitly disentangled the roles of climate and landscape properties on baseflow based on a probability distribution model. One key advantage of the new method is that its parameters clearly describe the climate and landscape characteristics, which are much straightforward compared the abstract parameters used in the generalized proportionality relationship since the generalized proportionality is based on empirical formulations of the SCS curve number method. The parameterization for the initial abstraction term in the new method offers another advantage that the functional forms for baseflow index and baseflow coefficient are smooth and differentiable instead of piecewise functions. This study advances our understanding of the role of landscape through storage capacity and its spatial variability in controlling baseflow. Moreover, it was found that storage capacity index in the study catchments can be approximated as a function of climate aridity index, reflecting the dependence of landscape on climate and indicating further evidence of possible coevolution of climate and catchment landscape. This study also demonstrated that temporal variability in climate forcings impacts baseflow index and baseflow coefficient, especially the intra-annual variability (i.e., seasonality).

The findings of this study extend our knowledge of the controlling factors on baseflow which is essential for hydrologists, ecologists, and water resources managers to evaluate the availability and vulnerability of baseflow in the changing environment. However, the soil water storage capacity parameters in this study were estimated numerically based on the streamflow and baseflow observations. This method may not be applicable to ungagged catchments; therefore, quantification of soil water storage capacity and its spatial variability (e.g., Gao et al., 2014) could be useful for estimating baseflow. Furthermore, this study mainly focused on index-based relationships between mean annual baseflow and climatic and catchment landscape properties, whilst process-based methods interpreting hydrological processes in greater detail are needed in the future to understand baseflow at smaller timescales.

CHAPTER FIVE: HYDROLOGICAL BASIS OF DIFFERENT BUDYKO EQUATIONS

5.1 Introduction

Water balance at various temporal and spatial scales has been an enduring research question in hydrology. Empirical equations have been developed for modeling mean annual evaporation as a function of mean annual precipitation and potential evaporation (Choudhury, 1999; Mezentsev, 1955; Ol'dekop, 1911; Pike, 1964; Schreiber, 1904; Turc, 1954). Based on observations from a large number of catchments, Budyko (1974) hypothesized that climate aridity index (i.e., the ratio between mean annual potential evaporation and precipitation, $\frac{E_P}{P}$) is the dominant controlling factor on evaporation ratio (i.e., the ratio between mean annual evaporation and precipitation, $\frac{E}{P}$). Thereafter, the function for the relationship between evaporation ratio and climate aridity index is named as Budyko curve or equation (Milly, 1994; Sivapalan et al., 2011; Ye et al., 2015). The impacts of other factors on evaporation ratio have been studied based on this framework, such as vegetation (Donohue et al., 2007; Yang et al., 2007; Zhang et al., 2001; Zhang et al., 2016), storage capacity (Porporato et al., 2004; Sankarasubramanian & Vogel, 2002), rainfall characteristics (Gerrits et al., 2009; Padrón et al., 2017), and snow(Berghuijs et al., 2014).

Research progress has also been made on the derivation of Budyko equation. Fu (1981) derived a one-parameter Budyko equation by combining dimensional analysis with mathematical reasoning (see Zhang et al., 2004 for details). Greve et al. (2015) introduced a probabilistic framework to the Budyko equation. Yang et al. (2008) derived a Budyko equation as a solution of a set of partial differential equations, and the Budyko equation has the same functional form as the empirical equation by Mezentsev (1955) and Choudhury (1999), therefore called MCY equation hereinafter. Zhou et al. (2015) proposed a concept of generating function to derive

Budyko equation. Sposito (2017) argued that the assumption, that evaporation is a homogenous function of precipitation and potential evaporation, is both necessary and sufficient to derive the Budyko equation. These equations are derived for satisfying the constraint of upper bound which is determined by water demand (i.e., $\frac{E}{P} = \frac{E_P}{P}$ when $\frac{E_P}{P} \leq 1$) and water supply (i.e., $\frac{E}{P} = 1$ when $\frac{E_P}{P} > 1$), as well as the boundary conditions, i.e., $\frac{E}{P} \rightarrow 0$ as $\frac{E_P}{P} \rightarrow 0$, and $\frac{E}{P} \rightarrow 1$ as $\frac{E_P}{P} \rightarrow \infty$. However, the physical meaning of the parameters in these derived Budyko equations are not explicitly linked to hydrologic variables since the derivations are through mathematical reasoning

Another important component of Budyko curve is the lower bound. Mathematically, the lower bound of Budyko curve is the x-axis (i.e., $\frac{E}{P} = 0$). However, the observed data points are shown to cluster in a small region of the $\frac{E}{P} \sim \frac{E_P}{P}$ plot instead of scattering in the entire domain between the upper bound (water and energy limits) and the x-axis, because of which the earlier hydrologists fitted deterministic curves to the observations of $\frac{E}{P}$ versus $\frac{E_P}{P}$ (Budyko, 1974; Mezentsev, 1955; Ol'dekop, 1911; Pike, 1964; Schreiber, 1904; Turc, 1954). Therefore, the lower bound of Budyko curve is above the x-axis and not far from the upper bound. In another word, the observed data are located in a small region below the upper bound. This component of Budyko curve has been used as an example to explain the co-evolution of catchments (Ehret et al., 2014; Harman & Troch, 2014; Li et al., 2014; Sivapalan, 2018; Zhao et al., 2016). It is not straightforward, if not impossible, to use the derived Budyko equations from mathematical reasoning (e.g., Fu equation and MCY equation) to explain such lower bound. Wang & Tang (2014) derived a Budyko equation by applying the proportionality hypothesis of SCS curve number method, which is a popular model for estimating direct runoff for rainfall events, to long-term water balance. The derived Budyko equation provides a lower bound which matches the reported data for catchments around the world by L. Zhang et al. (2004).

Though Budyko equations have been increasingly used in interpreting long-term water balance, few studies have been conducted to explore the hydrological basis of Budyko equations (Berghuijs et al., 2020). Recently, Chen & Sivapalan (2020) has demonstrated the role of storage water in explaining the functional form of Budyko equation. The main objective of this paper is to further explore the effects of available water in determining the emergence of the long-term water balance behavior in the Budyko framework, and demonstrate that different forms of Budyko equations are the emergent outcomes of the spatial distribution of available water for evaporation. Moreover, we will show that the lower bound of Budyko equations emerges as a result of spatial distribution of available water for evaporation. Section 5.2 introduces the spatial distribution functions of available water for evaporation. Section 5.3 shows the outcomes of different distribution functions in determining Budyko equations based on the one-stage partitioning of precipitation. Section 5.4 discusses the symmetry and the lower bound of Budyko curve, and Section 5.5 summarizes the findings.

5.2 Spatial Distribution of Available Water for Evaporation

The long-term available water for evaporation at a point in a catchment is denoted as Θ. The available water for evaporation includes vegetation interception, surface water storage, and soil water storage and groundwater storage depending on the root system of vegetation. The value of Θ varies within a catchment due to the spatial heterogeneity of precipitation, soil properties, topography, and vegetation (Fan et al., 2017; Gao et al., 2019; Jothityangkoon et al., 2001; Milly, 1994; Troch et al., 2002; Western et al., 1999). The spatial variation of point-scale available water for evaporation is represented by a distribution function, and its cumulative probability is denoted by $F(\Theta)$, i.e., the fraction of catchment area for which the available water for evaporation is less than or equal to Θ. The spatial distribution of available water for evaporation, has been modeled by gamma distribution (Entekhabi & Eagleson, 1989; Famiglietti & Wood, 1994), lognormal distribution (Sivapalan & Wood, 1986), beta distribution (Famiglietti et al., 1999), and Gaussian mixture model (Ryu & Famiglietti, 2005). The distribution function proposed by Wang (2018) for the soil water storage capacity is used for describing mean annual available water for evaporation as an example for demonstrating its controlling effect in determining the long-term water balance:

$$F(\Theta) = 1 - \frac{1}{\phi} + \frac{\Theta + (1-\phi)\mu}{\phi\sqrt{(\Theta+\mu)^2 - 2\phi\mu\Theta}} \tag{5.1}$$

where ϕ is the shape parameter and $0 < \phi < 2$; and μ is the mean of the distribution, i.e., the average available water for evaporation at the catchment scale. This distribution function has been used for describing the spatial distribution of water storage capacity for modeling saturation excess runoff generation (Wang, 2018). Figure 5.1a plots the cumulative distribution function (CDF) for μ=1000 mm and ϕ=0.0001, 1.50 and 1.99. Parameter ϕ controls the shape of the curves. In the following section, Equation (5.1) and some other distribution functions (e.g., exponential, gamma, and lognormal distributions) will be used as examples to show that different functional forms of Budyko equation are results from different distribution functions of available soil water.

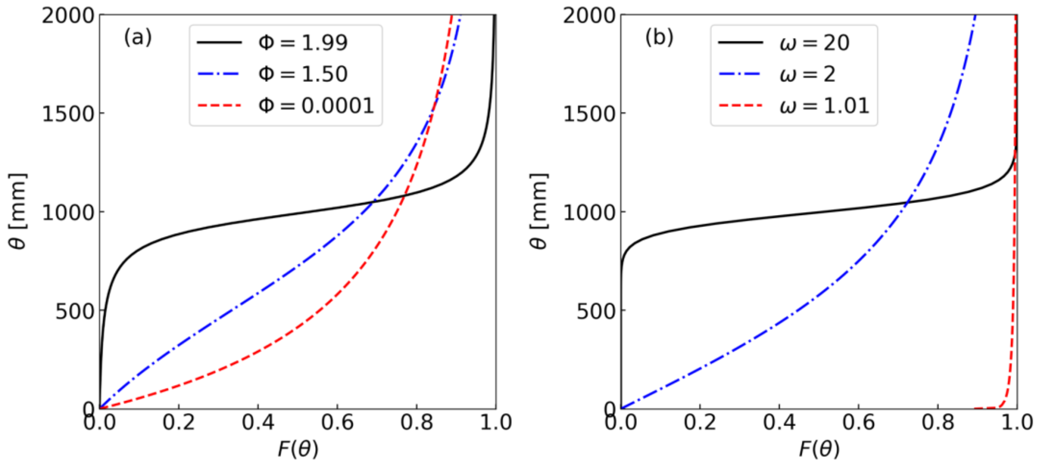

Figure 5.1: Two cumulative distribution functions for describing the spatial variability of available water for evapotranspiration in a catchment: (a) the cumulative distribution function represented by equation (1) where ϕ is shape parameter (0<ϕ<2); and (b) the cumulative distribution function corresponding to Fu's equation where ϖ is shape parameter (ϖ >1). The mean (μ) is set to 1000 mm.

5.3 Emergence of Budyko Curve Based on One-stage Precipitation Partitioning Concept

For one-stage partitioning of precipitation, mean annual precipitation (P) is partitioned into runoff (Q) and evaporation (E):

$$P = Q + E \tag{5.2}$$

Mean annual evaporation is computed based on the distribution function of available water for evaporation as shown in Figure 5.2. The shaded area in Figure 5.2a represents the catchment average of available water for evaporation, i.e., μ in Equation (5.1). The average available water for evaporation is precipitation; therefore, the shaded area in Figure 6.2a equals mean annual precipitation:

$$\mu = P \tag{5.3}$$

Actual evaporation at a point j in the catchment is denoted as E_j. The value of E_j is dependent on the available water (Θ_j) at the point and potential evaporation (E_p). It is reasonable to assume that potential evaporation is uniform over the catchment when the catchment area is small (e.g., a magnitude of 100~1000 km^2). At a point, when available water Θ_j is greater than potential evaporation, actual evaporation E_j equals potential evaporation; otherwise, E_j equals available water Θ_j:

$$E_j = min(\Theta_j, E_p) \tag{5.4}$$

Therefore, the average actual evaporation (E) at the catchment scale is represented by the shaded area in Figure 5.2b:

$$E = \int_0^{E_p} \big(1 - F(\Theta)\big) d\Theta \tag{5.5}$$

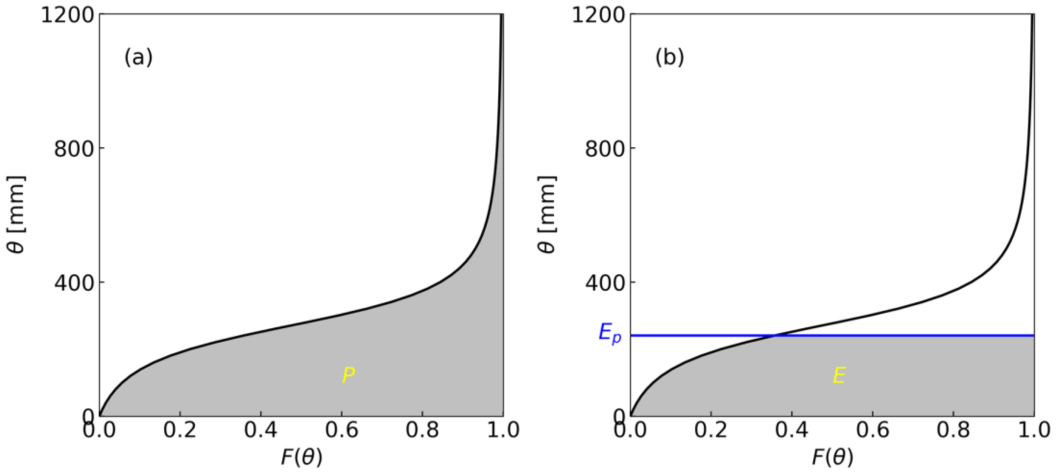

Figure 5.2: Mean annual evaporation based on one-stage precipitation partitioning: a) mean annual precipitation is the catchment-scale average of available water for evaporation; and b) catchment-scale average of mean annual evaporation.

5.3.1 Deterministic Budyko Equation

Equation (5.5) provides a framework for deriving Budyko equations from any distribution functions that describe the spatial variability of available water with $\Theta \geq 0$. If the distribution has one parameter, the derived Budyko equation is deterministic. For example, if exponential distribution is used for describing the spatial distribution of Θ, i.e., the CDF of Θ is $F(\Theta) = 1 -$

$e^{-\lambda\Theta}$. The mean of the exponential distribution is $\frac{1}{\lambda} = P$. Evaporation ratio is computed as $\frac{E}{P} = \frac{1}{P}\int_0^{E_p} e^{-\frac{\Theta}{P}} d\Theta = 1 - e^{-\frac{E_p}{P}}$ which is the Schreiber equation (Schreiber, 1904).

5.3.2 One-parameter Budyko Equation

5.3.2.1 SCS Distribution

If $F(\Theta)$ has two parameters, the corresponding Budyko equation has one parameter. For example, substituting Equation (5.1) into Equation (5.5) and replacing μ by P, E is obtained by integration of the shaded area in Figure 5.2b, and the following equation for computing evaporation ratio is easily obtained:

$$\frac{E}{P} = \frac{1+\frac{E_p}{P}-\sqrt{\left(1+\frac{E_p}{P}\right)^2-2\phi\frac{E_p}{P}}}{\phi} \tag{5.6}$$

Equation (5.6) is same as the derived one-parameter Budyko equation by applying proportionality hypothesis to mean annual water balance (Wang & Tang, 2014), which implicates that the proportionality relationship can be derived from the distribution shown in Equation (5.1). Comparing Equation (5.6) with the derived Budyko equation in (Wang & Tang, 2014), the parameters have the following relation:

$$\phi = 2\varepsilon(2-\varepsilon) \tag{5.7}$$

where ε is defined as the ratio between initial evaporation and total evaporation and the range of ε is between 0 and 1 (i.e., ϕ is between 0 and 2).

5.3.2.2 Gamma Distribution

Different spatial distribution of available for evaporation results in different one-parameter Budyko equations. For example, if the spatial variability of available water for evaporation is in a form of gamma distribution, and the CDF is:

$$F(\Theta) = \frac{\gamma\left(k, \frac{k\Theta}{\mu}\right)}{\Gamma(k)} \tag{5.8}$$

where μ is the mean value; k is the shape parameter ($k > 0$); $\Gamma(k)$ is the gamma function and $\Gamma(k) = \int_0^\infty x^{k-1} e^{-x} dx$; $\gamma\left(k, \frac{k\Theta}{\mu}\right)$ is the lower incomplete function and $\gamma\left(k, \frac{k\Theta}{\mu}\right) = \int_0^{\frac{k\Theta}{\mu}} x^{k-1} e^{-x} dx$. Substituting Equation (5.8) into Equation (5.5), we obtain:

$$E = \int_0^{E_p} \left[1 - \frac{\gamma\left(k, \frac{k\Theta}{\mu}\right)}{\Gamma(k)}\right] d\Theta \tag{5.9}$$

Equation (5.9) is re-written as:

$$E = \frac{1}{\Gamma(k)} \int_0^{E_p} \left[\int_{\frac{k\Theta}{\mu}}^{\infty} t^{k-1}\, e^{-t} dt\right] d\Theta \tag{5.10}$$

By changing order of double integration, Equation (5.10) becomes:

$$E = \frac{1}{\Gamma(k)} \int_0^{\frac{k}{\mu}E_p} t^{k-1} e^{-t} dt \left[\int_0^{\frac{\mu}{k}t} d\Theta\right] + \frac{1}{\Gamma(k)} \int_{\frac{k}{\mu}E_p}^{\infty} t^{k-1} e^{-t} dt \left[\int_0^{E_p} d\Theta\right] \tag{5.11}$$

After integrating $d\Theta$, Equation (5.11) becomes:

$$E = \frac{\mu}{k\Gamma(k)} \int_0^{\frac{k}{\mu}E_p} t^k e^{-t} dt + \frac{E_p}{\Gamma(k)} \int_{\frac{k}{\mu}E_p}^{\infty} t^{k-1} e^{-t} dt \tag{5.12}$$

which leads to:

$$E = \frac{1}{\Gamma(k)} \left[\frac{\mu}{k} \gamma\left(k+1, \frac{k}{\mu} E_p\right) + E_p \Gamma\left(k, \frac{k}{\mu} E_p\right)\right] \tag{5.13}$$

where $\gamma\left(k+1,\frac{k}{\mu}E_p\right)$ is the lower incomplete gamma function, and $\Gamma\left(k,\frac{k}{\mu}E_p\right)$ is the upper incomplete gamma function. For one-stage partitioning of precipitation, the mean of available water for evaporation equals mean annual precipitation, $\mu = P$. Therefore, Equation (5.13) becomes:

$$E = \frac{1}{\Gamma(k)}\left[\frac{P}{k}\gamma\left(k+1, k\frac{E_p}{P}\right) + E_p\Gamma\left(k, k\frac{E_p}{P}\right)\right] \tag{5.14}$$

Dividing P on both hand sides of Equation (5.14), we obtain:

$$\frac{E}{P} = \frac{1}{\Gamma(k)}\left[k^{-1}\gamma\left(k+1, k\frac{E_p}{P}\right) + \frac{E_p}{P}\Gamma\left(k, k\frac{E_p}{P}\right)\right] \tag{5.15}$$

Equation (5.15) is the Budyko equation corresponding to gamma distribution.

5.3.2.3 Lognormal Distribution

Lognormal distribution is also shown to be a good conceptualization of the spatial heterogeneity of available water for evaporation (Sivapalan & Wood, 1986):

$$F(\Theta) = \frac{1}{2} + \frac{1}{2}erf\left(\frac{\ln\frac{\Theta}{\mu}+\frac{\sigma^2}{2}}{\sqrt{2}\sigma}\right) \tag{5.16}$$

where μ is the mean of the random variable Θ; σ is the standard deviation of the variable's natural logarithm (i.e., $\ln\Theta$); and $erf(..)$ is the error function. As was mentioned, $\mu = P$ in one-stage precipitation partitioning. Substituting Equation (5.16) into Equation (5.5) we obtain:

$$E = \int_0^{E_p}\left[\frac{1}{2} - \frac{1}{2}erf\left(\frac{\ln\frac{\Theta}{P}+\frac{\sigma^2}{2}}{\sqrt{2}\sigma}\right)\right]d\Theta \tag{5.17}$$

After integration of the right hand side of Equation (5.17), the following equation can be obtained:

$$E = \frac{1}{2}E_p - \frac{1}{2}E_p erf\left[\frac{\frac{\sigma^2}{2}+\ln\left(\frac{E_p}{P}\right)}{\sqrt{2}\sigma}\right] + P\Phi\left[-\frac{\frac{\sigma^2}{2}-\ln\left(\frac{E_p}{P}\right)}{\sigma}\right] \tag{5.18}$$

where $\Phi(x) = \int_{-\infty}^{x} \frac{1}{\sqrt{2\pi}} e^{-z^2/2} dz$ is the standard normal cumulative distribution function. Therefore, we obtain the following Budyko equation corresponding to lognormal distribution:

$$\frac{E}{P} = \frac{1}{2}\frac{E_p}{P} - \frac{1}{2}\frac{E_p}{P} erf\left[\frac{\frac{\sigma^2}{2} + \ln\left(\frac{E_p}{P}\right)}{\sqrt{2}\sigma}\right] + \Phi\left[-\frac{\frac{\sigma^2}{2} - \ln\left(\frac{E_p}{P}\right)}{\sigma}\right] \tag{5.19}$$

Since this equation satisfies the condition of $g(x) = xg\left(\frac{1}{x}\right)$, this Budyko equation is symmetric for E_p and P. Therefore, Equation (5.19) can be written as:

$$\frac{E}{P} = \frac{1}{2} - \frac{1}{2} erf\left[\frac{\frac{\sigma^2}{2} - \ln\left(\frac{E_p}{P}\right)}{\sqrt{2}\sigma}\right] + \frac{E_p}{P}\Phi\left[-\frac{\frac{\sigma^2}{2} + \ln\left(\frac{E_p}{P}\right)}{\sigma}\right] \tag{5.20}$$

Similar derivation can be accomplished with any distribution functions for non-negative random variables. Table 5.1 shows 1 single-parameter distribution function and 5 two-parameter distribution functions and their corresponding Budyko equations. The fifth distribution function with parameters ϖ and μ (mean) leads to Fu's equation, and the sixth one with parameters n and μ (mean) leads to the MCY equation. All the Budyko equations in Table 5.1 satisfy the boundary conditions: $\frac{E}{P} \to 0$ as $\frac{E_p}{P} \to 0$; and $\frac{E}{P} \to 1$ as $\frac{E_p}{P} \to \infty$. For demonstration, the one-parameter Budyko equation derived from Equation (5.1) and that from gamma distribution (i.e., Equation (5.8)) are plotted in Figure 5.3a and Figure 5.3b, respectively.

For a specific catchment, different distribution functions would not bring much difference in modeling the spatial distribution of available water for evaporation. Figure 5.4 shows the modeling results for the Licking River in Kentucky (USGS gage number 03253500). Mean annual precipitation, potential evaporation and runoff in this catchment is 1128 mm, 821 mm, and 429 mm, respectively. Mean annual evaporation is approximated as the difference between precipitation and runoff, i.e., 699 mm. Therefore, $\frac{E_P}{P}$ is 0.728, and $\frac{E}{P}$ is 0.620. The parameters of the distributions in Table 5.1 are computed based on the observed values of $\frac{E_P}{P}$ and $\frac{E}{P}$: ϕ =1.785, k =2.536, σ =0.649, ϖ =3.092, and n =2.386. As can been seen from Figure 5.4, the differences among the five CDF curves are not significant.

Table 5.1: The cumulative distribution functions (CDF) are used for describing the spatial variability of available water for evaporation, and Budyko-type equations are derived for one-stage partitioning of precipitation based on the corresponding CDFs.

Index	**CDF, $F(\Theta)$**	**Budyko equation**
1	$1-e^{-\frac{\Theta}{\mu}}$	$1-e^{-\frac{E_p}{P}}$
2	$1-\frac{1}{\phi}+\frac{\Theta+(1-\phi)\mu}{\phi\sqrt{(\Theta+\mu)^2-2\phi\mu\Theta}}$, $0<\phi<2$	$\frac{E}{P}=\frac{1+\frac{E_p}{P}-\sqrt{\left(\frac{E_p}{P}+1\right)^2-2\phi\frac{E_p}{P}}}{\phi}$
3	$\frac{\gamma\left(k,\frac{k\Theta}{\mu}\right)}{\Gamma(k)}$, $k>0$	$\frac{E}{P}=\frac{1}{\Gamma(k)}\left[k^{-1}\gamma\left(k+1,k\frac{E_p}{P}\right)+\frac{E_p}{P}\Gamma\left(k,k\frac{E_p}{P}\right)\right]$
4	$\frac{1}{2}+\frac{1}{2}erf\left(\frac{\ln\frac{\Theta}{\mu}+\frac{\sigma^2}{2}}{\sqrt{2}\sigma}\right)$, $\sigma>0$	$\frac{E}{P}=\frac{1}{2}-\frac{1}{2}erf\left[\frac{\frac{\sigma^2}{2}-\ln\left(\frac{E_p}{P}\right)}{\sqrt{2}\sigma}\right]+\frac{E_p}{P}\Phi\left[-\frac{\frac{\sigma^2}{2}+\ln\left(\frac{E_p}{P}\right)}{\sigma}\right]$
5	$\left[1+\left(\frac{\mu}{\Theta}\right)^{\varpi}\right]^{\frac{1}{\varpi}-1}$, $\varpi>1$	$\frac{E}{P}=1+\frac{E_p}{P}-\left[\left(\frac{E_p}{P}\right)^{\varpi}+1\right]^{\frac{1}{\varpi}}$
6	$1-\left[1+\left(\frac{\mu}{\Theta}\right)^{-n}\right]^{-\frac{1}{n}-1}$, $n>0$	$\frac{E}{P}=\left[\left(\frac{E_p}{P}\right)^{-n}+1\right]^{-\frac{1}{n}}$

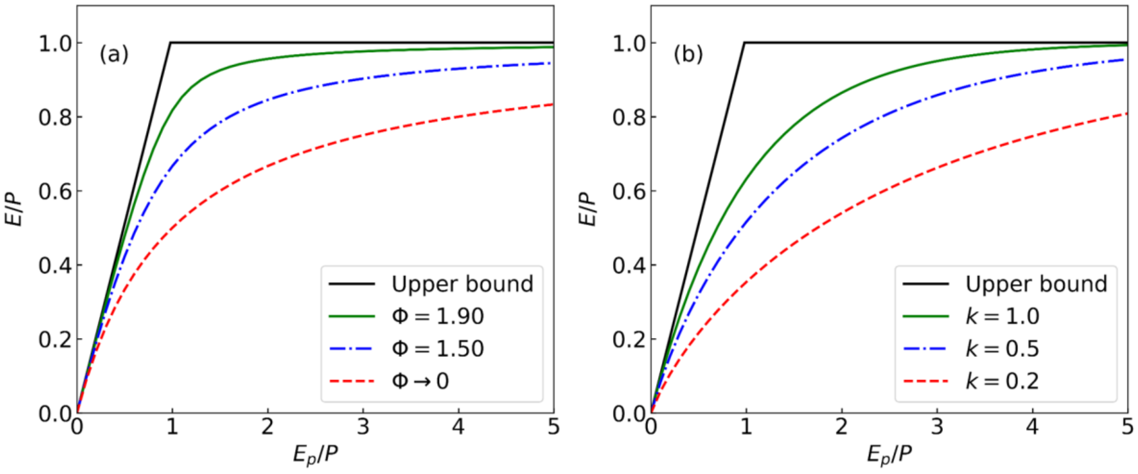

Figure 5.3: The derived Budyko-type equations from (a) the distribution function represented by equation (1); and (b) gamma distribution.

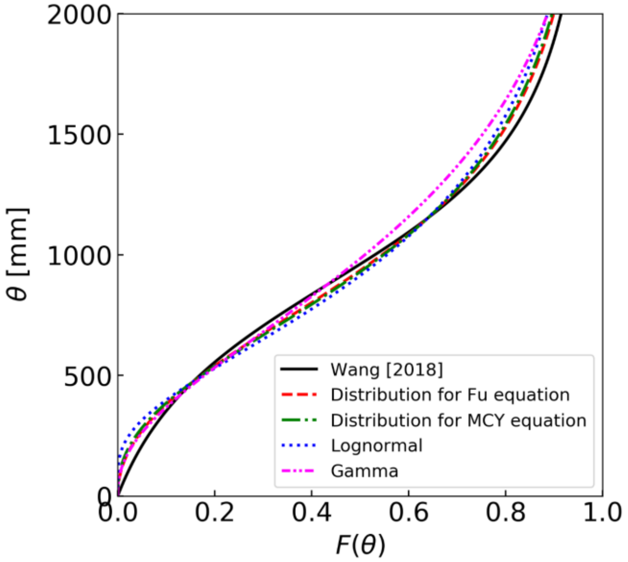

Figure 5.4: The cumulative distribution functions of available water for evaporation for Licking River in Kentucky (USGS gage number 03253500). The parameters of the distribution functions are estimated based on mean annual values of precipitation (P), potential evaporation (E_P), and runoff (Q). Mean annual evaporation is computed as the difference between P and Q.

5.4 Discussions

5.4.1 Symmetry Between Precipitation and Potential Evaporation

Precipitation and potential evaporation are symmetric if the Budyko equation does not change by switching P and E_P. For example, if a Budyko equation is written as $\frac{E}{P} = g\left(\frac{E_p}{P}\right)$, for the symmetric case the relationship between $\frac{E}{E_p}$ and $\frac{P}{E_p}$ has the same functional form, i.e., $\frac{E}{E_p} = g\left(\frac{P}{E_p}\right)$. In another word, a symmetric Budyko equation satisfies the following condition: $g(x) = xg\left(\frac{1}{x}\right)$. The normalized random variable by its mean is denoted as:

$$z = \frac{\Theta}{\mu} \tag{5.21}$$

If the probability density function (PDF), $f(z)$, satisfies the following condition:

$$f(z) = \frac{1}{z^3} f\left(\frac{1}{z}\right) \tag{5.22}$$

the derived Budyko equation from the CDF corresponding to PDF of $f(z)$ satisfies the condition of symmetry. P and E_P are symmetric in the Budyko equations derived from the SCS, lognormal, Fu and MCY distributions. However, the Budyko equation from the gamma distribution does not satisfy this symmetric condition.

5.4.2 Lower Bound of Budyko Curve

The Budyko equation based on the distribution function represented by Equation (1) has a different lower bound compared with other four Budyko equations in Table 5.1. The ranges of the shape parameters for the five distribution functions are: $0 < \phi < 2,\ k > 0, \sigma > 0, \varpi > 1,$ and $n > 0$. The upper bounds of the curves are same for all the Budyko equations, i.e., the energy limit and water limit (black solid lines in Figure 5.3); and the parameter values corresponding to the upper bound are $\phi \to 2,\ k \to \infty, \sigma \to 0,\ \varpi \to \infty,$ and $n \to \infty,$ The parameter values corresponding to the lower bound are $\phi \to 0, \varpi \to 1, n \to 0, k \to 0,$ and $\sigma \to \infty.$ The lower bound for the distribution represented by Equation (5.1) is the dashed red curve ($\phi \to 0$) in Figure 5.3a. However, the lower bounds for the other four Budyko equations are located on the x-axis, i.e., $\frac{E}{P} = 0$. Therefore, the feasible space for the first Budyko equation derived from Equation (1) is much smaller than the other ones. This feasible space explains the reason that hydrologists fitted their observations with deterministic curve (Budyko, 1974; Ol'dekop, 1911; Pike, 1964; Schreiber, 1904; Turc, 1954). (Wang & Tang, 2014)showed that the lower bound with $\phi \to 0$ matches the observations from global catchments reported by (Zhang et al., 2004).

The lower bound is an emergent behavior of catchments due to the spatial organization of available water for evaporation. Figure 5.1a plots the CDF for Budyko equation represented in Equation (5.6), and Figure 5.1b plots the CDF corresponding to Fu equation. The CDFs for the upper bound (black solid lines in Figure 5.3) are approximately represented by the CDF with ϕ=1.99 (Figure 1a) and ϖ=20 (Figure 5.1b), and they are close. The CDFs for $\phi \rightarrow 2$ and $\varpi \rightarrow \infty$ are almost uniform distributions, and the catchment scale evaporation is determined by Equation (5.4), i.e., the upper bound. However, the distribution with $\phi \rightarrow 0$ (see dashed red curve in Figure 5.1a) and the distribution with $\varpi \rightarrow 1$ (see dashed red curve in Figure 5.1b) are quite different. The CDF with $\phi \rightarrow 0$ is above the CDF with $\varpi \rightarrow 1$. Therefore, the CDF curves represented by Equation (5.1) cannot be squeezed to the right as much as the CDF curves represented by the distribution function leading to Fu equation. The CDFs with $\phi \rightarrow 0$ and $\varpi \rightarrow 1$ are corresponding to their lower bounds, respectively. Therefore, the lower bound of Budyko curve represented by Equation (5.1) could be explained as an extreme case of the possible spatial distribution of available water for evaporation. In real world, the distribution of available water for evaporation potentially varies from dashed red curve to solid black curve shown in Figure 5.1a. This spatial organization can be explained as a result of catchment co-evolution (Sivapalan, 2018).

5.5 Conclusion

In this paper, the spatial distribution of available water for evaporation in a catchment is quantified by a distribution function. Evaporation at the point scale is modeled as the smaller one between potential evaporation and available water. Average evaporation at the catchment scale is computed from the distribution function based on the one-stage precipitation partitioning concept. We demonstrate that the spatial distribution of available water for evaporation determines the emergence of different functional form of Budyko curves. If the available water follows a distribution function with has one parameter, the Budyko equation is deterministic; and if the distribution function has two parameters, the Budyko equation has a single parameter. Moreover, the lower bound of Budyko curve, which determines the feasible space of Budyko curve since the upper bound is determined by the limits of water demand and water supply, is explained by the possible spatial distribution of available water for evaporation. Therefore, the lower bound of Budyko curve is a result of spatial organization of available water for evaporation due to catchment co-evolution. Future research could evaluate the possible distributions based on observed data of spatial heterogeneity of available water storage for evaporation.

CHAPTER SIX: CLIMATIC CONTROL ON THE SPATIAL DISTRIBUTION OF WATER STORAGE

6.1 Introduction

Spatially variable antecedent wetness condition in catchments is a critical factor affecting hydrological processes. It determines the locations of source area for runoff generation and the amount of saturation excess runoff (Clark & Gedney, 2008; Jayawardena & Zhou, 2000; Jothityangkoon et al., 2001), and affects the evaporation process (Gao et al., 2021; Ronda, 2002; Sivapalan & Woods, 1995). Therefore, accounting for the spatial variation of catchment water storage in hydrological models results in more realistic runoff generation and evaporation simulations compared to those models treating catchment as a single bucket. Fully distributed hydrological models, such as MIKE-SHE (Abbott et al., 1986; DHI, 2017), GEOtop (Rigon et al., 2006), and WetSpa (Liu & Smedt, 2004), explicitly account for the spatial variability of physical properties and hydrological processes across catchments. However, the utility of the fully distributed models is typically hampered by its heavy data requirements or computational burden (Fatichi et al., 2016; Semenova & Beven, 2015).

Alternatively, semi-distributed models, such as TOPography-based hydrologic model (TOPMODEL) and Variable Infiltration Capacity model (VIC) which provide implicit description of spatial variability of storage, are extensively used in practice because they are parametrically simple and yet physically realistic (Bartlett et al., 2016). TOPMODEL uses the concept of hydrological similarity to represent catchment heterogeneity, whereby the points with the same topographic wetness index will have the same predicted hydrological response (Beven & Kirkby, 1979; Sivapalan et al., 1987). Therefore, the spatial heterogeneity within a catchment is determined by the spatial distribution of topographic wetness index in TOPMODEL. Moreover, TOPMODEL assumes quasi-steady state dynamics and the hydraulic gradient of groundwater is same as the gradient of land surface topography (Beven & Kirkby, 1979; Sivapalan et al., 1987). Though it is known that water table does not always mirror land surface, it is still a reasonable simplification in regions with topography-controlled water table (Rinderer et al., 2014; Troch et al., 1993). On the other hand, VIC model (Liang et al., 1994; Wood et al., 1992) is one of the Probability Distributed Model (PDM) family which also includes Xinanjiang model (Zhao, 1992) and HyMOD (Moore, 1985), and we will use the VIC-type model to refer to the PDM hereinafter. VIC-type model assumes a statistical distribution, such as the generalized Pareto distribution function (Liang et al., 1994; Zhao, 1992) and the SCS distribution function (Yao et al., 2020), for capturing the spatial variability of maximum water storage capacity (i.e., volumetric capacity from land surface to bedrock). Given a spatially uniform rainfall, VIC-type model assumes a spatially uniform water storage rise across the catchment except in those points where the storage capacity is smaller than the rainfall depth.

Though TOPMODEL and the VIC-type model have been widely used and numerous studies have compared the structure and performance of these two models (Devia et al., 2015; Konapala et al., 2020; Lane et al., 2019; Staudinger et al., 2011; Warrach et al., 2002), only a few studies have explored the relation between them. Sivapalan et al. (1997) and Noto (2014) used the spatial distribution of topographical index as a surrogate of the spatial distribution of maximum soil water storage capacity by assuming a negative linear relationship between the topographical index and soil storage capacity, since topography is closely related to other landscape properties that determine soil water storage capacity and its spatial variation, and topography data is much easier to obtain than soil properties (Gao et al., 2019). Kavetski et al. (2003) considered

TOPMODEL and VIC model as special cases of saturation path modeling since each of them assumes an event-invariant relationship between the saturated area and the catchment storage.

However, the relation between TOPMODEL and VIC-type model has not been discussed from the perspective of the spatial distribution of water storage which varies with climate. The objective of this paper is to gain a better understanding of the spatial variability of water storage (capacity) at the catchment scale under different dryness conditions. It will shed light on the commonality of saturation excess runoff models in terms of their underlying assumptions of the heterogeneously distributed water storage. To achieve this objective, we build a hypothetical model and conduct numerical simulations to model groundwater flow at steady states. The second section introduces the main settings of the numerical model. Section 6.3 presents the spatial distributions of water table and storage in different climates. Section 6.4 discusses the impacts of bedrock topography on the simulations, and the implication of the findings to the unification of saturation excess runoff models. The final section summaries the main findings of this paper.

6.2 Methodology

6.2.1 Land Surface and Bedrock Topography of the Model Domain

The purpose of this paper is not to develop a numerical model mimicking the groundwater system for a specific catchment, but to gain general understanding on the spatial heterogeneity of water storage under different climate humidity conditions using a hypothetical model, and the climate humidity is represented by the net recharge which is uniformly distributed on the land surface. While, the model domain is still delineated by the boundary of a real catchment, i.e., the Crab Orchard Creek catchment located in Illinois (USGS gauge ID: 05597500), which is selected simply because of the availability of both land surface and bedrock elevation data. The drainage area of the model domain is 80 km^2, and the land surface elevation ranges from 129 to 185 m above mean sea level with an average land surface slope of 0.017 as presented in Figure 6.1a.

The lower boundary of the catchment is the observed impeding bedrock as shown in Figure 6.1b, and the average soil thickness, i.e., the vertical distance between land surface and bedrock surface, is 10 m. Bedrock topography in this catchment generally follows the topography of land surface, and the total soil thickness from land surface to bedrock decreases from stream channel to upland.

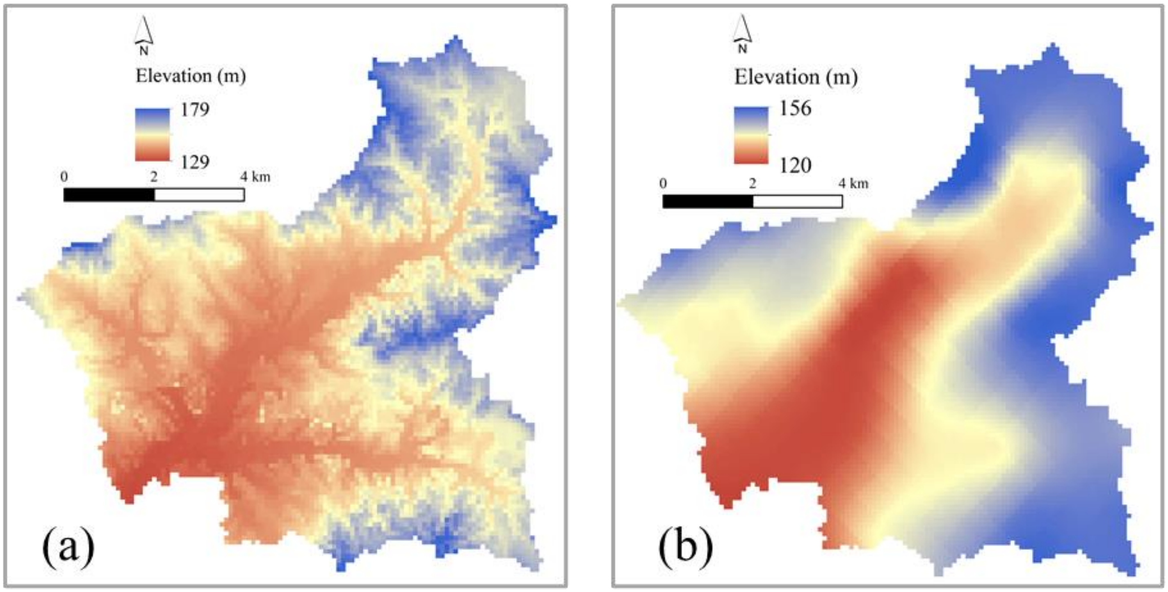

Figure 6.1: (a) The land surface and (b) bedrock topography of the Crab Orchard Creek catchment in Illinois (USGS gauge ID: 05597500) with 100 m resolution.

6.2.2 Model Implementation

The groundwater flow system is developed via numerical simulation using MODFLOW (Panday et al., 2013), and the unstructured grid (USG) version is adopted because of the bedrock outcrops in a few locations. The modeled domain is horizontally discretized into finite difference square cells with a resolution of 100 m × 100 m, leading to a total number of 8019 cells. The model is not discretized vertically considering that the soil thickness is much smaller than the horizontal dimensions by two to five orders of magnitude. A “drain” boundary condition is assigned to the top face of each grid (Goderniaux et al., 2013). Drain boundary is a head-dependent flux boundary, through which water leaves groundwater system when the head is higher than the land surface elevation, and it turns inactive when the head of the model cell drops below the land surface. Discharge of groundwater from an active drain surface is proportional to the drain conductance, which is assumed to be 10^6 m^2/year in this paper and is subject to change as needed. A spatially uniform recharge is applied to the model domain, and different steady-state groundwater levels are obtained by adjusting the value of recharge. The recharge considered here is the net recharge since evaporation is not considered directly in this paper. All other lateral and vertical edges of the model are set as no-flow boundaries. The saturated hydraulic conductivity is assumed to be homogeneous and isotropic. Given land surface and bedrock topography, the ratio of recharge and saturated hydraulic conductivity determines water table configuration, therefore, the absolute value of the saturated hydraulic conductivity (i.e., 315 m/year in this paper) is less important here (Gleeson & Manning, 2008; Haitjema & Mitchell-Bruker, 2005). Water storage at the cell-scale could be determined after each steady-state groundwater table is obtained, and is calculated as the groundwater thickness multiplied by soil porosity. Since the geology is assumed to be homogeneous and isotropic, the value of soil porosity (i.e., 0.417 in this paper) is less important for determining the spatial heterogeneity of water storage given a water table.

6.3 Results

6.3.1 Water Table Configuration in Different Climates

As mentioned in Section 6.2, different values of net recharge were applied on the land surface to model water storage in different climates; therefore, a series of steady state water tables with various values of R/K ranging from 0.003 to 1.8E-07 were obtained. Figure 2a-c displays three groundwater table distributions with the values of R/K as 0.003, 1.6E-05, and 1.8E-07, respectively. Comparing these water table configurations with land surface, it can be found that the similarity between water table and land surface topography decreases as the water table depth decreases in more arid climates. In very humid condition, e.g., R/K=0.003, the spatial variability of water table (Figure 6.2a) is almost identical to the land surface topography (Figure 6.1a), whereas the water table (Figure 6.2b) is much smoother when R/K decreases to 1.6E-05, and the water table (Figure 6.2c) is much different from the land surface when R/K = 1.8E-07. The decreasing similarity between water table and land surface confirms the less control of land surface topography on the shape of water table as the mean water table depth increases (Cuthbert et al., 2019; Gleeson & Manning, 2008). Conversely, the role of bedrock topography is more and more significant in determining water table configuration as climate becomes drier. It can be seen that the similarity between water table configuration and bedrock topography increases as R/K decreases. When climate is very arid, e.g., R/K = 1.8E-07, the distribution of water table elevation is highly similar as that of the bedrock. These results are in agreement with the field observations at the hillslope scale (van Meerveld et al., 2015; Hutchinson & Moore, 2000; Freer et al., 2002)

Compatible with groundwater table configuration, groundwater flow pathways change with climate as well (Detty & McGuire, 2010; Toth, 1963). Figure 6.2d-f show the contours of the corresponding water table in Figure 6.2a-c. Groundwater flow direction is perpendicular to the contours; therefore, it can be observed that in very humid condition (Figure 6.2d) groundwater from hillslopes flows towards immediately adjacent channels, suggesting that local flow systems dominant groundwater circulation. While as R/K decreases (Figure 6.2e-f), groundwater flows across the boundaries of individual hillslopes and merge at higher orders of channels. Note that the channel initiation threshold, i.e., 0.08 km^2, was determined by the 1 % of the maximum flow accumulation in this paper (Maidment, 2002).

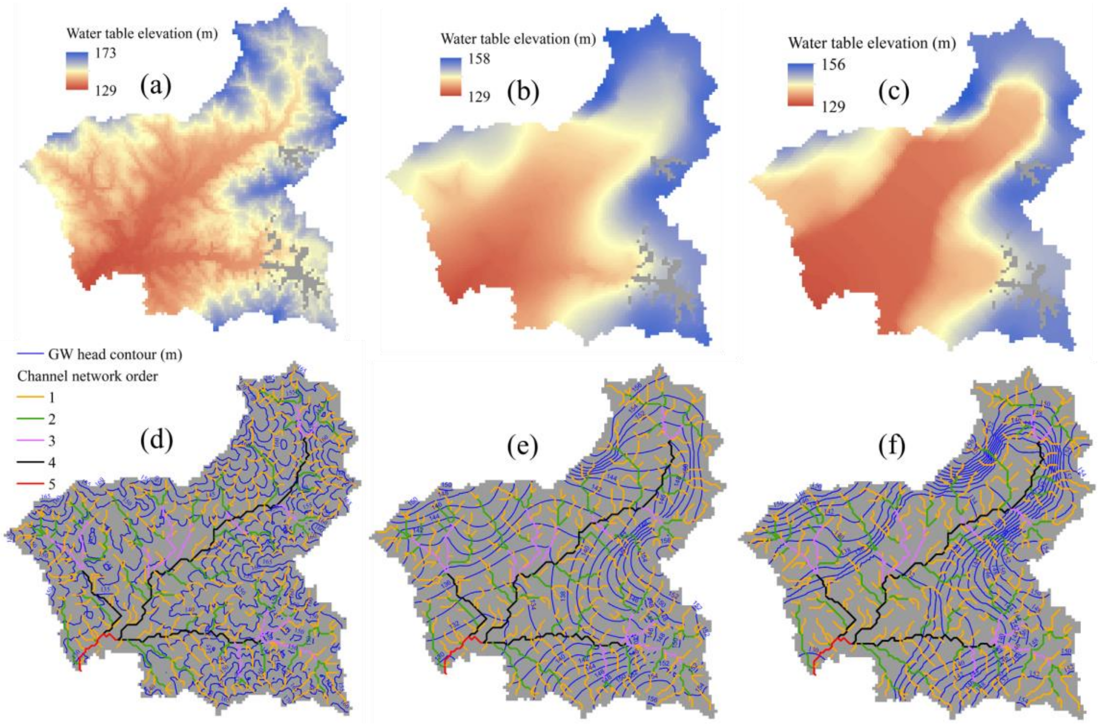

Figure 6.2: The simulated water table elevations when the recharge/hydraulic conductivity equals (a) 0.003, (b)1.6e-5, and (c) 1.8e-7; the contours of water table elevation when the recharge/hydraulic conductivity equals (d) 0.003, (e) 1.6e-5, and (f)1.8e-7. Note that the channel initiation threshold was determined as the 1 % of the maximum flow accumulation (Maidment, 2002)

6.3.2 Percentage of Saturated Land Surface

The percentage of saturated area on land surface is an important factor for determining runoff generation since precipitation falls on the saturated area transfers to surface runoff directly.

Saturated area occurs where the groundwater table intercepts with land surface; therefore, the percentage of saturated area changes with climate. Figure 6.3a presents the percentage of saturated area (defined as the ratio between the flooded area and the total area in the model) as a function of R/K. The linear curve on the log-log plot suggests that the saturated area follows a power function relationship with respect to the dimensionless value, i.e., R/K. Moreover, Figure 6.3b presents the percentage of saturated area as a function of mean water table depth for simulations on the semi-log plot. The roughly linear curve indicates that the saturated area follows an exponential function relationship with respect to mean water table depth, which is in agreement with Niu et al. (2005) who obtained an exponential function relationship between the fraction of saturated area and water table depth by representing the CDF of topographic wetness index using an exponential function.

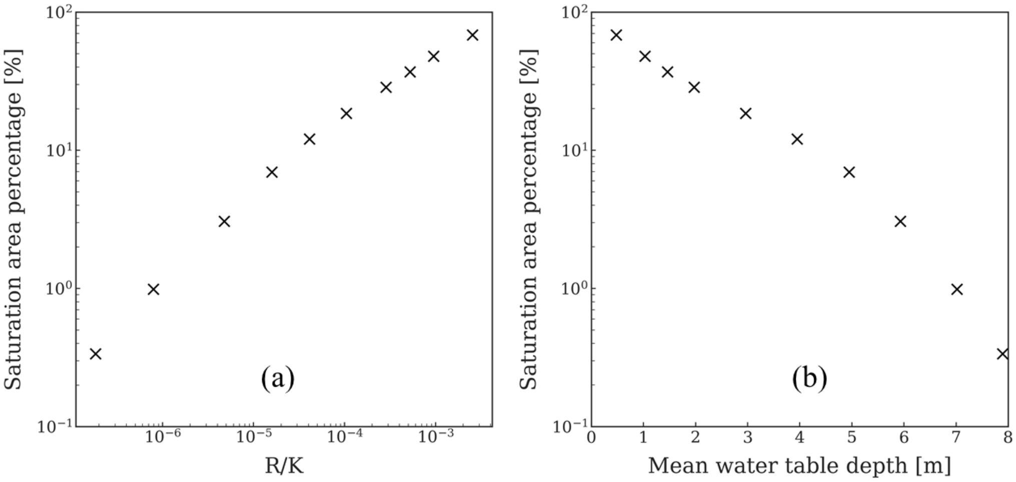

Figure 6.3: (a) The relationship between saturated area percentage and the ratio between recharge and saturated hydraulic conductivity (R/K); (b) the relationship between saturated area percentage and mean water table depth (m).

6.3.3 Statistical Distribution of Water Storage in Different Climates

In this section, we present the spatial distribution of water storage from the statistics perspective. Figure 6.4 presents the empirical CDFs of the groundwater storage under different climates. The black curve is the empirical CDF of the maximum storage capacity which is defined as the total water storage space from land surface to the impeding bedrock surface, and is determined by the soil thickness and soil porosity. It can be found that the empirical CDF of the maximum storage capacity present an “S” shape, which is accordance with previous studies (Gao et al., 2021; Sivapalan et al., 1997). Figure 6.4 shows that the statistical distribution of water storage evolves systematically with climate. The empirical CDF is similar as that of the maximum storage capacity under humid condition with a shallow water table as shown by the purple curves because the shallow water table configuration roughly follows the land surface topography. Whilst the statistical distribution of groundwater storage gradually deviates from the “S” shape as climate becomes more arid and the groundwater storage is more skewered to relatively smaller values. Soil thickness within the modeled area decreases from channel network to uplands; therefore, groundwater storage is limited in uplands and mainly accumulated in downstream when the climate is highly arid (e.g., R/K=1.8e-7), leading to the large percentage of small values and an abrupt change of the slope in the CDF curve (red curve in Figure 6.4).

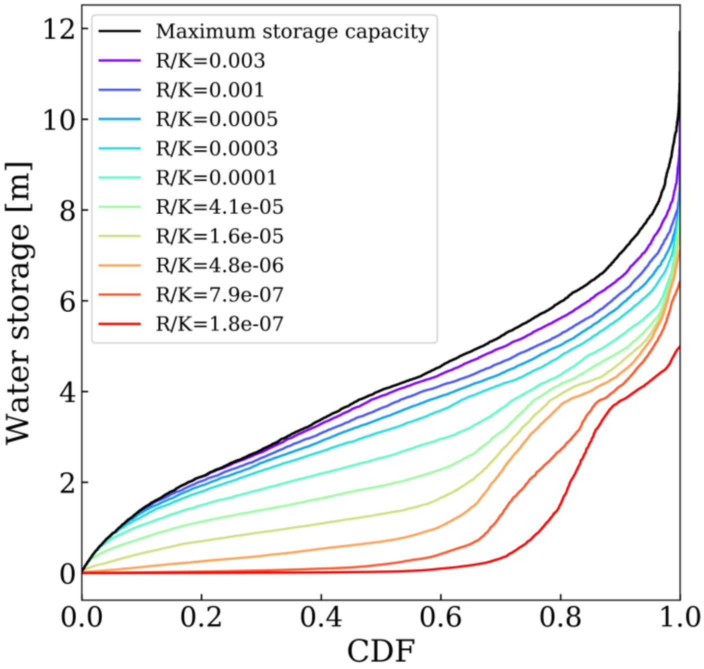

Figure 6.4: The empirical cumulative distribution functions (CDF) of the groundwater storage under different climates represented by the ratio between recharge and saturated hydraulic conductivity (R/K).

6.4 Discussions

6.4.1 Impact of Bedrock Topography

Catchment adapts to the nature of climate forcing, as a result, soil thickness or the topography of impeding bedrock would change with long-term climate (Blöschl et al., 2013; Troch et al., 2015). While the above results and analysis were based on the simulations with a fixed bedrock. To demonstrate that the evolution pattern of the spatially distributed water storage with climate remains valid with various soil thickness or bedrock topographic, a synthetic bedrock was designed, and a new model was built by replacing the observed bedrock with the synthetic bedrock. The synthetic bedrock was generated through utilizing the observed bedrock data combined with channel network on the land surface, and the elevation (E [m]) of the synthetic bedrock at the point scale is determined by the following equation:

$$E = E_0 + s \times d \tag{6.1}$$

where E_0 (m) is the observed bedrock elevation of the closest cell in the highest order (i.e., the 5th-order) channel network; s (-) is the slope of the bedrock between the cell and its closest cell, and is set to 0.002 in this study; d (m) is the horizontal component of the minimum downslope distance to a cell on the channel network, following the flow path. The synthetic bedrock has the same average soil thickness as the observation (10 m) by moving the bedrock surface with a spatially uniform amount in the vertical direction. As shown in Figure 6.5a, the elevation of the synthetic bedrock is higher in the northeast, and lower in the southwest which is similar as its observed counterpart. However, the topography of the synthetic bedrock surface inherits less land surface topographic information compared to the observed one. Moreover, since the slope of land surface is higher than the synthetic bedrock (i.e., 0.002), the soil thickness for the generated bedrock increases from channel to upland, which is opposite of the observed one in this catchment but has been widely observed in other catchments and used in conceptual models (Rempe & Dietrich, 2014; St. Clair et al., 2015; Troch et al., 2002; Zimmer & McGlynn, 2017).

Figure 6.5b presents the statistical distributions of water storage from simulations with the synthetical bedrock. The empirical CDF of the maximum storage capacity (black curve in Figure 6b) also present an “S” shape, and the distribution of water storage shows a similar pattern of evolution with climate as that in the model with the observed bedrock, i.e., deviating from the empirical CDF of the maximum storage capacity as climate becomes more arid. Whereas compared to Figure 6.4, the CDF curve with arid climate is much flatter in Figure 6.5b. It is because the soil thickness increases from channel network to uplands in the model with the synthetical bedrock which is opposite to the observed topography; therefore, the groundwater thickness is more uniformly distributed across the catchment.

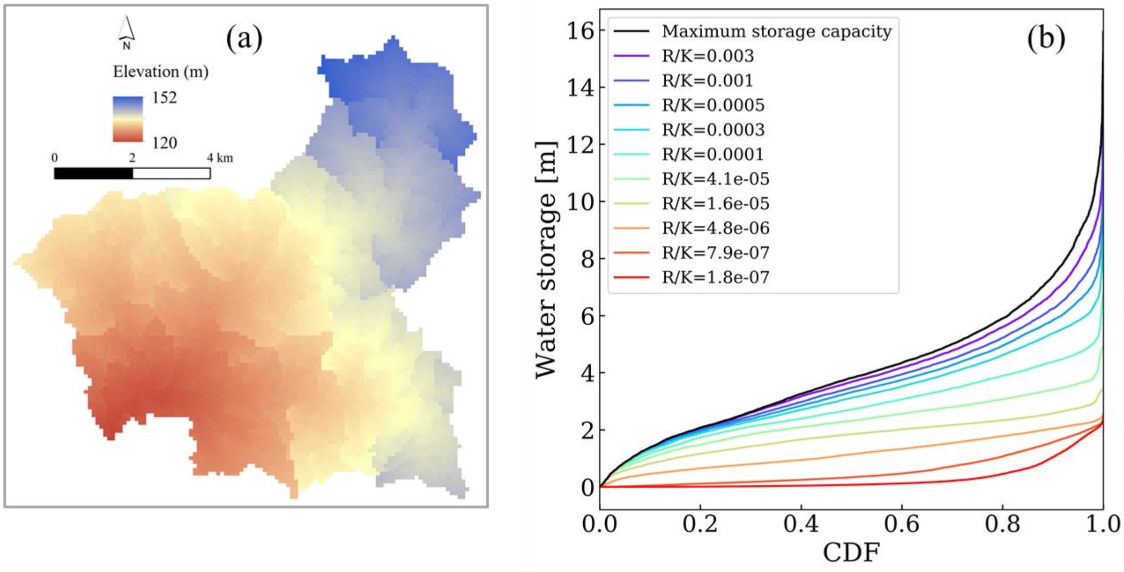

Figure 6.5: (a) The topography of the synthetical bedrock with 100 m resolution, and (b) the empirical cumulative distribution functions (CDF) of groundwater storage under different climates represented by the ratio between recharge and saturated hydraulic conductivity (R/K).

6.4.2 Unifying Saturation Excess Runoff Models

The TOPMODEL and VIC-type model have distinct conceptualizations on rainfall-runoff process. As mentioned in the Introduction section, one of the basic assumptions of TOPMODEL is that water table is parallel to land surface (Beven & Kirkby, 1979; Sivapalan et al., 1987). While the VIC-type model assumes a spatially uniform water storage rise across the catchment as shown in Figure 6a (Liang et al., 1994; Moore, 2007). Figure 6.2 has confirmed that water table in humid climate approximately follows land surface as assumed in the TOPMODEL. The similarity between land surface and water table configuration is also suggested by the similarity between the empirical CDF of the maximum storage capacity (e.g., the black curve in Figure 6.4 or Figure 6.5b) and that of groundwater storage with a shallow water table (e.g., the purple curve in Figure

6.4 or Figure 6.5b). The parallelism between land surface and shallow water table means that the available space for water storage, i.e., spare storage capacity, is spatially uniform across the unsaturated area. Therefore, TOPMODEL implicitly assumes that water storage capacity is approximately spatially uniform across the unsaturated area. As climate becomes arid, larger catchment area holds a similarly small value of water storage indicated by the flatter part of the CDF curve with red color in Figure 6.4 or Figure 6.5b. It is reasonable to speculate that when the climate becomes extremely arid, water storage will become spatially uniform, which is consistent with the water storage assumed in VIC model as shown in Figure 6a. Therefore, the assumption of the spatially uniform water storage rise in the VIC-type model is more reasonable in arid climate.

Inspired by the variation of the probability distribution of water storage (capacity) under different climate conditions, we propose a framework for unifying saturation excess runoff models. In the future investigation, it is possible to have a same functional form to present the spatial distribution of water storage (or water storage capacity) in different climates (or dry and wet seasons in a catchment), and TOPMODEL and the VIC-type model can be viewed as special cases of a more general conceptualization as shown in Figure 6.6b. The colors in the double-headed arrow indicate the transition of the optimal model considering the reasonability degree of their assumptions of the distributed water storage. In this framework, the spatial distribution of water storage could be formulated by a mixed probability distribution function consisting of two parts, one for saturated area and another one for unsaturated area. The spatial distribution of water storage in the saturated area is equal to that of the corresponding maximum storage capacity. The spatial distribution of water storage across the unsaturated area has the same general expression under different climate conditions, but the distribution changes with saturated area ratio (or other variables reflecting the antecedent storage condition). When saturated area ratio approaches 0, the mixed probability distribution function of storage approaches to that used by the VIC-type model; whereas, when saturated area ratio approaches 1, the mixed distribution function becomes the distribution function of the maximum storage capacity as adopted by TOPMODEL.

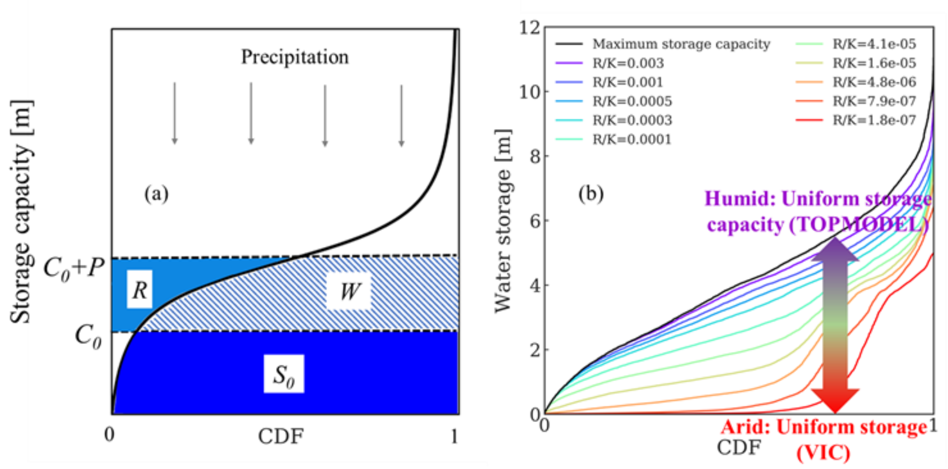

Figure 6.6: (a) The conceptualization of water storage in the VIC-type model: S_0 is the initial soil water storage; P is the precipitation which is partitioned into the soil wetting (W) and runoff (R). (b) Schematic illustrating that the TOPMODEL and VIC-type morels are special cases of a unified framework which conceptualizes distributed water storage through a general functional form. The colors in the double-headed arrow indicate the transition of the optimal model considering the reasonability degree of their assumptions of the distributed water storage.

6.5 Conclusion

The spatial pattern of groundwater table and the corresponding distribution of water storage are recognized as crucial determinants of saturation excess runoff generation at the catchment scale. To investigate the variation of the spatial distribution of water storage in different climates, steady-state water table was obtained from numerical simulations using MODFLOW (USG) for hypothetical models. When water table is close to the land surface in humid climate, land surface is a good proxy of water table; and when the water table is close to the bedrock in arid climate, bedrock is a good proxy of water table. Results showed that the spatial distribution of water storage, quantified through the empirical cumulative distribution function, changes with water table depth systematically, approximately from the state of a spatially uniform storage capacity under wet conditions to the state of a spatially uniform storage in unsaturated area under dry conditions. Moreover, it was found that the percentage of saturated area on the land surface follows an exponential function relationship with mean water table depth or follows a power function relationship with R/K.

This paper provided a framework to unify the TOPMODEL and VIC-type model from the perspective of their underlying assumptions on the probability distribution of water storage. The assumed water table in TOPMODEL suggests an approximately spatially uniform water storage capacity in the unsaturated area; whilst the VIC-type model indicates a spatially uniform water storage in the unsaturated area. Different saturation excess runoff models are possible to be unified by a same general expression for water storage (capacity) distribution which could characterize the full spectrum of the spatial distribution of water storage: spatially uniform storage capacity type, spatially uniform storage type, and the transition between them.

The findings of this study contribute to a better understanding of the spatial distribution of water storage at the catchment scale, representing a further step towards developing process-based hydrological models for modeling the saturation excess runoff generation. However, these findings may be somewhat limited by the modeling sets applied in this study. It assumes homogenous geological properties and recharge in the model area. Further studies, which consider more comprehensive catchment properties, could be undertaken.

CHAPTER SEVEN: CONCLUSION

Hydrological processes including the infiltration, total streamflow generation, baseflow generation, evaporation, were investigated considering the role of groundwater table. For the infiltration process, the assumptions of TCA, i.e., time invariant and uniform initial soil moisture in the vertical directions, were evaluated in the presence of a shallow water table, and were relaxed by introducing a powerful function relationship between the infiltration rate and its time derivate. Numerical simulations in HYDRUS showed that the exponent of the power function of TCA gradually evolves during the infiltration process because of the dynamics of the two driving forces of infiltration, i.e., capillary and gravity. A dimensionless matric named infiltration Péclet number (Pe) was proposed to evaluate the relative effect of gravity and capillarity. When the gravity is dominant, i.e., $Pe>1$, the exponent of the power function of TCA follows a linear relationship with Pe. The relationship between Pe and β provides an objective approach to identify the suitable infiltration function.

A new daily water balance model incorporating the SCS distribution function for describing the spatial variability of soil water storage capacity was developed. In this model, the spatial variability of the soil water storage was assumed to have impacts on both runoff generation and evaporation. This new model unifies water balance models from daily to mean annual timescales. The relative effects of climate variabilities, i.e., intra-monthly, intra-annual, and inter-annual variability of precipitation and potential evapotranspiration, on the streamflow at different timescales were evaluated by comparing the simulated streamflow from different timescale climate scenarios for MOPEX catchments in the U.S. The results show that at the daily, monthly, and annual scales, streamflow variation is mostly influenced by the climate variability at the same timescale.

The mean annual water balance model from the unified framework was used to disentangle the roles of climate and soil water storage capacity on baseflow generation at the mean annual scale for catchments from both the U.S. and U.K. A dimensionless parameter named storage capacity index defined as the ratio between the average storage capacity of a catchment and the mean annual precipitation was found to directly related to the baseflow index and baseflow fraction to the study area. In general, baseflow index or baseflow coefficient increases with storage capacity index given a climate condition, and it decreases with climate aridity index given a storage capacity index. The storage capacity index was found to follow an exponential function with the climate aridity index which indicates further evidence of the coevolution of climate and catchment landscape.

The spatial distribution of available water for evaporation which is determined by the location of groundwater table given a catchment was found to determines the different functional form of Budyko equations based on the on-stage precipitation partitioning concept. The lower bound the Budyko curve was explained by the possible spatial distribution of the available for evaporation as a result of catchment coevolution.

Lastly, the variation of the spatial distribution of groundwater table and the corresponding storage distribution were explored under different climate conditions for a given catchment through numerical simulations. The land surface and bedrock topography were found to serve as the two endmembers of water table configuration at the catchment scale, and the empirical cumulative distribution function of water storage within the catchment evolves systematically as climate becomes more arid from a spatially-uniform-storage-capacity form to the spatially-uniform-storage case form. Storage capacity in humid condition with a shallow water table could be approximated as spatially uniform as assumed in the TOPMODEL, while in arid condition when the groundwater table is close to the bedrock the available storage is spatially uniform as assumed in the VIC-type model. Therefore, the systematic evolution of the statistical distribution of water storage provides a framework for unifying the two popular hydrological models, i.e., the TOPMPODEL and VIC-type model.

Studies in this dissertation contributed to deeper understandings of water balance behaviors considering the presence of groundwater table and its spatial heterogeneity for both the infiltration excess and saturation excess runoff generation regimes. Whereas there is abundant room for further progress. Future work is needed to test the applicability of the power function relationship of TCA at the catchment scale with multiple soil layers and considering the impacts of air phase during infiltration. Process-based methods interpreting hydrological processes in greater detail are also needed in the future to understand baseflow at smaller timescales. The impact of the catchment topography on the spatial distribution of the maximum storage capacity is required to explored. In addition, the general functional form of the spatial distribution of water storage is required to be proposed, and the unified framework in which the TOPMODEL and VIC-type model are the two endmembers is suggested to be evaluated in terms of its performance in modeling hydrological processes.

APPENDIX: PÉCLET NUMBER FOR MUALEM-VAN GENUCHTEN MODEL

The Péclet number is derived here for the case when the Mualem-*van* Genuchten (MG) model is used for describing soil hydraulic properties (Mualem, 1976; van Genuchten, 1980):

$$\theta(\psi) = \theta_r + \frac{\theta_s - \theta_r}{(1+(c|\varphi|)^n)^m} \tag{A1}$$

$$K(\psi) = K_S \frac{\left\{1-(c|\varphi|)^{n-1}[1+(c|\varphi|)^n]^{-m}\right\}^2}{(1+(c|\varphi|)^n)^{m/2}} \tag{A2}$$

$$m = 1 - \frac{1}{n} \tag{A3}$$

where c, n, and m are parameters, and $n > 1$. From Equations (A1) and (A2), one can obtain ψ and K as functions of θ and the following derivatives:

$$\frac{\partial K}{\partial \theta} = \frac{K_S\left[\left(1-S_e{}^{1/m}\right)^m\left(5S_e{}^{1/m}-1\right)-S_e{}^{1/m}+1\right]\cdot\left[\left(1-S_e{}^{1/m}\right)^m-1\right]}{2(\theta_s-\theta_r)S_e{}^{1/2}\left(S_e{}^{1/m}-1\right)} \tag{A4}$$

$$\frac{\partial \psi}{\partial \theta} = \frac{\left(S_e{}^{-1/m}-1\right)^{-m}}{cmn(\theta-\theta_r)S_e{}^{1/m}} \tag{A5}$$

where S_e is effective saturation and defined as:

$$S_e = \frac{\theta-\theta_r}{\theta_s-\theta_r} \tag{A6}$$

From Equation (A1) and (A6), one obtains:

$$S_e{}^{1/m} = [1+(c|\varphi|)^n]^{-1} \tag{A7}$$

Substituting Equations (A4), (A5) and (A7) into Equation (11), the infiltration Péclet number as a function of $|\varphi|$ is obtained:

$$Pe = \frac{\{cmnL[1+(c|\varphi|)^n]^{-1}\}\cdot\left\{[5[1+(c|\varphi|)^n]^{-1}-1]\cdot[1-[1+(c|\varphi|)^n]^{-1}]^m-[1+(c|\varphi|)^n]^{-1}+1\right\}\cdot\{[1+(c|\varphi|)^n]-1\}^m}{2\{[1+(c|\varphi|)^n]^{-1}-1\}\cdot\{\{1-[1+(c|\varphi|)^n]^{-1}\}^m-1\}} \tag{A8}$$

Besides the Brooks-Corey model, numerical simulations were conducted for two soils (clay and sandy loam) based on the Mualem-van Genuchten (MG) model. In general, the findings are consistent with the Brooks-Corey model, e.g., β decreases with Pe. The detailed information is documented in the Supporting Information (SI). The main differences are summarized here. For both clay and sandy loam, β decreases rapidly with Pe when Pe < 0.5. When Pe > 0.5, β is stable, and β is around 1.5 for clay but 1.0 for sandy loam. The mode of the exponents is 1.5 for clay but 1.0 for sandy loam; whereas, the mode for the Brooks-Corey model is around 2 for all soils.

REFERENCES

Abatzoglou, J. T. (2013). Development of gridded surface meteorological data for ecological applications and modelling. *International Journal of Climatology*, *33*(1), 121–131. https://doi.org/10.1002/joc.3413

Abatzoglou, J. T., & Ficklin, D. L. (2017). Climatic and physiographic controls of spatial variability in surface water balance over the contiguous United States using the Budyko relationship. *Water Resources Research*, *53*(9), 7630–7643. https://doi.org/10.1002/2017WR020843

Abbott, M. B., Bathurst, J. C., Cunge, J. A., O'Connell, P. E., & Rasmussen, J. (1986). An introduction to the European Hydrological System — Systeme Hydrologique Europeen, "SHE", 2: Structure of a physically-based, distributed modelling system. *Journal of Hydrology*, *87*(1–2), 61–77. https://doi.org/10.1016/0022-1694(86)90115-0

Allen, R. G., Pereira, L. S., Raes, D., & Smith, M. (1998). Crop evapotranspiration—*Guidelines for computing crop water requirements—FAO Irrigation and drainage paper 56* (Vol. 300, 9th ed., pp. D05109). Rome, Italy: Food and Agriculture Organization.

Appels, W. M., Bogaart, P. W., & van der Zee, S. E. A. T. M. (2017). Feedbacks between shallow groundwater dynamics and surface topography on runoff generation in flat fields. *Water Resources Research*, *53*(10). https://doi.org/10.1002/2017WR020727

Arora, V. K. (2002), The use of the aridity index to assess climate change effect on annual runoff, *Journal of Hydrology*, *265*(1–4), 164–177. https://doi.org/10.1016/S0022-1694(02)00101-4

Assouline, S. (2013). Infiltration into soils: Conceptual approaches and solutions. *Water Resources Research, 49*, 1755–1772. https://doi.org/ 10.1002/wrcr.20155

Assouline, S., Selker, J. S., & Parlange, J. Y. (2007). A simple accurate method to predict time of ponding under variable intensity rainfall. *Water Resources Research, 43,* W03426. https://doi.org/10.1029/2006WR005138

Atkinson, S. E., Woods, R. A., & Sivapalan, M. (2002). Climate and landscape controls on water balance model complexity over changing timescales. *Water Resources Research*, *38*(12). https://doi.org/10.1029/2002WR001487

Aubert, D., Loumagne, C., & Oudin, L. (2003). Sequential assimilation of soil moisture and streamflow data in a conceptual rainfall-runoff model. *Journal of Hydrology*, *280*(1–4), 145–161. https://doi.org/10.1016/S0022-1694(03)00229-4

Bachmair, S., & Weiler, M. (2012). Hillslope characteristics as controls of subsurface flow variability. *Hydrology and Earth System Sciences*, *16*(10), 3699–3715. https://doi.org/10.5194/hess-16-3699-2012

Baker, D. B., Richards, P., Loftus, T. T., & Kramer, J. W. (2004). A new flashiness index: Characteristics and applications to Midwestern rivers and streams. *Journal of the American Water Resources Association*, *40*(2), 503–522. https://doi.org/10.1111/j.1752-1688.2004. tb01046.x

Bartlett, M. S., Parolari, A. J., McDonnell, J. J., & Porporato, A. (2016). Beyond the SCS-CN method: A theoretical framework for spatially lumped rainfall-runoff response. *Water Resources Research*, *52*(6), 4608–4627. https://doi.org/10.1002/2015WR018439

Basha, H. A. (2011). Infiltration models for semi-infinite soil profiles. *Water Resources Research*, *47,* W08516. https://doi.org/10.1029/ 2010WR010253

Beck, H. E., van Dijk, A. I. J. M., Miralles, D. G., de Jeu, R. A. M., Sampurno Bruijnzeel, L. A., McVicar, T. R., & Schellekens, J. (2013). Global patterns in base flow index and recession based on streamflow observations from 3394 catchments. *Water Resources Research*, *49*(12), 7843–7863. https://doi.org/10.1002/2013WR013918

Berghuijs, W. R., Gnann, S. J., & Woods, R. A. (2020). Unanswered questions on the Budyko framework. *Hydrological Processes*, *34*(26), 5699–5703. https://doi.org/10.1002/hyp.13958

Berghuijs, W. R., Hartmann, A., & Woods, R. A. (2016). Streamflow sensitivity to water storage changes across Europe. *Geophysical Research Letters*, *43*, 1980–1987. https://doi.org/10.1002/2016GL067927

Berghuijs, W. R., Sivapalan, M., Woods, R. A., & Savenije, H. H. G. (2014). Patterns of similarity of seasonal water balances: A window into streamflow variability over a range of time scales. *Water Resources Research*, *50*(7), 5638–5661. https://doi.org/10.1002/2014WR015692

Berghuijs, W. R., Woods, R. A., & Hrachowitz, M. (2014). A precipitation shift from snow towards rain leads to a decrease in streamflow. *Nature Climate Change*, *4*(7), 583–586. https://doi.org/10.1038/nclimate2246

Beven, K. J., & Kirkby, M. J. (1979). A physically based, variable contributing area model of basin hydrology. *Hydrological Sciences Journal*, *24*(1), 43–69. https://doi.org/10.1080/02626667909491834

Blackmore, S., Pedretti, D., Mayer, K. U., Smith, L., & Beckie, R. D. (2018). Evaluation of single-and dual-porosity models for reproducing the release of external and internal tracers from heterogeneous waste-rock piles. *Journal of Contaminant Hydrology*, *214*, 65–74. https://doi. org/10.1016/j.jconhyd.2018.05.007

Bloomfield, J. P., Allen, D. J., & Griffiths, K. J. (2009). Examining geological controls on baseflow index (BFI) using regression analysis: An illustration from the Thames Basin, UK. *Journal of Hydrology*, *373*(1–2), 164–176. https://doi.org/10.1016/j.jhydrol.2009.04.025

Blöschl, G., Sivapalan, M., Wagener, T., Viglione, A., & Savenije, H. (2013). *Runoff prediction in ungauged basins: synthesis across processes, places and scales*. Cambridge, U.K.: Cambridge University Press.

Botter, G., Porporato, A., Rodriguez-Iturbe, I., & Rinaldo, A. (2007). Basin-scale soil moisture dynamics and the probabilistic characterization of carrier hydrologic flows: Slow, leaching-prone components of the hydrologic response. *Water Resources Research*, *43*(2), W02417. https://doi.org/10.1029/2006WR005043

Brooks, R. H., & Corey, A. T. (1964). Hydraulic properties of porous media, Hydrology papers, No. 3, Colorado State University, Fort Collins, CO. Brutsaert, W. (2005). *Hydrology: An introduction* (pp. 305–365). Cambridge, New York: Cambridge University Press. https://doi.org/10.1017/CBO9780511808470

Brutsaert, W. (2005). *Hydrology: An introduction* (pp. 305–365). New York: Cambridge University Press.

Brutsaert, W., & Nieber, J. L. (1977). Regionalized drought flow hydrographs from a mature glaciated plateau. W*ater Resources Research*, *13*(3), 637–643. https://doi.org/10.1029/WR013i003p00637

Budyko, M. I. (1958). *The heat balance of the Earth's surface*. Washington, D.C.: U.S. Dep. Of Commer.

Budyko, M. I. (1974). *Climate and life*, 508 pp. New York: Academic Press.

Cardenas, M. B. (2007). Potential contribution of topography-driven regional groundwater flow to fractal stream chemistry: Residence time distribution analysis of Tóth flow. *Geophysical Research Letters*, *34*(5). https://doi.org/10.1029/2006GL029126

Chen, H., Yang, D., Hong, Y., Gourley, J. J., & Zhang, Y. (2013). Hydrological data assimilation with the Ensemble Square-Root-Filter: Use of streamflow observations to update model states for real-time flash flood forecasting. *Advances in Water Resources, 59*, 209–220.

Chen, X., & Sivapalan, M. (2020). Hydrological Basis of the Budyko Curve: Data-Guided Exploration of the Mediating Role of Soil Moisture. *Water Resources Research*, *56*(10), e2020WR028221. https://doi.org/10.1029/2020WR028221

Chen, X., Alimohammadi, N., & Wang, D. (2013). Modeling interannual variability of seasonal evaporation and storage change based on the extended Budyko framework. *Water Resources Research, 49*(9), 6067–6078. https://doi.org/10.1002/wrcr.20493

Choudhury, B. J. (1999). Evaluation of an empirical equation for annual evaporation using field observations and results from a biophysical model. *Journal of Hydrology*, *216*(1–2), 99–110. https://doi.org/10.1016/S0022-1694(98)00293-5

Clark, D. B., & Gedney, N. (2008). Representing the effects of subgrid variability of soil moisture on runoff generation in a land surface model. *Journal of Geophysical Research*, *113*(D10), D10111. https://doi.org/10.1029/2007JD008940

Clauset, A., Shalizi, C. R., & Newman, M. E. (2009). Power-law distributions in empirical data. *SIAM Review*, *51*(4), 661–703. https://doi.org/ 10.1137/070710111

Condon, L. E., & Maxwell, R. M. (2015). Evaluating the relationship between topography and groundwater using outputs from a continental-scale integrated hydrology model. *Water Resources Research*, *51*(8), 6602–6621. https://doi.org/10.1002/2014WR016774

Condon, L. E., Atchley, A. L., & Maxwell, R. M. (2020). Evapotranspiration depletes groundwater under warming over the contiguous United States. *Nature Communications*, *11*(1), 873. https://doi.org/10.1038/s41467-020-14688-0

Condon, L. E., Markovich, K. H., Kelleher, C. A., McDonnell, J. J., Ferguson, G., & McIntosh, J. C. (2020). Where Is the Bottom of a Watershed? *Water Resources Research*, *56*(3), e2019WR026010. https://doi.org/10.1029/2019WR026010

Cote, C. M., Bristow, K. L., Charlesworth, P. B., Cook, F. J., & Thorburn, P. J. (2003). Analysis of soil wetting and solute transport in subsurface trickle irrigation. *Irrigation Science,* *22*(3–4), 143–156. https://doi.org/10.1007/s00271-003-0080-8

Dabach, S., Lazarovitch, N., Šimůnek, J., & Shani, U. (2013). Numerical investigation of irrigation scheduling based on soil water status. *Irrigation Science*, *31*(1), 27–36. https://doi.org/10.1007/s00271-011-0289-x

Dai, A. (2008). Temperature and pressure dependence of the rain-snow phase transition over land and ocean. *Geophysical Research Letters*, *35*(12), L12802. https://doi.org/10.1029/2008GL033295

Dai, A. (2008). Temperature and pressure dependence of the rain-snow phase transition over land and ocean. *Geophysical Research Letters, 35,* L12802. https://doi.org/10.1029/2008GL033295

de Boer-Euser, T., McMillan, H. K., Hrachowitz, M., Winsemius, H. C., & Savenije, H. H. G. (2016). Influence of soil and climate on root zone storage capacity. *Water Resources*

Research, *52*(3), 2009–2024. https://doi.org/10.1002/2015WR018115

Deng, C., Liu, P., Wang, D., & Wang, W. (2018). Temporal variation and scaling of parameters for a monthly hydrologic model. *Journal of Hydrology*, *558*, 290–300. https://doi.org/10.1016/j.jhydrol.2018.01.049

Deng, C., Liu, P., Wang, D., & Wang, W. (2018). Temporal variation and scaling of parameters for a monthly hydrologic model. *Journal of Hydrology*, *558*, 290–300. https://doi.org/10.1016/j.jhydrol.2018.01.049

Denmark Hydrology Institute (DHI), 2017. Mike She User Manual and Reference Guide, December 2007, Denmark.

Desbarats, A. J., Logan, C. E., Hinton, M. J., & Sharpe, D. R. (2002). On the kriging of water table elevations using collateral information from a digital elevation model. *Journal of Hydrology*, *255*(1–4), 25–38. https://doi.org/10.1016/S0022-1694(01)00504-2

Dettinger, M. D., & Diaz, H. F. (2000). Global characteristics of stream flow seasonality and variability. *Journal of Hydrometeorology*, *1*(4), 289–310. https://doi.org/10.1175/1525-7541(2000)001<0289:GCOSFS>2.0.CO;2

Detty, J. M., & McGuire, K. J. (2010). Topographic controls on shallow groundwater dynamics: implications of hydrologic connectivity between hillslopes and riparian zones in a till mantled catchment. *Hydrological Processes*, *24*(16), 2222–2236. https://doi.org/10.1002/hyp.7656

Detwiler, R. L., Rajaram, H., & Glass, R. J. (2000). Solute transport in variable-aperture fractures: An investigation of the relative importance of Taylor dispersion and macrodispersion. *Water Resources Research*, *36*(7), 1611–1625. https://doi.org/10.1029/2000WR900036

Devia, G. K., B. P. Ganasri, and G. S. Dwarakish (2015), A review on hydrological models, *Aquatic Procedia*, *4*, 1001–1007. https://doi.org/10.1016/j.aqpro.2015.02.126

Diskin, M. H., & Nazimov, N. (1996). Ponding time and infiltration capacity variation during steady rainfall. *Journal of Hydrology*, *178*(1–4), 369–380. https://doi.org/10.1016/0022-1694(95)02798-X

Donohue, R. J., Roderick, M. L., & McVicar, T. R. (2007). On the importance of including vegetation dynamics in Budyko's hydrological model. *Hydrology and Earth System Sciences*, *11*(2), 983–995. https://doi.org/10.5194/hess-11-983-2007

Duan, Q., Schaake, J., Andréassian, V., Franks, S., Goteti, G., Gupta, H. V., et al. (2006). Model Parameter Estimation Experiment (MOPEX): An overview of science strategy and major results from the second and third workshops. *Journal of Hydrology*, *320*(1–2), 3–17. https://doi.org/10.1016/j.jhydrol.2005.07.031

Duan, Q., Sorooshian, S., & Gupta, V. (1992). Effective and efficient global optimization for conceptual rainfall-runoff models. *Water Resources Research*, *28*(4), 1015–1031. https://doi.org/10.1029/91WR02985

Eagleson, P. (1978). Climate, soil, and vegetation 2. The distribution of annual precipitation derived from observed storm sequences. *Water Resources Research*, *14*(5), 713–721. https://doi.org/10.1029/WR014i005p00713

Ehret, U., Gupta, H. V., Sivapalan, M., Weijs, S. V., Schymanski, S. J., Blöschl, G., et al. (2014). Advancing catchment hydrology to deal with predictions under change. *Hydrology and Earth System Sciences*, *18*(2), 649–671. https://doi.org/10.5194/hess-18-649-2014

Entekhabi, D., & Eagleson, P. S. (1989). Land Surface Hydrology Parameterization for Atmospheric General Circulation Models Including Subgrid Scale Spatial Variability.

Journal of Climate, *2*(8), 816–831. https://doi.org/10.1175/1520-0442(1989)002%3C0816:LSHPFA%3E2.0.CO;2

Famiglietti, J. S., & Wood, E. F. (1994). Multiscale modeling of spatially variable water and energy balance processes. *Water Resources Research*, *30*(11), 3061–3078. https://doi.org/10.1029/94WR01498

Famiglietti, J. S., Devereaux, J. A., Laymon, C. A., Tsegaye, T., Houser, P. R., Jackson, T. J., et al. (1999). Ground-based investigation of soil moisture variability within remote sensing footprints During the Southern Great Plains 1997 (SGP97) Hydrology Experiment. *Water Resources Research*, *35*(6), 1839–1851. https://doi.org/10.1029/1999WR900047

Fan, Y., Miguez-Macho, G., Jobbágy, E. G., Jackson, R. B., & Otero-Casal, C. (2017). Hydrologic regulation of plant rooting depth. *Proceedings of the National Academy of Sciences*, *114*(40), 10572–10577. https://doi.org/10.1073/pnas.1712381114

Fan, Y., Miguez-Macho, G., Weaver, C. P., Walko, R., & Robock, A. (2007). Incorporating water table dynamics in climate modeling: 1.Water table observations and equilibrium water table simulations. *Journal of Geophysical Research, 112,* D10125. https://doi.org/10.1029/2006JD008111

Farmer, D., Sivapalan, M., & Jothityangkoon, C. (2003). Climate, soil, and vegetation controls upon the variability of water balance in temperate and semiarid landscapes: Downward approach to water balance analysis. *Water Resources Research*, *39*(2), 1035. https://doi.org/10.1029/2001WR000328

Fatichi, S., Vivoni, E. R., Ogden, F. L., Ivanov, V. Y., Mirus, B., Gochis, D., et al. (2016). An overview of current applications, challenges, and future trends in distributed process-based models in hydrology. *Journal of Hydrology*, *537*, 45–60.

https://doi.org/10.1016/j.jhydrol.2016.03.026

Feng, X., Vico, G., & Porporato, A. (2012). On the effects of seasonality on soil water balance and plant growth. *Water Resources Research, 48,* W05543. https://doi.org/10.1029/2011WR011263

Fenicia, F., Savenije, H. H. G., Matgen, P., & Pfister, L. (2006). Is the groundwater reservoir linear? Learning from data in hydrological modelling. *Hydrology and Earth System Sciences*, *10*, 139–150.

Ferguson, I. M., & Maxwell, R. M. (2010). Role of groundwater in watershed response and land surface feedbacks under climate change. *Water Resources Research*, *46*, W00F02. https://doi.org/10.1029/2009WR008616

Fernandes, N. F., & Dietrich, W. E. (1997). Hillslope evolution by diffusive processes: The timescale for equilibrium adjustments. *Water Resources Research, 33*(6), 1307–1318. https://doi.org/10.1029/97WR00534

Ficklin, D. L., Robeson, S. M., & Knouft, J. H. (2016). Impacts of recent climate change on trends in baseflow and stormflow in United States watersheds. *Geophysical Research Letters*, *43*(10), 5079–5088. https://doi.org/10.1002/2016GL069121

Freer, J., McDonnell, J. J., Beven, K. J., Peters, N. E., Burns, D. A., Hooper, R. P., et al. (2002). The role of bedrock topography on subsurface storm flow. *Water Resources Research*, *38*(12), 1269. https://doi.org/10.1029/2001WR000872

Freer, J., McDonnell, J. J., Beven, K. J., Peters, N. E., Burns, D. A., Hooper, R. P., et al. (2002). The role of bedrock topography on subsurface storm flow. *Water Resources Research*, *38*(12), 5-1-5–16. https://doi.org/10.1029/2001WR000872

Freeze, R. A., & Cherry, J. A. (1979). *Groundwater*. Englewood Cliffs, NJ: Prentice Hall.

Fu, B. P. (1981). On the calculation of the evaporation from land surface [in Chinese]. *Chinese Journal of Atmospheric Sciences, 5*, 23–31. https://doi.org/10.3878/j.issn.10069895.1981.01.03

Gao, H., Birkel, C., Hrachowitz, M., Tetzlaff, D., Soulsby, C., & Savenije, H. H. G. (2019). A simple topography-driven and calibration-free runoff generation module. *Hydrology and Earth System Sciences*, *23*(2), 787–809. https://doi.org/10.5194/hess-23-787-2019

Gao, H., Hrachowitz, M., Schymanski, S. J., Fenicia, F., Sriwongsitanon, N., & Savenije, H. H. G. (2014). Climate controls how ecosystems size the root zone storage capacity at catchment scale. *Geophysical Research Letters*, *41*, 7916–7923. https://doi.org/10.1002/2014GL061668

Gao, Y., Yao, L., Chang, N.-B., & Wang, D. (2021). Diagnosis toward predicting mean annual runoff in ungauged basins. *Hydrology and Earth System Sciences*, *25*(2), 945–956. https://doi.org/10.5194/hess-25-945-2021.

Gao, Y., Yao, L., Chang, N.-B., & Wang, D. (2021). Diagnosis toward predicting mean annual runoff in ungauged basins. https://doi.org/10.5194/hess-2020-353

Gentine, P., D’Odorico, P., Lintner, B. R., Sivandran, G., & Salvucci, G. (2012). Interdependence of climate, soil, and vegetation as constrained by the Budyko curve. *Geophysical Research Letters*, *39*(19), L19404. https://doi.org/10.1029/2012GL053492

Gerrits, A. M. J., Savenije, H. H. G., Veling, E. J. M., & Pfister, L. (2009). Analytical derivation of the Budyko curve based on rainfall characteristics and a simple evaporation model. *Water Resources Research*, *45*(4), W04403. https://doi.org/10.1029/2008WR007308

Ghosh, D. K., Wang, D., & Zhu, T. (2016). On the transition of base flow recession from early stage to late stage. *Advances in Water Resources, 88*, 8–13. https://doi.org/10.1016/j.advwatres.2015.11.015

Gleeson, T., & Manning, A. H. (2008). Regional groundwater flow in mountainous terrain: Three-dimensional simulations of topographic and hydrogeologic controls. *Water Resources Research*, *44*, W10403. https://doi.org/10.1029/2008WR006848

Gnann, S. J., Howden, N. J. K., & Woods, R. A. (2019). Hydrological signatures describing the translation of climate seasonality into streamflow seasonality. *Hydrology and Earth System Sciences, 24*(2), 561–580. https://doi.org/10.5194/hess-24-561-2020

Gnann, S. J., Woods, R. A., & Howden, N. J. K. (2019). Is there a baseflow Budyko curve? *Water Resources Research*, *55*(4), 2838–2855. https://doi.org/10.1029/2018WR024464

Goderniaux, P., Davy, P., Bresciani, E., de Dreuzy, J.-R., & Borgne, T. L. (2013). Partitioning a regional groundwater flow system into shallow local and deep regional flow compartments. *Water Resources Research*, *49*, 2274–2286. https://doi.org/10.1002/wrcr.20186

Gomez-Velez, J. D., Harvey, J. W., Cardenas, M. B., & Kiel, B. (2015). Denitrification in the Mississippi River network controlled by flow through river bedforms. *Nature Geoscience*, *8*(12), 941–945. https://doi.org/10.1038/ngeo2567

Grayson, R., & Western, A. (2001). Terrain and the distribution of soil moisture. *Hydrological Processes*, *15*(13), 2689–2690. https://doi.org/10.1002/hyp.479

Green, W. H., & Ampt, G. A. (1911). Studies on soil physics. *The Journal of Agricultural Science, 4*(01), 1–24. https://doi.org/10.1017/ S0021859600001441

Greve, P., Gudmundsson, L., Orlowsky, B., & Seneviratne, S. I. (2015). Introducing a probabilistic Budyko framework. *Geophysical Research Letters*, *42*(7), 2261–2269. https://doi.org/10.1002/2015GL063449

Gupta, H. V., Kling, H., Yilmaz, K. K., & Martinez, G. F. (2009). Decomposition of the mean squared error and NSE performance criteria: Implications for improving hydrological modelling. *Journal of Hydrology, 377*(1-2), 80–91. https://doi.org/10.1016/j.jhydrol.2009.08.003

Haberlandt, U., KloÈcking, B., Krysanova, V., & Becker, A. (2001). Regionalisation of the baseflow index from dynamically simulated flow components - a case study in the Elbe River Basin. *Journal of Hydrology*, *248*(1–4), 35–53.

Haitjema, H. M., & Mitchell-Bruker, S. (2005). Are Water Tables a Subdued Replica of the Topography? *Ground Water*, *43*(6), 781–786. https://doi.org/10.1111/j.1745-6584.2005.00090.x

Han, P. F., Wang, X. S., & Istanbulluoglu, E. (2018). A null-parameter formula of storage-evapotranspiration relationship at catchment scale and its application for a new hydrological model. *Journal of Geophysical Research: Atmospheres, 123,* 2082–2097. https://doi.org/ 10.1002/2017jd027758

Hare, D. K., Helton, A. M., Johnson, Z. C., Lane, J. W., & Briggs, M. A. (2021). Continental-scale analysis of shallow and deep groundwater contributions to streams. *Nature Communications*, *12*, 1450. https://doi.org/10.1038/s41467-021-21651-0

Harman, C., & Troch, P. A. (2014). What makes Darwinian hydrology “Darwinian”? Asking a different kind of question about landscapes. *Hydrology and Earth System Sciences*, *18*(2), 417–433. https://doi.org/10.5194/hess-18-417-2014

Harrigan, S., Hannaford, J., Muchan, K., & Marsh, T. J. (2018). Designation and trend analysis of the updated UK Benchmark Network of river flow stations: the UKBN2 dataset. *Hydrology Research*, *49*(2), 552–567. https://doi.org/10.2166/nh.2017.058

Hay, L. E., Leavesley, G. H., Clark, M. P., Markstrom, S. L., Viger, R. J., & Umemoto, M. (2006). Step wise, multiple objective calibration of a hydrologic model for a snowmelt dominated basin. *Journal of the American Water Resources Association, 42*, 877–890. https://doi.org/ 10.1111/j.1752-1688.2006.tb04501.x

Hickel, K., & Zhang, L. (2006). Estimating the impact of rainfall seasonality on mean annual water balance using a top-down approach. *Journal of Hydrology, 331*(3–4), 409–424. https://doi.org/10.1016/j.jhydrol.2006.05.028

Holtan, H. N. (1945). Time-condensation in hydrograph-analysis. Eos, *Transactions of the American Geophysical Union, 26*(3), 407–413. https://doi.org/10.1029/TR026i003p00407

Hooshyar, M., & Wang, D. (2016). An analytical solution of Richards' equation providing the physical basis of SCS curve number method and its proportionality relationship. *Water Resources Research*, *52*(8), 6611–6620. https://doi.org/10.1002/2016WR018885

Horton, R. E. (1940). An approach towards a physical interpretation of infiltration capacity. *Soil Science Society of America Journa*l, *5*(c), 399–417.

Houska, T., Kraft, P., Chamorro-Chavez, A., & Breuer, L. (2015). SPOTting model parameters using a ready-made python package. *PLoS ONE*, *10*(12), e0145180. https://doi.org/10.1371/journal.pone.0145180

Huang, M., Liang, X., & Liang, Y. (2003). A transferability study of model parameters for the variable infiltration capacity land surface scheme. *Journal of Geophysical Research: Atmospheres*, *108*(D22), 2003JD003676. https://doi.org/10.1029/2003JD003676

Hutchinson, D. G., & Moore, R. D. (2000). Throughflow variability on a forested hillslope underlain by compacted glacial till. *Hydrological Processes*, *14*, 1751–1766.

Huysmans, M., & Dassargues, A. (2005). Review of the use of Péclet numbers to determine the relative importance of advection and diffusion in low permeability environments. *Hydrogeology Journal*, *13*(5–6), 895–904. https://doi.org/10.1007/s10040-004-0387-4

Istanbulluoglu, E., Wang, T., Wright, O. M., & Lenters, J. D. (2012). Interpretation of hydrologic trends from a water balance perspective: The role of groundwater storage in the Budyko hypothesis. *Water Resources Research, 48,* W00H16. https://doi.org/10.1029/ 2010WR010100

Jasechko, S., Birks, S. J., Gleeson, T., Wada, Y., Fawcett, P. J., Sharp, Z. D., et al. (2014). The pronounced seasonality of global groundwater recharge. *Water Resources Research, 50,* 8845–8867. https://doi.org/10.1002/2014WR015809

Jayawardena, A. W., & Zhou, M. C. (2000). A modified spatial soil moisture storage capacity distribution curve for the Xinanjiang model. *Journal of Hydrology*, *227*(1-4), 93–113. https://doi.org/10.1016/S0022-1694(99)00173-0

Jiang, X.-W., Wan, L., Cardenas, M. B., Ge, S., & Wang, X.-S. (2010). Simultaneous rejuvenation and aging of groundwater in basins due to depth-decaying hydraulic conductivity and porosity. *Geophysical Research Letters*, *37*(5), L05403. https://doi.org/10.1029/2010GL042387

Jordan, T. E., Correll, D. L., & Weller, D. E. (1997). Relating nutrient discharges from watersheds to land use and streamflow variability. *Water Resources Research*, *33*(11), 2579–2590. https://doi.org/10.1029/97WR02005

Jothityangkoon, C., & Sivapalan, M. (2009). Framework for exploration of climatic and landscape controls on catchment water balance, with emphasis on inter-annual variability. *Journal of Hydrology*, *371*(1–4), 154–168. https://doi.org/10.1016/j.jhydrol.2009.03.030

Jothityangkoon, C., Sivapalan, M., & Farmer, D. L. (2001). Process controls of water balance variability in a large semi-arid catchment: downward approach to hydrological model development. *Journal of Hydrology*, *254*(1–4), 174–198. https://doi.org/10.1016/S0022-1694(01)00496-6

Kavetski, D., Kuczera, G., & Franks, S. W. (2003). Semidistributed hydrological modeling: A "saturation path" perspective on TOPMODEL and VIC. *Water Resources Research*, *39*(9). https://doi.org/10.1029/2003WR002122

Kim, C. P., Stricker, J. N. M., & Torfs, P. J. J. F. (1996). An analytical framework for the water budget of the unsaturated zone. *Water Resources Research*, *32*(12), 3475–3484. https://doi.org/10.1029/95WR02667

Kim, K. B., Kwon, H. H., & Han, D. (2018). Exploration of warm-up period in conceptual hydrological modelling. *Journal of Hydrology, 556*, 194–210. https://doi.org/10.1016/j.jhydrol.2017.11.015

Kollat, J. B., Reed, P. M., & Wagener, T. (2012). When are multiobjective calibration trade-offs in hydrologic models meaningful? *Water Resources Research*, *48,* W03520. https://doi.org/10.1029/2011WR011534

Kollat, J. B., Reed, P. M., & Wagener, T. (2012). When are multiobjective calibration trade-offs in hydrologic models meaningful? *Water Resources Research*, *48*(3), W03520. https://doi.org/10.1029/2011WR011534

Konapala, G., Kao, S., & Addor, N. (2020). Exploring Hydrologic Model Process Connectivity at the Continental Scale Through an Information Theory Approach. *Water Resources Research*, *56*(10). https://doi.org/10.1029/2020WR027340

Koster, R. D., & Suarez, M. J. (1999). A simple framework for examining the interannual variability of land surface moisture fluxes. *Journal of Climate*, *12*(7), 1911–1917. https://doi.org/10.1175/1520-0442(1999)012<1911:ASFFET>2.0.CO;2

Lacey, G. C., & Grayson, R. B. (1998). Relating baseflow to catchment properties in south-eastern Australia. *Journal of Hydrology*, *204*(1–4), 231–250. https://doi.org/10.1016/S0022-1694(97)00124-8

Lane, R. A., Coxon, G., Freer, J. E., Wagener, T., Johnes, P. J., Greene, S., et al. (2019). Benchmarking the predictive capability of hydrological models for river flow and flood peak predictions across a large-sample of catchments in Great Britain, 34.

Li, D. (2014). Assessing the impact of interannual variability of precipitation and potential evaporation on evapotranspiration. *Advances in Water Resources*, *70*, 1–11. https://doi.org/10.1016/j.advwatres.2014.04.012

Li, D., Pan, M., Cong, Z., Zhang, L., & Wood, E. (2013). Vegetation control on water and energy balance within the Budyko framework. *Water Resources Research*, *49*, 969–976. https://doi.org/10.1002/wrcr.20107

Li, H., Sivapalan, M., Tian, F., & Harman, C. (2014). Functional approach to exploring climatic and landscape controls of runoff generation: 1. Behavioral constraints on runoff volume. *Water Resources Research*, *50*(12), 9300–9322. https://doi.org/10.1002/2014WR016307

Liang, X., Lettenmaier, D. P., Wood, E. F., & Burges, S. J. (1994). A simple hydrologically based model of land surface water and energy fluxes for general circulation models.

Journal of Geophysical Research, *99*(D7), 14,415–14,428. https://doi.org/10.1029/94JD00483

Liang, X., Lettenmaier, D. P., Wood, E. F., & Burges, S. J. (1994). A simple hydrologically based model of land surface water and energy fluxes for general circulation models. *Journal of Geophysical Research: Atmospheres*, *99*(D7), 14415–14428.

Liang, X., Lettenmaier, D. P., Wood, E. F., & Burges, S. J. (1994). A simple hydrologically based model of land surface water and energy fluxes for general circulation models. *Journal of Geophysical Research: Atmospheres*, *99*(D7), 14415–14428.

Liang, X., Xie, Z., & Huang, M. (2003). A new parameterization for surface and groundwater interactions and its impact on water budgets with the variable infiltration capacity (VIC) land surface model. *Journal of Geophysical Research*, *108*(D16), 8613. https://doi.org/10.1029/2002JD003090

Liu, M. C., Parlange, J. Y., Sivapalan, M., & Brutsaert, W. (1998). A note on the time compression approximation. *Water Resources Research*, *34*(12), 3683–3686. https://doi.org/10.1029/98WR02741

Liu, Y. B., & Smedt, F. D. (2004). *WetSpa Extension, A GIS-based Hydrologic Model for Flood Prediction and Watershed Management*. Department of Hydrology and Hydraulic Engineering, Vrije Universiteit Brussel, Belgium.

Longobardi, A., & Villani, P. (2008). Baseflow index regionalization analysis in a mediterranean area and data scarcity context: Role of the catchment permeability index. *Journal of Hydrology*, *355*(1–4), 63–75. https://doi.org/10.1016/j.jhydrol.2008.03.011

Lute, A. C., & Abatzoglou, J. T. (2014). Role of extreme snowfall events in interannual variability of snowfall accumulation in the western United States. *Water Resources Research, 50,* 2874–2888. https://doi.org/10.1002/2013WR014465

L'vovich, M. I. (1979). *World water resources and their future*. Washington: American Geophysical Union. https://doi.org/10.1029/SP013

Lyne, V., & Hollick, M. (1979). *Stochastic time-variable rainfall-runoff modelling*. In Presented at the Institute of Engineers Australia National Conference (pp. 89–93), Perth: Institute of Engineers Australia.

Maidment, D. R. (1993). *Handbook of hydrology*. New York: McGraw-Hill.

Maidment, D. R.: ArcHydro: GIS for Water Resources, ESRI Press, Redlands, CL, USA, 2002.

Makhlouf, Z., & Michel, C. (1994). A two-parameter monthly water balance model for French watersheds. *Journal of Hydrology, 162*(3-4), 299–318. https://doi.org/10.1016/0022-1694(94)90233-X

Maxwell, R. M., & Condon, L. E. (2016). Connections between groundwater flow and transpiration partitioning. *Science*, *353*(6297), 377–380. https://doi.org/10.1126/science.aaf7891

McGuire, K. J., McDonnell, J. J., Weiler, M., Kendall, C., McGlynn, B. L., Welker, J. M., & Seibert, J. (2005). The role of topography on catchment-scale water residence time. *Water Resources Research*, *41*(5). https://doi.org/10.1029/2004WR003657

McIntyre, N., Lee, H., Wheater, H., Young, A., & Wagener, T. (2005). Ensemble predictions of runoff in ungauged catchments. *Water Resources Research, 41,* W12434. https://doi.org/10.1029/2005WR004289

McMillan, H. K., & Srinivasan, M. (2015). Characteristics and controls of variability in soil moisture and groundwater in a headwater catchment. *Hydrology and Earth System Sciences*, *19*(4), 1767–1786. https://doi.org/10.5194/hess-19-1767-2015

McNamara, J. P., Tetzlaff, D., Bishop, K., Soulsby, C., Seyfried, M., Peters, N. E., et al. (2011). Storage as a metric of catchment comparison. *Hydrological Procedure*, *25*(21), 3364–3371. https://doi.org/10.1002/hyp.8113

Mein, R. G., & Larson, C. L. (1973). Modeling infiltration during a steady rain. *Water Resources Research*, *9*(2), 384–394. https://doi.org/10.1029/WR009i002p00384

Meira Neto, A. A., Roy, T., Oliveira, P. T. S., & Troch, P. A. (2020). An aridity index-based formulation of streamflow components. *Water Resources Research*, *56*(9). https://doi.org/10.1029/2020WR027123

Mezentsev, V. S. (1955). More on the calculation of average total evaporation. *Meteorol. Gidrol*, *5*(24–28).

Micallef, A., Person, M., Haroon, A., Weymer, B. A., Jegen, M., Schwalenberg, K., et al. (2020). 3D characterisation and quantification of an offshore freshened groundwater system in the Canterbury Bight. *Nature Communications*, *11*(1), 1372. https://doi.org/10.1038/s41467-020-14770-7

Miller, M. P., Buto, S. G., Susong, D. D., & Rumsey, C. A. (2016). The importance of base flow in sustaining surface water flow in the Upper Colorado River Basin. *Water Resources Research*, *52*(5), 3547–3562. https://doi.org/10.1002/2015WR017963

Milly, P. C. D. (1986). An event-based simulation model of moisture and energy fluxes at a bare soil surface. *Water Resources Research*, *22*(12),1680–1692. https://doi.org/10.1029/WR022i012p01680

Milly, P. C. D. (1994). Climate, soil water storage, and the average annual water balance. *Water Resources Research, 30*(7), 2143–2156. https://doi.org/10.1029/94WR00586

Milly, P. C. D., & Dunne, K. A. (2002). Macroscale water fluxes 2. Water and energy supply control of their interannual variability. *Water Resources Research, 38*(10). 157 https://doi.org/10.1029/2001WR000760

Mishra, S. K., Tyagi, J. V., & Singh, V. P. (2003). Comparison of infiltration models. *Hydrological Processes*, *17*(13), 2629–2652. https://doi.org/10.1002/hyp.1257

Monteith, J. L. (1965). Evaporation and environment. The state and movement of water in living organisms. In *Symposia of the Society for Experimental Biology* (Vol. 19, pp. 205–234). Cambridge, UK: Cambridge University Press.

Moore, R. J. (1985). The probability-distributed principle and runoff production at point and basin scales. *Hydrological Sciences Journal*, *30*(2), 273–297. https://doi.org/10.1080/02626668509490989

Moore, R. J. (2007). The PDM rainfall-runoff model. *Hydrology and Earth System Sciences*, *11*(1), 483–499. https://doi.org/10.5194/hess-11-483-2007

Moore, R. J. (2007). The PDM rainfall-runoff model. Hydrology and Earth System Sciences, 11(1), 483–499. https://hal.archives-ouvertes.fr/hal-00305633/

Moriasi, D. N., Arnold, J. G., Van Liew, M. W., Bingner, R. L., Harmel, R. D., & Veith, T. L. (2007). Model evaluation guidelines for systematic quantification of accuracy in watershed simulations. *Transactions of the ASABE, 50*(3), 885–900. https://doi.org/10.13031/2013.23153

Mualem, Y. (1976). A new model for predicting the hydraulic conductivity of unsaturated porous media. *Water Resources Research*, *12*(3),513–522. https://doi.org/10.1029/WR012i003p00513

Mwakalila, S., Feyen, J., & Wyseure, G. (2002). The influence of physical catchment properties on baseflow in semi-arid environments. *Journal of Arid Environments*, *52*(2), 245–258. https://doi.org/10.1006/jare.2001.0947

Nash, J. E., & Sutcliffe, J. V. (1970). River flow forecasting through conceptual models part I—A discussion of principles. *Journal of Hydrology*, *10*(3), 282–290. https://doi.org/10.1016/0022-1694(70)90255-6

National Resources Conservation Service (2004). Hydrology. In *National engineering handbook* (Chap. 10, pp. 10-2-10-4). Washington, DC: National Resources Conservation Service, US Department of Agriculture.

Niu, G.-Y., Yang, Z.-L., Dickinson, R. E., & Gulden, L. E. (2005). A simple TOPMODEL-based runoff parameterization (SIMTOP) for use in global climate models. *Journal of Geophysical Research*, *110*, D21106. https://doi.org/10.1029/2005JD006111

Noto, L. V. (2014). Exploiting the Topographic Information in a PDM-Based Conceptual Hydrological Model. *Journal of Hydrologic Engineering*, *19*(6), 13.

Ol'dekop, E. M. (1911). On evaporation from the surface of river basins. *Meteorol. Obs. Univ. Tartu*, *4*, 200.

Padrón, R. S., Gudmundsson, L., Greve, P., & Seneviratne, S. I. (2017). Large-Scale Controls of the Surface Water Balance Over Land: Insights From a Systematic Review and Meta-Analysis. *Water Resources Research*, *53*(11), 9659–9678. https://doi.org/10.1002/2017WR021215

Panday, S., Langevin, C. D., Niswonger, R. G., Ibaraki, M., & Hughes, J. D. (2013). *MODFLOW–USG version 1: An unstructured grid version of MODFLOW for simulating groundwater flow and tightly coupled processes using a control volume finite-difference formulation* (book 6 A45). U.S. Geological Survey Techniques and Methods. Retrieved from https://pubs.usgs.gov/tm/06/a45.

Pang, L., Close, M. E., Watt, J. P. C., & Vincent, K. W. (2000). Simulation of picloram, atrazine, and simazine leaching through two New Zealand soils and into groundwater using HYDRUS-2D. *Journal of Contaminant Hydrology*, *44*(1), 19–46. https://doi.org/10.1016/S0169-7722(00)00091-7

Pardé, M. (1933). *Fleuves et Rivières*, vol., (Vol. 1). Paris: Armand Colin.

Payn, R. A., Gooseff, M. N., McGlynn, B. L., Bencala, K. E., & Wondzell, S. M. (2012). Exploring changes in the spatial distribution of stream baseflow generation during a seasonal recession. *Water Resources Research*, *48*(4). https://doi.org/10.1029/2011WR011552

Pedretti, D., & Bianchi, M. (2018). Reproducing tailing in breakthrough curves: Are statistical models equally representative and predictive? *Advances in Water Resources*, *113*, 236–248. https://doi.org/10.1016/j.advwatres.2018.01.023

Pedretti, D., Fernàndez-Garcia, D., Bolster, D., & Sanchez-Vila, X. (2013). On the formation of breakthrough curves tailing during convergent flow tracer tests in three-dimensional heterogeneous aquifers. *Water Resources Research*, *49*, 4157–4173. https://doi.org/10.1002/wrcr.20330

Perdigão, R. A. P., & Blöschl, G. (2014). Spatiotemporal flood sensitivity to annual precipitation: Evidence for landscape-climate coevolution. *Water Resources Research*, *50*, 5492. https://doi.org/10.1002/2014WR015365

Perrin, C., Michel, C., & Andreassian, V. (2001). Does a large number of parameters enhance model performance? Comparative assessment of common catchment model structures on 429 catchments. *Journal of Hydrology*, *242*(3-4), 275–301. https://doi.org/10.1016/S0022- 1694(00)00393-0

Perron, J. T., Kirchner, J. W., & Dietrich, W. E. (2009). Formation of evenly spaced ridges and valleys. *Nature*, *460*(7254), 502–505. https://doi.org/10.1038/nature08174

Petersen, T., Devineni, N., & Sankarasubramanian, A. (2012). Seasonality of monthly runoff over the continental United States: Causality and relations to mean annual and mean monthly distributions of moisture and energy. *Journal of Hydrology*, *468-469*, 139–150. https:// doi.org/10.1016/j.jhydrol.2012.08.028

Philip, J. R. (1957). The theory of infiltration: 1. The infiltration equation and its solution. *Soil Science*, *83*(5), 345–358. https://doi.org/10.1097/00010694-195705000-00002

Philip, J. R. (1969). Theory of infiltration. *Advances in Hydroscience*, *5*, 215–296.

Philip, J. R. (1986). Linearized unsteady multidimensional infiltration. *Water Resources Research*, *22*(12), 1717–1727. https://doi.org/10.1029/WR022i012p01717

Pike, J. G. (1964). The estimation of annual run-off from meteorological data in a tropical climate. *Journal of Hydrology*, *2*(2), 116–123. https://doi.org/10.1016/0022-1694(64)90022-8

Pilgrim, D. H., Chapman, T. G., & Doran, D. G. (1988). Problems of rainfall-runoff modelling in arid and semiarid regions. *Hydrological Sciences Journal, 33*(4), 379–400. https://doi.org/10.1080/02626668809491261

Poff, N. L., Allan, J. D., Bain, M. B., Karr, J. R., Prestegaard, K. L., Richter, B. D., et al. (1997). The Natural Flow Regime. *BioScience*, *47*(11), 769–784. https://doi.org/10.2307/1313099

Ponce, V. M., & Shetty, A. V. (1995). A conceptual model of catchment water balance: 1. Formulation and calibration. *Journal of Hydrology*, *173*(1–4), 27–40. https://doi.org/10.1016/0022-1694(95)02739-C

Porporato, A., Daly, E., & Rodriguez-Ignacio, I. (2004). Soil water balance and ecosystem response to climate change. *The American Naturalist*, *164*(5), 625–632. https://doi.org/10.1086/424970

Potter, N. J., & Zhang, L. (2009). Interannual variability of catchment water balance in Australia. *Journal of Hydrology, 369*(1–2), 120–129. https://doi.org/10.1016/j.jhydrol.2009.02.005

Potter, N. J., Zhang, L., Milly, P. C. D., McMahon, T. A., & Jakeman, A. J. (2005). Effects of rainfall seasonality and soil moisture capacity on mean annual water balance for Australian catchments. *Water Resources Research, 41,* W06007. https://doi.org/10.1029/2004WR003697

Price, K. (2011). Effects of watershed topography, soils, land use, and climate on baseflow hydrology in humid regions: A review. *Progress in Physical Geography: Earth and Environment*, *35*(4), 465–492. https://doi.org/10.1177/0309133311402714

Razavi, S., & Gupta, H. V. (2016). A new framework for comprehensive, robust, and efficient global sensitivity analysis: 2. Application. *Water Resources Research, 52,* 440–455. https://doi.org/10.1002/2015WR017559

Reeves, M., & Miller, E. E. (1975). Estimating infiltration for erratic rainfall. *Water Resources Research*, *11*(1), 102–110. https://doi.org/10.1029/WR011i001p00102

Refsgaard, J. C. , and B. Storm (1995), *MIKE SHE in computer models of watershed hydrology*, edited by V. P. Singh, 804-846 pp., Water Resources Publ., Colorado.

Reggiani, P., Sivapalan, M., & Hassanizadeh, S. M. (2000). Conservation equations governing hillslope responses: Exploring the physical basis of water balance. *Water Resources Research*, *36*(7), 1845–1863. https://doi.org/10.1029/2000WR900066

Rempe, D. M., & Dietrich, W. E. (2014). A bottom-up control on fresh-bedrock topography under landscapes. *Proceedings of the National Academy of Sciences*, *111*(18), 6576–6581.

Richards, L. A. (1931). Capillary conduction of liquids through porous mediums. Physics, 1(5), 318–333. https://doi.org/10.1063/1.1745010 Salvucci, G. D., & Entekhabi, D. (1995). Ponded infiltration into soils bounded by a water table. *Water Resources Research*, *31*(11), 2651–2759.

Richardson, C. M., Zimmer, M. A., Fackrell, J. K., & Paytan, A. (2020). Geologic controls on source water drive baseflow generation and carbon geochemistry: Evidence of nonstationary baseflow sources across multiple subwatersheds. *Water Resources Research*, *56*(7). https://doi.org/10.1029/2019WR026577

Rigon, R., Bertoldi, G., & Over, T. M. (2006). GEOtop: A Distributed Hydrological Model with Coupled Water and Energy Budgets. *Journal of Hydrometeorology*, *7*(3), 371–388. https://doi.org/10.1175/JHM497.1

Rinderer, M., van Meerveld, H. J., & Seibert, J. (2014). Topographic controls on shallow groundwater levels in a steep, prealpine catchment: When are the TWI assumptions valid? *Water Resources Research*, *50*(7), 6067–6080.

https://doi.org/10.1002/2013WR015009

Robinson, E.L.; Blyth, E.M.; Clark, D.B.; Comyn-Platt, E.; Rudd, A.C. (2020). Climate hydrology and ecology research support system potential evapotranspiration dataset for Great Britain (1961-2017) [CHESS-PE]. NERC Environmental Information Data Centre. https://doi.org/10.5285/9116e565-2c0a-455b-9c68-558fdd9179ad

Rodriguez-Iturbe, I., Porporato, A., Ridolfi, L., Isham, V., & Cox, D. R. (1999). Probabilistic modelling of water balance at a point: The role of climate, soil and vegetation. *Proceedings of the Royal Society of London, Series A: Mathematical, Physical and Engineering Sciences, 455,* 3789–3805. https://doi.org/10.1098/rspa.1999.0477

Ronda, R. J. (2002). Spatial Heterogeneity of the Soil Moisture Content and Its Impact on Surface Flux Densities and Near-Surface Meteorology. *Journal of Hydrometeorology*, *3*, 15.

Rossi, M. W., Whipple, K. X., & Vivoni, E. R. (2015). Precipitation and evapotranspiration controls on daily runoff variability in the contiguous United States and Puerto Rico. *Journal of Geophysical Research: Earth Surface, 121,* 128–145. https://doi.org/10.1002/2015JF003446

Ryu, D., & Famiglietti, J. S. (2005). Characterization of footprint-scale surface soil moisture variability using Gaussian and beta distribution functions during the Southern Great Plains 1997 (SGP97) hydrology experiment. *Water Resources Research*, *41*(12), W12433. https://doi.org/10.1029/2004WR003835

Sankarasubramanian, A., & Vogel, R. M. (2002). Annual hydroclimatology of the United States. *Water Resources Research*, *38*(6), 1083. https://doi.org/10.1029/2001WR000619

Santhi, C., Allen, P. M., Muttiah, R. S., Arnold, J. G., & Tuppad, P. (2008). Regional estimation of base flow for the conterminous United States by hydrologic landscape regions. *Journal of Hydrology*, *351*(1–2), 139–153. https://doi.org/10.1016/j.jhydrol.2007.12.018

Schaake, J. C., Koren, V. I., Duan, Q. Y., Mitchell, K., & Chen, F. (1996). Simple water balance model for estimating runoff at different spatial and temporal scales. *Journal of Geophysical Researc*h, *101*(D3), 7461–7475. https://doi.org/10.1029/95JD02892

Schijven, J. F., & Šimůnek, J. (2002). Kinetic modeling of virus transport at the field scale. *Journal of Contaminant Hydrology*, *55*(1–2), 113–135. https://doi.org/10.1016/S0169-7722(01)00188-7

Schreiber, P. (1904). Über die Beziehungen zwischen dem Niederschlag und der Wasserführung der Flüsse in Mitteleuropa. *Z. Meteorol*, *21*(10), 441–452.

SCS (1972). Hydrology. In *National engineering handbook, Supplement A, Section 4, Chapter 10* (pp. 762). Washington, DC: Soil Conservation Service, US Department of Agriculture.

Segura, C., Noone, D., Warren, D., Jones, J. A., Tenny, J., & Ganio, L. M. (2019). Climate, landforms, and geology affect baseflow sources in a mountain catchment. *Water Resources Research*, *55*(7), 5238–5254. https://doi.org/10.1029/2018WR023551

Šejna, M., Šimůnek, J., & van Genuchten, M. Th. (2018). The HYDRUS software package for simulating two-and three-dimensional movement of water, heat, and multiple solutes in variably-saturated media. User manual, version *3.0, PC Progress, Prague, Czech Republic*.

Semenova, O., & Beven, K. (2015). Barriers to progress in distributed hydrological modelling. *Hydrological Processes*, *29*(8), 2074–2078. https://doi.org/10.1002/hyp.10434

Shaman, J., Stieglitz, M., Engel, V., Koster, R., & Stark, C. (2002). Representation of subsurface storm flow and a more responsive water table in a TOPMODEL-based hydrology model. *Water Resources Research*, *38*(8), 31-1-31–16. https://doi.org/10.1029/2001WR000636

Shao, Q., Traylen, A., & Zhang, L. (2012). Nonparametric method for estimating the effects of climatic and catchment characteristics on mean annual evapotranspiration. *Water Resources Research, 48*, W03517. https://doi.org/10.1029/2010WR009610

Shaw, S. B., McHardy, T. M., & Riha, S. J. (2013). Evaluating the influence of watershed moisture storage on variations in base flow recession rates during prolonged rain-free periods in medium-sized catchments in New York and Illinois, USA. *Water Resources Research*, *49*, 6022–6028. https://doi.org/10.1002/wrcr.20507

Sherman, L. K. (1943). Comparison of f-curves derived by the methods of sharp and Holtan and of Sherman and Mayer. Eos, *Transactions American Geophysical Union*, *24*(2), 465–467. https://doi.org/10.1029/TR024i002p00465

Simmons, C. T., Narayan, K. A., & Wooding, R. A. (1999). On a test case for density-dependent groundwater flow and solute transport models: The Salt Lake problem. *Water Resources Research, 35*(12), 3607–3620. https://doi.org/10.1029/1999WR900254

Sivapalan, M. (2018). From engineering hydrology to Earth system science: milestones in the transformation of hydrologic science. *Hydrology and Earth System Sciences*, *22*(3), 1665–1693. https://doi.org/10.5194/hess-22-1665-2018

Sivapalan, M., & Milly, P. C. D. (1989). On the relationship between the time condensation approximation and the flux concentration relation. *Journal of Hydrology*, *105*(3–4), 357–367. https://doi.org/10.1016/0022-1694(89)90113-3

Sivapalan, M., & Wood, E. F. (1986). Spatial heterogeneity and scale in the infiltration response of catchments. In V. K. Gupta, I. Rodríguez-Iturbe, & E. F. Wood (Eds.), Scale problems in hydrology: Runoff generation and basin response (pp. 81–106). Dordrecht: Springer Netherlands. https://doi.org/10.1007/978-94-009-4678-1_5

Sivapalan, M., Beven, K., & Wood, E. F. (1987). On hydrologic similarity: 2. A scaled model of storm runoff production. *Water Resources Research*, *23*(12), 2266–2278. https://doi.org/10.1029/WR023i012p02266

Sivapalan, M., Blöschl, G., Merz, R., & Gutknecht, D. (2005). Linking flood frequency to long-term water balance: Incorporating effects of seasonality. *Water Resources Research, 41,* W06012. https://doi.org/10.1029/2004WR003439

Sivapalan, M., Woods, R. A., & Kalma, J. D. (1997). Variable bucket representation of TOPMODEL and investigation of the effects of rainfall heterogeneity. *Hydrological Processes*, *11*, 1307–1330. https://doi.org/10.1002/(SICI)1099-1085(199707)11:9%3C1307::AID-HYP562%3E3.0.CO;2-Y

Sivapalan, M., Yaeger, M. A., Harman, C. J., Xu, X., & Troch, P. A. (2011). Functional model of water balance variability at the catchment scale: 1. Evidence of hydrologic similarity and space-time symmetry. *Water Resources Research*, *47*(2). https://doi.org/10.1029/2010WR009568

Sivapalan, Murugesu, & Woods, R. A. (1995). Evaluation of the effects of general circulation models' subgrid variability and patchiness of rainfall and soil moisture on land surface water balance fluxes. *Hydrological Processes*, *9*(5–6), 697–717. https://doi.org/10.1002/hyp.3360090515

Skaggs, T. H., Trout, T. J., Šimůne, J., & Shouse, P. J. (2004). Comparison of HYDRUS-2D simulations of drip irrigation with experimental observations. *Journal of Irrigation and*

Drainage Engineering, *130*(4), 304–310. https://doi.org/10.1061/(ASCE)07339437(2004)130:4(304)

Smith, R. E., Smettem, K. R. J., Broadbridge, P., & Woolhiser, D. A. (2002). Infiltration theory for hydrologic applications. *Water Resources Monograph* (Vol. 15, chap. 1, 5, pp. 1-6, 63-96). Washington, DC: American Geophysical Union. https://doi.org/10.1029/WM015

Soylu, M. E., Istanbulluoglu, E., Lenters, J. D., & Wang, T. (2011). Quantifying the impact of groundwater depth on evapotranspiration in a semi-arid grassland region. *Hydrology and Earth System Sciences*, *15*(3), 787–806. https://doi.org/10.5194/hess-15-787-2011

Spence, C., Guan, X. J., Phillips, R., Hedstrom, N., Granger, R., & Reid, B. (2009). Storage dynamics and streamflow in a catchment with a variable contributing area. *Hydrological Processes*, *24*(16), 2209–2221. https://doi.org/10.1002/hyp.7492

Sposito, G. (2017). Understanding the Budyko Equation. *Water*, *9*(4), 236. https://doi.org/10.3390/w9040236

St. Clair, J., Moon, S., Holbrook, W. S., Perron, J. T., Riebe, C. S., Martel, S. J., et al. (2015). Geophysical imaging reveals topographic stress control of bedrock weathering. *Science*, *350*(6260), 534–538. https://doi.org/10.1126/science.aab2210

Staudinger, M., Stahl, K., Seibert, J., Clark, M. P., & Tallaksen, L. M. (2011). Comparison of hydrological model structures based on recession and low flow simulations. *Hydrology and Earth System Sciences*, *15*(11), 3447–3459. https://doi.org/10.5194/hess-15-3447-2011

Sudheer, K. P., Chaubey, I., Garg, V., & Migliaccio, K. W. (2007). Impact of timescale of the calibration objective function on the perfor mance of watershed models. *Hydrological Processes*, *21*(25), 3409–3419. https://doi.org/10.1002/hyp.6555

Sweeney, K. E., Roering, J. J., & Ellis, C. (2015). Experimental evidence for hil slope control of landscape scale. *Science, 349*(6243), 51–53.https://doi.org/10.1126/science.aab0017

Tan, X., Liu, B., & Tan, X. (2020). Global Changes in Baseflow Under the Impacts of Changing Climate and Vegetation. *Water Resources Research*, *56*(9), e2020WR027349. https://doi.org/10.1029/2020WR027349

Tang, Y., & Wang, D. (2017). Evaluating the role of watershed properties in long-term water balance through a Budyko equation based on two-stage partitioning of precipitation. *Water Resources Research*, *53*(5), 4142–4157. https://doi.org/10.1002/2016WR019920

Thomas, H. A. (1981). *Improved methods for national water assessment, report, contract WR 15249270*. Washington, D.C.: U.S. Water Resources Council.

Toth, J. (1963). A theoretical analysis of groundwater flow in small drainage basins. *Journal of Geophysical Research*, *68*(16), 4795–4812. https://doi.org/10.1029/JZ068i016p04795

Troch, P. A., Carrillo, G., Sivapalan, M., Wagner, T., & Sawicz, K. (2013). Climate-vegetation-soil interactions and long-term hydrologic partitioning: Signatures of catchment co-evolution. *Hydrology and Earth System Sciences, 17*(6), 2209–2217. https://doi.org/10.5194/ hess-17-2209-2013

Troch, P. A., De Troch, F. P., & Brutsaert, W. (1993). Effective water table depth to describe initial conditions prior to storm rainfall in humid regions. *Water Resources Research, 29*(2), 427–434. https://doi.org/10.1029/92WR02087

Troch, P. A., Lahmers, T., Meira, A., Mukherjee, R., Pedersen, J. W., Roy, T., & Valdés-Pineda, R. (2015). Catchment coevolution: A useful framework for improving predictions of hydrological change? *Water Resources Research*, *51*(7), 4903–4922. https://doi.org/10.1002/2015WR017032

Troch, P. A., Martinez, G. F., Pauwels, V. R. N., Durcik, M., Sivapalan, M., Harman, C., et al. (2009). Climate and vegetation water use efficiency at catchment scales. *Hydrological Processes*, *23*(16), 2409–2414. https://doi.org/10.1002/hyp.7358

Troch, P., Mancini, M., Paniconi, C., & Wood, E. F. (1993). Evaluation of a distributed catchment scale water balance model. *Water Resources Research*, *29*(6), 1805–1817. https://doi.org/10.1029/93WR00398

Troch, P., van Loon, E., & Hilberts, A. (2002). Analytical solutions to a hillslope-storage kinematic wave equation for subsurface flow. *Advances in Water Resources*, *25*(6), 637–649. https://doi.org/10.1016/S0309-1708(02)00017-9

Turc, L. (1954). Le bilan d’eau des sols: relations entre les précipitations, l’évaporation et l’écoulement. *Annales Agronomiques*, *Se´rie A*(5), 491–595.

van Genuchten, M. T. (1980). A closed-form equation for predicting the hydraulic conductivity of unsaturated soils. *Soil Science Society of America Journal*, *44*(5), 892–898. https://doi.org/10.2136/sssaj1980.03615995004400050002x

van Meerveld, H. J., Seibert, J., & Peters, N. E. (2015). Hillslope-riparian-stream connectivity and flow directions at the Panola Mountain Research Watershed. *Hydrological Processes*, *29*(16), 3556–3574. https://doi.org/10.1002/hyp.10508

Vrugt, J. A., van Wijk, M. T., Hopmans, J. W., & Šimunek, J. (2001). One-, two-, and three dimensional root water uptake functions for transient modeling. *Water Resources Research*, *37*(10), 2457–2470. https://doi.org/10.1029/2000WR000027

Wang, D. (2018). A new probability density function for spatial distribution of soil water storage capacity leads to the SCS curve number method. *Hydrology and Earth System Sciences*, *22*(12), 6567–6578. https://doi.org/10.5194/hess-22-6567-2018

Wang, D., & Cai, X. (2009). Detecting human interferences to low flows through base flow recession analysis. *Water Resources Research*, *45*(7), W07426. https://doi.org/10.1029/2009WR007819

Wang, D., & Hejazi, M. (2011). Quantifying the relative contribution of the climate and direct human impacts on mean annual streamflow in the contiguous United States. *Water Resources Research*, 47, W00J12. https://doi.org/10.1029/2010WR010283

Wang, D., & Tang, Y. (2014). A one-parameter Budyko model for water balance captures emergent behavior in darwinian hydrologic models: Emergent Behavior in Hydrologic Models. *Geophysical Research Letters*, *41*(13), 4569–4577. https://doi.org/10.1002/2014GL060509

Wang, D., & Wu, L. (2013). Similarity of climate control on base flow and perennial stream density in the Budyko framework. *Hydrology and Earth System Sciences*, *17*(1), 315–324. https://doi.org/10.5194/hess-17-315-2013

Wang, G., Xia, J., & Chen, J. (2009). Quantification of effects of climate variations and human activities on runoff by a monthly water balance model: A case study of the Chaobai River basin in northern China. *Water Resources Research*, *45*, W00A11. https://doi.org/10.1029/2007WR006768

Wang, J., Chen, L., & Yu, Z. (2018). Modeling rainfal infiltration on hil slopes using flux-concentration relation and time compression approximation. *Journal of Hydrology*, *557*, 243–253. https://doi.org/10.1016/j.jhydrol.2017.12.031

Wang, Q., Pagano, T. C., Zhou, S., Hapuarachchi, H. A. P., Zhang, L., & Robertson, D. E. (2011). Monthly versus daily water balance models in simulating monthly runoff. *Journal of Hydrology*, *404*(3-4), 166–175. https://doi.org/10.1016/j.jhydrol.2011.04.027

Warrach, K., Stieglitz, M., Mengelkamp, H.-T., & Raschke, E. (2002). Advantages of a Topographically Controlled Runoff Simulation in a Soil–Vegetation–Atmosphere Transfer Model. *Journal of Hydrometeorology*, *3*, 18.

Western, A. W., Grayson, R. B., Blöschl, G., Willgoose, G. R., & McMahon, T. A. (1999). Observed spatial organization of soil moisture and its relation to terrain indices. *Water Resources Research*, *35*(3), 797–810. https://doi.org/10.1029/1998WR900065

Westhoff, M., Zehe, E., Archambeau, P., & Dewals, B. (2016). Does the Budyko curve reflect a maximum power state of hydrological sys- tems? A backward analysis. *Hydrology and Earth System Sciences, 20*(1), 479–486. https://doi.org/10.5194/hess-20-479-2016

Wood, E. F., Lettenmaier, D. P., & Zartarian, V. G. (1992). A land-surface hydrology parameterization with subgrid variability for general-circulation models. *Journal of Geophysical Research, 97*(D3), 2717–2728. https://doi.org/10.1029/91JD01786

Wood, E. F., Lettenmaier, D. P., & Zartarian, V. G. (1992). A land-surface hydrology parameterization with subgrid variability for general circulation models. *Journal of Geophysical Research*, *97*(D3), 2717. https://doi.org/10.1029/91JD01786

Woods, R. A. (2009). Analytical model of seasonal climate impacts on snow hydrology: Continuous snowpacks. *Advances in Water Resources, 32*(10), 1465–1481. https://doi.org/10.1016/j.advwatres.2009.06.011

Xu, X., Yang, D., & Sivapalan, M. (2012). Assessing the impact of climate variability on catchment water balance and vegetation cover. *Hydrology and Earth System Sciences, 16*(1), 43–58. https://doi.org/10.5194/hess-16-43-2012

Yaeger, M., Coopersmith, E., Ye, S., Cheng, L., Viglione, A., & Sivapalan, M. (2012). Exploring the physical controls of regional patterns of flow duration curves—Part 4: A synthesis of empirical analysis, process modeling and catchment classification. *Hydrology and Earth System Sciences, 16*(11), 4483–4498. https://doi.org/10.5194/hess-16-4483-2012

Yang, D., Sun, F., Liu, Z., Cong, Z., & Lei, Z. (2006). Interpreting the complementary relationship in non-humid environments based on the Budyko and Penman hypotheses. *Geophysical Research Letters, 33*, L18402. https://doi.org/10.1029/2006GL027657

Yang, D., Sun, F., Liu, Z., Cong, Z., Ni, G., & Lei, Z. (2007). Analyzing spatial and temporal variability of annual water-energy balance in nonhumid regions of China using the Budyko hypothesis. *Water Resources Research, 43,* W04426. https://doi.org/10.1029/2006WR005224

Yang, H., Yang, D., Lei, Z., & Sun, F. (2008). New analytical derivation of the mean annual water-energy balance equation. *Water Resources Research, 44,* W03410. https://doi.org/10.1029/2007WR006135

Yao, L., Libera, D. A., Kheimi, M., Sankarasubramanian, A., & Wang, D. (2020). The Roles of Climate Forcing and Its Variability on Streamflow at Daily, Monthly, Annual, and Long-Term Scales. *Water Resources Research*, *55*, e2020WR027111. https://doi.org/10.1029/2020WR027111

Yokoo, Y., Sivapalan, M., & Oki, T. (2008). Investigating the roles of climate seasonality and landscape characteristics on mean annual and monthly water balances. *Journal of Hydrology, 357*(3–4), 255–269. https://doi.org/10.1016/j.jhydrol.2008.05.010

Zanardo, S., Harman, C. J., Troch, P. A., Rao, P. S. C., & Sivapalan, M. (2012). Intra-annual rainfall variability control on interannual variability of catchment water balance: A stochastic analysis. *Water Resources Research, 48,* W00J16. https://doi.org/10.1029/2010WR009869

Zhang, K., Kimball, J. S., Nemani, R. R., & Running, S. W. (2010). A continuous satellite-derived global record of land surface evapotranspiration from 1983 to 2006. *Water Resources Research*, *46*(9), W09522. https://doi.org/10.1029/2009WR008800

Zhang, L., Dawes, W. R., & Walker, G. R. (2001). Response of mean annual evapotranspiration to vegetation changes at catchment scale. *Water Resources Research*, *37*(3), 701–708. https://doi.org/10.1029/2000WR900325

Zhang, L., Potter, N., Hickel, K., Zhang, Y. Q., & Shao, Q. X. (2008). Water balance modeling over variable time scales based on the Budyko framework—Model development and testing. *Journal of Hydrology*, *360*(1–4), 117–131. https://doi.org/10.1016/j.jhydrol.2008.07.021

Zhang, X., Jiao, J. J., Li, H., Luo, X., & Kuang, X. (2020). Effects of Downward Intrusion of Saline Water on Nested Groundwater Flow Systems. *Water Resources Research*, *56*(10), e2020WR028377. https://doi.org/10.1029/2020WR028377

Zhao, R. (1992). The Xinanjiang model applied in China. *Journal of Hydrology*, *135*(1–4), 371–381. https://doi.org/10.1016/0022-1694(92)90096-E

Zimmer, M. A., & McGlynn, B. L. (2017). Ephemeral and intermittent runoff generation processes in a low relief, highly weathered catchment. *Water Resources Research*, *53*(8), 7055–7077. https://doi.org/10.1002/2016WR019742